POLITECNICO

MILANO 1863

SCUOLA DI INGEGNERIA INDUSTRIALE
E DELL'INFORMAZIONE

Study of Suprathermal Electron Dynamics by Modelling the Electron Cyclotron Emission

Tesi di Laurea Magistrale in
Nuclear Engineering - Ingegneria Nucleare

Author: **Lorenzo Votta**

Student ID: 967891
Advisor: Prof. David Dellasega
Co-advisors: Joan Decker, Mathias Hoppe
Academic Year: 2021-22

Ai miei genitori

Abstract

Electrons gyrating around magnetic field lines emit radiation at the frequency $\Omega_c = n\,eB/(\gamma m)$, where e is the elementary charge, B is the magnetic field amplitude, m is the electron rest mass, γ is the ralitivistic factor and n is the harmonic number. This radiation mechanism is called electron cyclotron emission (ECE). In the presence of a magnetic field amplitude gradient, as in a tokamak, the origin of emission is related to the frequency of the emission and a temperature profile can be reconstructed by scanning a range of frequencies, which is the general purpose of ECE diagnostics. The definition of *temperature* assumes that the plasma is in thermal equilibrium with a Maxwellian velocity distribution for its particles. In certain scenarios, the plasma may contain a significant proportion of suprathermal particles whose energy exceeds that of the thermal particles by several orders of magnitude, affecting both temperature measurements and profile reconstruction. Measuring ECE at various frequencies along vertical lines of sight (VECE) with constant magnetic field amplitude B provides a scan in electron energy via the relativistic factor γ. On the other hand, reconstructing the 3D bounce-averaged guiding center electron distribution function from ECE measurements is an ill-conditioned problem and a more promising approach consists of constructing an equivalent synthetic ECE diagnostic providing simulations that can be directly compared to measurements. A new general synthetic ECE diagnostic that includes the effect of suprathermal electrons is constructed: the YODA code. This code is able to calculate: **i)** the EC emission and (re)absorption based on any arbitrary numerical electron distribution function calculated by any first-principle kinetic codes (as the 3-D bounce-averaged relativistic Fokker-Planck code LUKE) for arbitrary line of sight simulated using the C3PO ray-tracing code (which also model the detection system); **ii)** the transport of EC radiated intensity along the propagation path. In this work, the YODA code is validated for thermal plasmas, and two direct application to TCV tokamak electron cyclotron current drive (ECCD) experiments are envisioned with good agreement between the experimental vertical ECE measurements and synthetic intensity trends, opening new paths regarding suprathermal electron studies in tokamak plasmas.

Keywords: nuclear fusion, plasma physics, suprathermal electrons, runaway electrons,

electron cyclotron emission, electron cyclotron resonance heating, electron cyclotron current drive, microwave, synthetic diagnostic, Fokker-Planck.

Abstract in lingua italiana

Gli elettroni che orbitano intorno a linee del campo magnetico emettono radiazione alla frequenza di ciclotrone $\Omega_c = neB/(\gamma m)$, dove e rappresenta la carica elementare, B l'ampiezza del campo magnetico, m la massa a riposo dell'elettrone, γ il fattore relativistico e n il numero armonico. Questa radiazione è chiamata emissione ciclotronica degli elettroni (ECE). In presenza di un gradiente nell'ampiezza del campo magnetico, come nei tokamak, l'origine dell'emissione è legata alla frequenza dell'emissione e il profilo di temperatura elettronica può essere ricostruito scandendo un range di frequenze, che è lo scopo generale delle diagnostica ECE. Tuttavia, la definizione di *temperatura* assume che il plasma sia in equilibrio termico con una distribuzione di velocità maxwelliana per le sue particelle. In determinati scenari, il plasma può contenere una porzione significativa di particelle sovratermiche la cui energia supera quella delle particelle termiche di diversi ordini di grandezza. La presenza di una popolazione significativa di elettroni sovratermici influisce sia sulle misurazioni della temperatura che sulla ricostruzione del profilo degli elettroni. La diagnostica ECE può comunque fornire informazioni preziose sulla distribuzione degli elettroni sovratermici nello spazio delle fasi. La misura della ECE a varie frequenze lungo una linea di vista verticale (VECE) con ampiezza del campo magnetico costante B fornisce una scansione dell'energia degli elettroni tramite il fattore relativistico γ. La ricostruzione della funzione di distribuzione degli elettroni a partire dalle misurazioni della ECE è un problema mal condizionato e un approccio più promettente consiste nella costruzione di una diagnostica sintetica equivalente che fornisce simulazioni che possono essere direttamente confrontate con le misurazioni dell'ECE. In questo lavoro viene costruita una nuova diagnostica sintetica per l'ECE che include l'effetto degli elettroni sovratermici: il codice YODA. Questo codice è in grado di calcolare: **i)** l'emissione ed il (ri)assorbimento di EC sulla base della funzione di distribuzione degli elettroni calcolata utilizzando il codice 3-D bounce-averaged guiding center relativistic Fokker-Planck LUKE, per una linea di vista arbitraria simulata utilizzando il codice di ray-tracing C3PO, che modella anche il sistema di rilevamento; **ii)** il trasporto dell'intensità della radiazione di EC lungo il percorso di propagazione. In questo lavoro, il codice YODA viene sia validato per plasmi termici e che utilizzato per applicazioni dirette in due esperimenti di guida

di corrente di elettrone ciclotrone (ECCD), ottenendo buoni risultati dai confronti diretti tra i trend delle misure sperimentali della ECE verticale e le intensità sintetiche, aprendo così nuove strade allo studio degli elettroni sovratermici nei tokamak.

Contents

1 | Introduction

The energy crisis of 2022 will serve as a stark reminder of how the absence of diversification in the world's energy production systems can represent an enormous problem for the survival of all humanity. In addition, countries have continued to use coal, oil, and natural gas extensively to power their economy in spite of decades-long recommendations to reduce dependence on fossil fuels whose combustion is the main cause of the increase in the concentration of climate-altering agents in the Earth's atmosphere, as proven in several IPCC (Intergovernmental Panel on Climate Change) reports [57].
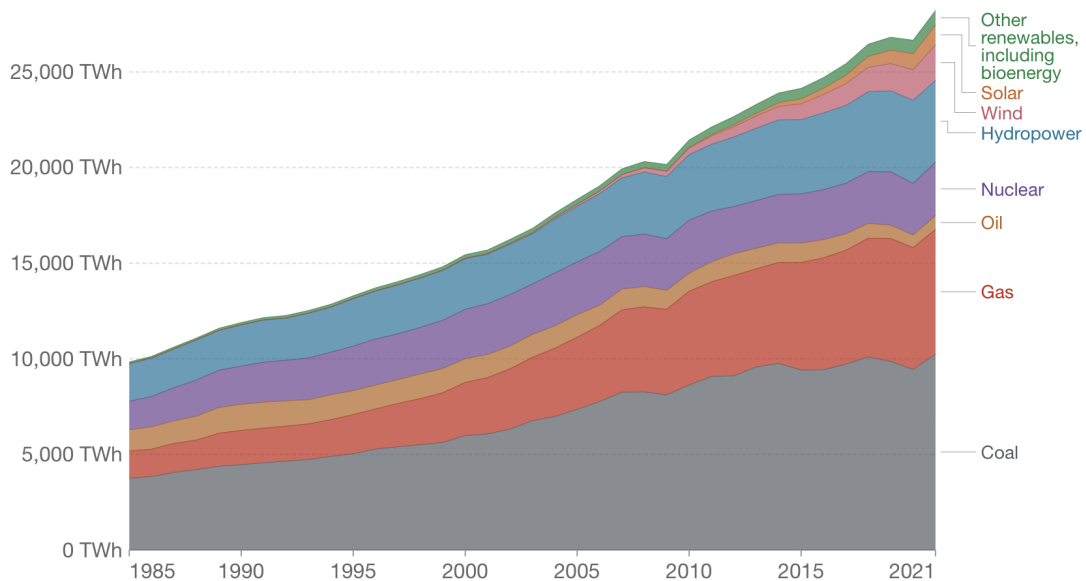
Figure 1.1: World electricity production by source - 2022 [46]

Thus, it becomes clear that finding a solution to meet the world's increasing energy needs in a way that is sustainable for both the environment and human communities is one of the main problems humanity will face in the next decades. Therefore, renewable energy sources, like hydroelectric, wind or solar technology, are considered by many as the main solution to produce non-polluting clean energy. Although they can provide a significant amount of clean energy (in terms of CO_2 production), there are still substantial issues

in terms of energy storage and availability due to uncontrollable seasonal/daily climate intermittences. In addition, the current difficulties in sourcing materials such as silicon and rare minerals, which are needed for the production of wind and solar power plants, are a challenge not to be underestimated. Finally, nuclear fission power plants have the potential to provide ultralow-emission power generation, but for reasons mainly related to public opinion about their safety, radioactive waste management and nuclear weapons proliferation, they still constitute a minority share in energy production.

The scientific community is looking for new methods of producing energy. Nuclear fusion is predicted to be a significant possibility to enhance the energy grid supply in the second part of the 21th century, while being a very difficult undertaking. To date, no nuclear fusion power plants exist, but the scientific and technological effort around their future realization constitutes an unmissable opportunity and one of the greatest challenges for all of humanity. In the next section, both the nuclear fusion process and some of the challenges to achieve this process are explored.

1.1. Thermonuclear Fusion

Nuclear fusion is a nuclear reaction between two light nuclei (e.g. the Hydrogen isotopes Deuterium D and Tritium T) with a given Q *value*[1] which depends on the involved nuclides. To talk about fusion, it is important to introduce the physical concept of *binding energy*. It is defined, for the nucleus ground state, as [13]

$$B.E. = Zm_pc^2 + (A - Z)m_nc^2 - U \tag{1.1}$$

where Z is the atomic number, A is the mass number, m_p is the proton mass, m_n is the neutron mass, c is the speed of light in vacuum, while the total energy of the nucleus is $U = m_{\text{nucl}}c^2$. Figure 1.2 shows a plot of the binding energy per nucleon as a function of the atomic mass.

---

[1]The Q value is the amount of energy absorbed or released during a nuclear reaction.
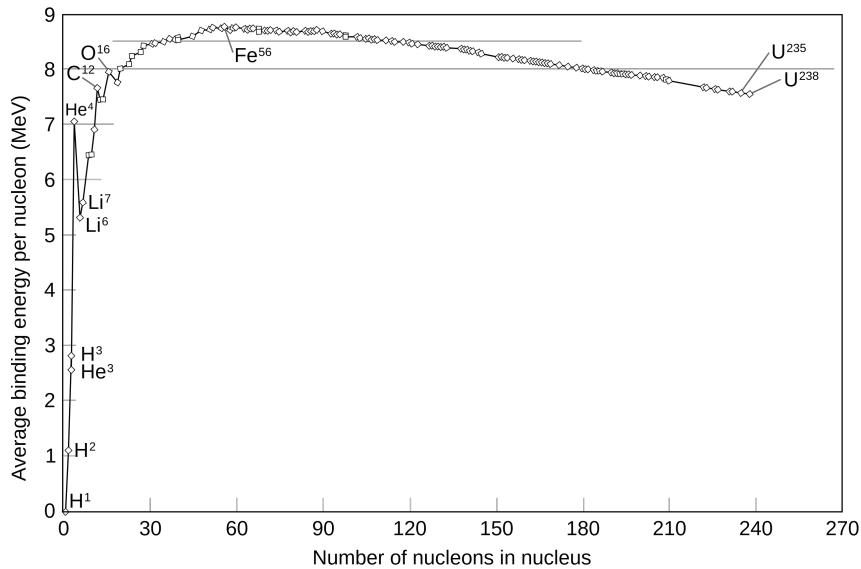
Figure 1.2: Binding energy per nucleon vs mass number for the main nucleons. The maximum of the binding energy per nucleon is achieved at Iron and then decreases for light elements [Public Domain https://it.m.wikipedia.org/].

Energy may be collected from nuclear reactions, such as nuclear fusion and nuclear fission, by taking advantage of the rise in binding energy per nucleon that results from these reactions. Particularly in nuclear fusion, two light nuclei merge to form a heavier and more stable product, and the the reaction releases net energy. In contrast to the electromagnetic force that underlies chemical processes, the fundamental interaction involved in nuclear fusion, the *strong nuclear force*, is ideed very strong, but has a short range of action. This is the primary cause of the high energy density of nuclear fusion.

Very light nuclei are best suited for energy production via nuclear fusion, for two separate reasons. First, the gain in binding energy per nucleon is often substantially larger for the fusion of two extremely light nuclei. Secondly, using the lightest nuclei reduces the amount of energy needed to start the reaction since the two nuclei must overcome the Coulomb potential barrier that arises as a result of their positive charges in order to fuse together. Therefore, hydrogen and helium isotopes are the most commonly studied reactants in fusion applications. Three fusion reactions may be useful for the generation of nuclear energy, according to studies on the nuclear characteristics of light element fusion. Deuterium, Tritium, and ^{3}He, are involved in these. Among them, the most studied in the nuclear energy field is the fusion reaction between D and T:

$$D + T \rightarrow {}_2^4\text{He}\,(3.56\,MeV) + {}^1\text{n}\,(14.03\,MeV) \tag{1.2}$$
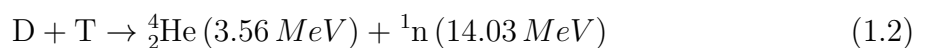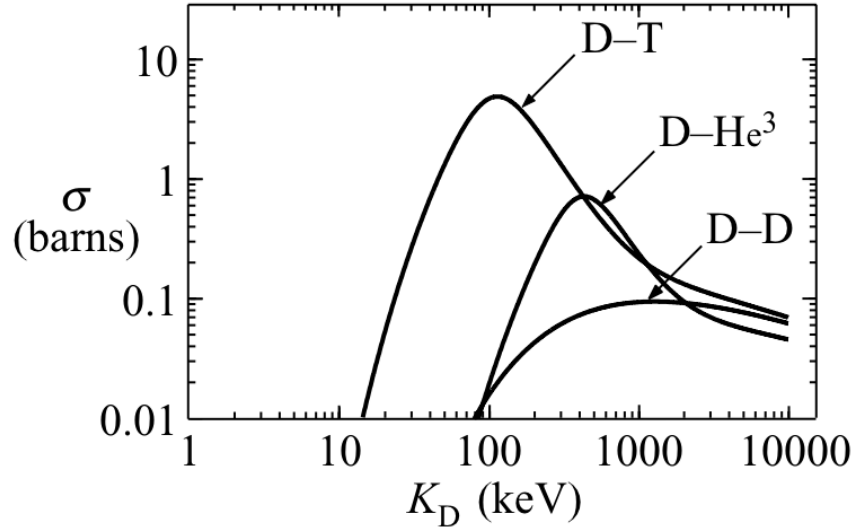
Figure 1.3: Experimentally measured cross sections for the D–T, D–^3He, and D–D fusion reactions as a function of deuteron energy $K_D = m_D v_D^2/2$ [58].

In fact, looking at the reaction cross section for these three reactions plotted vs. deuteron energy (figure 1.3), it can be noticed how relatively high cross-section values can be obtained only for energies between 10 keV and 100 keV[2] and how the D-T reaction is particularly advantageous compared to the others. These high temperatures required to achieve sufficiently high fusion reaction rates, entails that the reactants of a fusion reaction must be in the plasma state.

1.1.1. The plasma state

Chen defines a plasma as [25]

> *A plasma is a quasi-neutral gas of charged and neutral particles which exhibits collective behaviour.*

In general, it is composed of at least two sufficiently large populations of oppositely charged particles, which are often ions and electrons produced during ionization processes. It is also possible to distinguish between partially and completely ionized plasmas depending on the presence of a neutral population among the plasma components.

The charged populations are in a concentration such that the physical properties of the system are significantly affected by *space charge effects* and electromagnetic phenomena. In fact, in contrast to short-range nearest-neighbor Coulomb interactions in common

---

[2]Roughly corresponding to more than a hundred million Celsius degrees, in fact $E[eV] = K_B T[K]$, e.g $1\,eV = 11605\,K$

materials (including solids, liquids, and gases), this system is affected also by long-range collective effects due to the charged species, which are affected by external electric and magnetic fields. At the same time, small-scale charge separation has a significant impact on the electromagnetic field, in fact if an unbalanced charge were to arise, electrons would immediately redistribute to balance it out. The *Debye length* is the typical characteristic length where charge imbalance may occur without being shielded by nearby particles:

$$\lambda_D = \sqrt{\frac{\varepsilon_0 T}{ne^2}} \tag{1.3}$$

where n is the plasma density, T is the plasma temperature[3], ε_0 is the vacuum dielectric constant and e is the elementary charge.

If one releases a certain charge density, after having displaced it, the charges will feel an electromagnetic force related to the charge separation and start to oscillate with a characteristic frequency called *plasma frequency*:

$$\omega_p = \sqrt{\frac{Zne^2}{\epsilon_0 m}} \tag{1.4}$$

where Z and m are respectively the atomic number and the mass of the considered species[4]. Because of this, it is possible to give a more quantitative definition of plasma by requiring that $\lambda_D \ll L$, $n\lambda_D \gg 1$ and $\omega_p \ggg \nu_{en}$. It means that the collective effects (e.g. charge shielding) dominate over binary interactions[5].

Finally as is shown in the table (1.1), there is a very wide range of densities and temperatures that different plasmas may exist in.

---

[3]A plasma in general is composed of different species. In this Debye length definition, electrons and ions are assumed to be in thermal equilibrium, which is not always true.

[4]For a plasma the total plasma frequency is $\omega_{p,total}^2 = \omega_{p,e}^2 + \sum \omega_{p,i}^2$ and since the ions inertia is bigger than the electrons', it is common to refer with plasma frequency to the electron plasma frequency $\omega_{p,e} = \sqrt{n_e e^2/(\epsilon_0 m_e)}$.

[5]L is the macroscopic length scale of the system and ν_{en} is the frequency of collision between electrons and neutrals.

Type of plasma	Temperature T [K]	Density n [m^{-3}]
Intergalactic gas	10^8	1
Interstellar medium	10^4	10^6
Gas cloud in galaxies	$10^4...10^6$	10^{12}
Fusion plasmas	10^8	$10^{20}...10^{32}$
Technical plasmas	$10^3...10^5$	$10^{15}...10^{25}$
Electron cloud in metals	10^5	8×10^{28}
Surface of stars	10^4	10^{22}
Star center	$10^7...10^8$	10^{30}
White dwarf	10^4	10^{36}
Neutron star	10^4	10^{45}

Table 1.1: Parameter range of plasmas in the universe and on Earth

Thus, it becomes evident that comparing the qualitative behavior of various plasmas is not straightforward.

1.2. Magnetic Confinement Nuclear Fusion

The most promising fusion reactor concepts for energy production are based on magnetic confinement fusion (MCF), where external magnetic fields are exploited to confine the plasma: in this section, some basic physical principles concerning this approach are outlined. Subsection 1.2.1 describes the motion of charged particles in an external field, while subsection 1.2.2 shows the features of one device specifically designed to achieve magnetically confined fusion: the *Tokamak*.

1.2.1. Charged Particle Dynamics in External Field

A particle of mass m and charge q under the action of an external electric $\boldsymbol{E}$ and magnetic $\mathbf{B}$ field will experience a force called the *Lorentz force*

$$\boldsymbol{F}_L = \boldsymbol{E} + \boldsymbol{v} \times \boldsymbol{B}. \tag{1.5}$$

Therefore, Newton's equation of motion can be written as

$$m\frac{d^2\boldsymbol{x}}{dt^2} = q\left[\boldsymbol{E}(\boldsymbol{x}(t), t) + \dot{\boldsymbol{x}} \times \boldsymbol{B}(\boldsymbol{x}(t), t)\right], \tag{1.6}$$

which is, in general, not trivial to solve because the second temporal derivative of the position x of the particle, at the time instant t, will be dependent on the electric and magnetic fields that, in turn, will depend on the position considered: the problem is intrinsically non-linear. To solve it, one can study the system under certain degrees of ideality, gradually relaxing the assumptions made, making the description closer to reality.

From the theory [19], a charged particle subjected only to an external uniform and constant magnetic field B, follows a helical trajectory as depicted in figure 1.4. In the plane
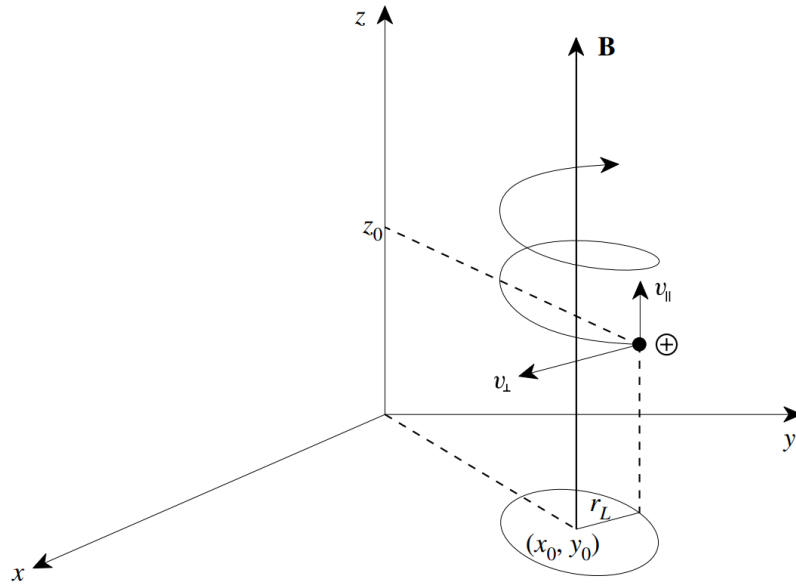
Figure 1.4: Orbit of a positive charged particle in a constant and uniform magneitc field oriented as the z axis in a cartesian coordinate system [19].

of motion $z = v_\parallel t + z_0$, the orbit exhibits uniform circular motion. In the non-relativistic limit, the gyration frequency is known as *cyclotron frequency*

$$\Omega_c = \frac{qB}{m},\tag{1.7}$$

while the gyro-radius is called *Larmor radius*

$$\rho_L = \frac{v_\perp m}{eB}.\tag{1.8}$$

The orbit's center, called the *guiding center*, describes a uniform rectilinear motion along the magnetic field line itself.

If one adds to the system a generic constant external force F, the basic helical motion described above is altered, resulting in a cycloidal trajectory [19]. The particle will gyrate

in the plane orthogonal to the parallel component of the velocity $v_\parallel$ around the guiding center, whose motion is now obtained as the combination of a uniform acceleration in the direction parallel to the magnetic field line and a uniform rectilinear motion with a *drift velocity*

$$\boldsymbol{v}_D = \frac{1}{q}\frac{\boldsymbol{F} \times \boldsymbol{B}}{B^2}, \tag{1.9}$$

in the direction orthogonal to both the magnetic field and the external force. In cases of practical importance in MCF, if the external force is due to the action of an external electric field, so that $\boldsymbol{F} = q\boldsymbol{E}$, the phenomenon is referred to as $\boldsymbol{E} \times \boldsymbol{B}$ *drift*. Also in this case it involves a drift velocity that is either perpendicular to both the electric and magnetic fields, in the same direction for both positively and negatively charged particles [19].

Another drift can arise if one considers a varying magnetic field. If the magnetic field only varies in the xy plane, an expansion to first order of the magnetic field in a Taylor series centered around the guiding-center, it is possible to find an expression for the so called ∇B *drift* velocity

$$\boldsymbol{v}_{\nabla B} = \mathrm{sgn}q\frac{v_\perp \rho_L}{2}\frac{\boldsymbol{B} \times \nabla B}{B^2}. \tag{1.10}$$

In addition, if the magnetic field line is not straight, there is another type of drift motion caused by the eventual curved geometry of the field. This motion is generated by the centripetal force acting on the particle $\boldsymbol{F}_c = mv_\parallel^2 \boldsymbol{R}_c/R_c^2$, where $\boldsymbol{R}_c$ is the vector which identifies the local curvature radius of the field. Inserting the centripetal force into equation 1.9, it is possible to find an expression for the *curvature drift* velocity

$$\boldsymbol{v}_c = \frac{mv_\parallel^2}{qB^2}\frac{\boldsymbol{R}_c \times \boldsymbol{B}}{R_c^2}. \tag{1.11}$$

An important result is the existence of an adiabatic invariant, which serves as an approximate constant of motion. However, it is approximate because its derivation involves averaging over a gyro period, while assuming that the magnetic field is slowly varying. The adiabatic invariant takes the form of the *magnetic moment* and it can be expressed as

$$\mu = \frac{mv_\perp^2}{2B} = \mathrm{const.} \tag{1.12}$$

In many in magnetic confinement devices, this quantity plays a very important role, since it governs how the perpendicular energy of a charged particle evolves in time in the presence of a weakly varying magnetic field.

1.2.2. The Tokamak Principle

After having provided a general description of the motion of a single charged particle in external magnetic and electric fields, now it is possible to focus on one of the most promising machines designed to achieve nuclear fusion: the *Tokamak*. The term "tokamak" originates from Russia and is derived from the Russian acronym "Toroidalnaya kamera magnitnaya katuschka", which means toroidal chamber with magnetic coils. The tokamak is a machine primarily composed of a vacuum vessel with a toroidal shape, which is symmetric toroidally and surrounded by an array of magnetic coils. The purpose of these coils is to ensure the confinement of the charged particles that make up the plasma. The tokamak reactor concept is currently the main direction of research in controlled nuclear fusion. The magnetic confinement structure in a tokamak is schematically represented in figure 1.5.
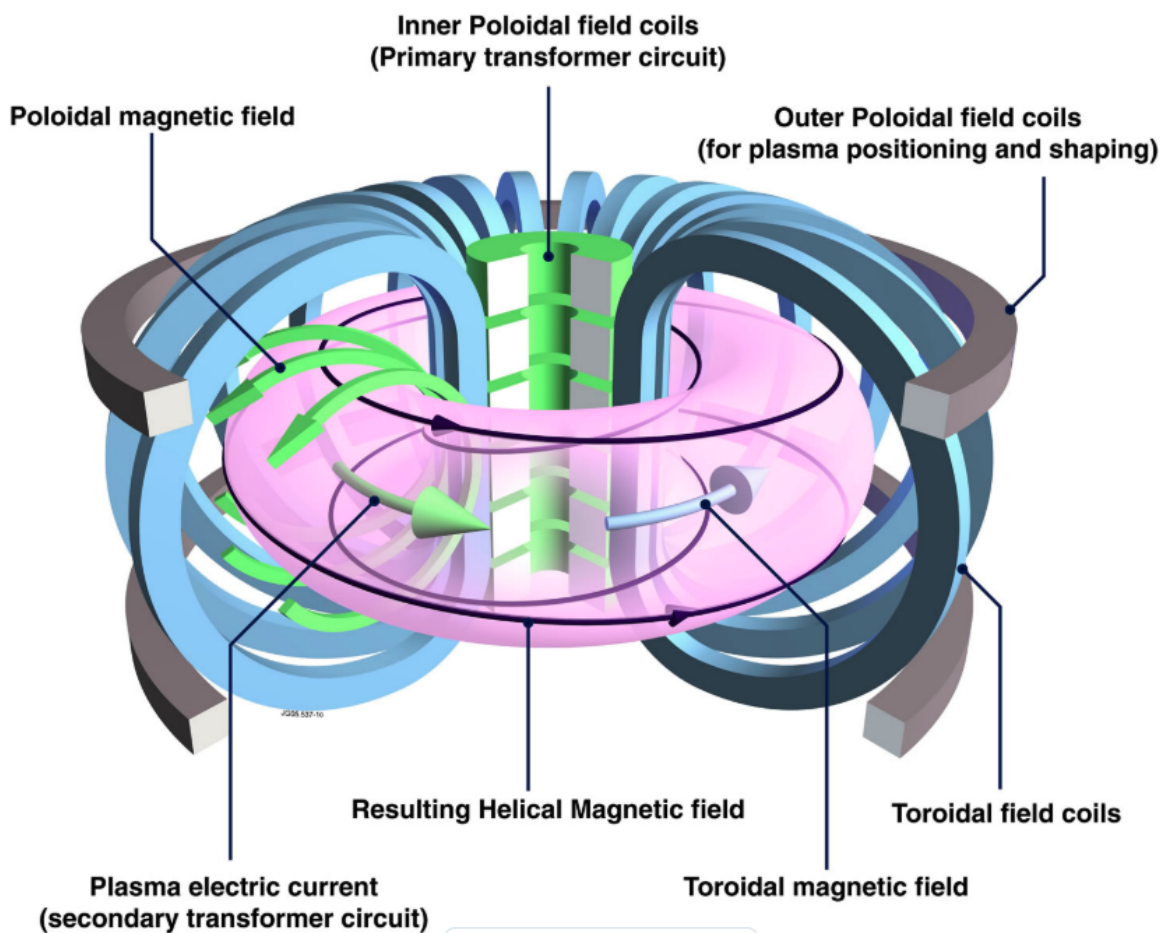

Figure 1.5: Schematic representation of the tokamak geometry

The tokamak's magnetic configuration can be described by means of the fundamental properties of a static magnetic field

$$\nabla \cdot \boldsymbol{B} = 0 \tag{1.13a}$$

$$\nabla \times \boldsymbol{B} = \mu_0 \boldsymbol{J} \tag{1.13b}$$

An important property of equation (1.13a) is that the magnetic field lines do not have starting or ending points. This condition is be met by either closed or open lines, which may occupy a finite region of space or extend to infinity: in this latter case, one talks about a *magnetic surface*. The magnetic field configuration of the tokamak, which falls under the latter category, is the result of combining toroidal and poloidal field components:

$$\boldsymbol{B} = B_\theta \boldsymbol{e}_\theta + B_\phi \boldsymbol{e}_\phi. \tag{1.14}$$

In this case, as depicted in figure 1.6, each resulting magnetic field line is an infinitely long open line that *ergodically* cover the associated toroidal magnetic surface, giving rise to a set of nested magnetic surfaces. From equation (1.13b) it is possible to show that the magnetic field configuration exhibits a $1/R$ radial dependence (where R is the major radius). Therefore, in the presence of a purely toroidal magnetic field, the motion of charged particles would not be confined in space since the onset of a ∇B drift and a curvature drift would promote the motion of the particles either upward or downward, thus separating oppositely charged particles and giving rise to a vertical electric field, responsible for an $\boldsymbol{E} \times \boldsymbol{B}$ drift in the radial direction. In this perspective, the addition of a poloidal component to the magnetic field, which provides the particles with the possibility of exploring different radial positions during the zero-order gyro-motion along the resulting helical magnetic field lines, is crucial in compensating the arising drifts, thus making the overall motion confined in space: this is the basic principle on which the tokamak is designed.

In a tokamak, the dominant toroidal component of the magnetic field B_ϕ is generated via poloidal coils that are distributed throughout the length of the chamber, whereas the poloidal field component B_θ is produced by a toroidal current flowing in the plasma. This *plasma current*, which is induced by a central transformer utilizing electromagnetic induction, provides *Ohmic heating* thereby helping to increase the plasma temperature. Additionally, toroidal coils are utilized to control the equilibrium of the plasma. In a tokamak, the ohmic heating mechanism is not always sufficient to maintain the plasma at the desired temperature level required for sustained fusion reactions. As a result,
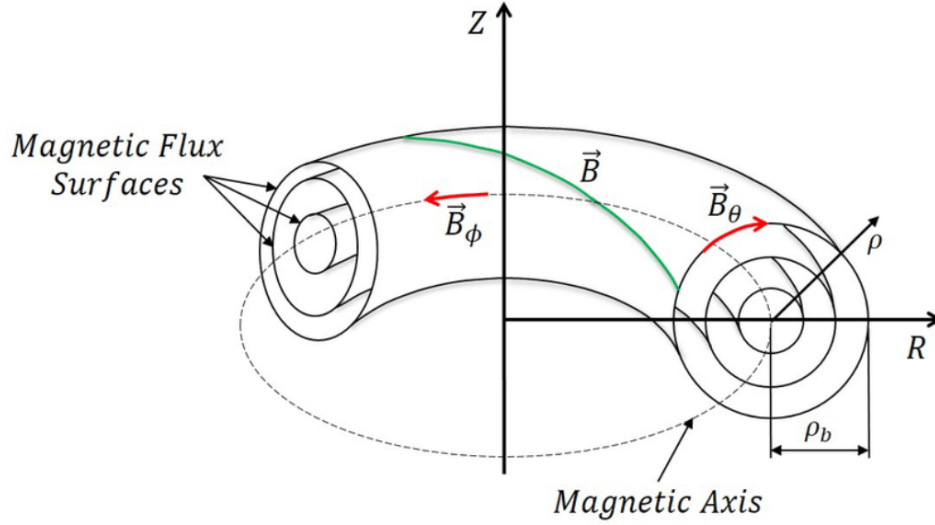
Figure 1.6: Illustration of nested magnetic sufaces in a toroidal + poloidal magnetic field.

alternative *current drive* mechanisms are needed to supplement or replace the ohmic heating.

One reason for this is that the ohmic heating mechanism is limited by the resistivity of the plasma, which decreases with temperature as $\propto T^{-3/2}$. The problem is related to that turbulent transport becomes too strong for really high temperatures to be reached. A solution to overcome this limitation is the Radio frequency (RF) wave resonance heating, a mechanism which allows the energy transfer from waves to particles without depending on collisions. In the plasma scenarios studied in this thesis, the suprathermal electrons are generated by the heating of electrons through Electron Cyclotron Resonance Heating (ECRH) and Current Drive (ECCD). This current drive technique can also be very useful for mitigating various current-driven instabilities, like tearing modes.

1.3.   Production of Fast Electrons

1.3.1.   Electron Cyclotron Current Drive

The application of electron cyclotron wave injection is a method used to drive current in tokamak plasmas. This technique's ability to deposit energy in the plasma in a highly localized manner makes it well-suited for shaping current profiles and managing or suppressing magnetohydrodynamic (MHD) instabilities, such as sawtooth crashes and neoclassical tearing modes (NTM) [45].

To selectively accelerate electrons with a particular sign of parallel[6] velocity $v_\parallel$, it is necessary to inject electron cyclotron waves into the plasma with a finite tangential component of the wave vector ($k_\parallel \neq 0$). One theory developed to describe the ECCD process hinges on the *Fisch-Boozer* effect [41], which generates an asymmetric resistivity in the distribution function without imparting parallel momentum directly. This phenomenon is achieved by boosting the perpendicular velocity of electrons moving in a specific direction relative to the toroidal magnetic field, as depicted in figure 1.7. The decrease in
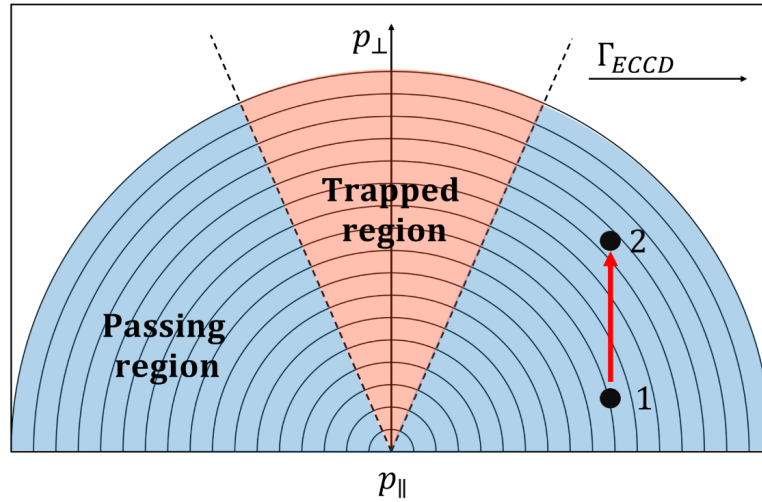
Figure 1.7: Illustration of the Fisch-Boozer current drive mechanism.

the cross section of Coulomb collisions with increasing relative speed between particles is the main reason for the preservation of the Maxwellian distribution function in the bulk of the distribution, where thermal particles with velocities close to the thermal velocity reside. Suprathermal particles, on the other hand, have higher relative speeds compared to other particles in their frame of reference, leading to reduced collisional coupling and strong deviation from the Maxwellian equilibrium in the tail of the distribution function. In typical experimental conditions, a steady-state situation is reached between heating, collisions, and losses (such as radiation and radial transport). The induced current is proportional to the anisotropy of the steady-state electron distribution function with respect to the magnetic field direction, and the ion contribution is negligible due to the large mass ratio between ions and electrons. A quantitative analysis showed that it may be advantageous to invest more energy to accelerate fast electrons, in order to maintain a steady-state tail anisotropy of the distribution function. Although more energy is required for their acceleration, the reduced collisional coupling allows the induced perturbation to resist collisional isotropization for longer times, making the investment profitable.

---

[6]The terminology *parallel* and *perpendicular* refer to the direction of motion relative to the magnetic field lines.

Being more quantitative, the absorption of EC waves causes a movement of electrons from one velocity position to another, resulting in a displacement of a certain number of electrons from position 1 ($v = v_1$) to position 2 ($v_2 \simeq \sqrt{v_1^2 + \Delta E/2m_e}$). A formula proposed by Alikaev and Parail [3] can be used to express the EC-induced current:

$$j = \frac{e\boldsymbol{v}_1 P_d^{EC}}{\Delta E \nu_e(\boldsymbol{v}_2)} \left(1 - \frac{\nu_e(\boldsymbol{v}_2)}{\nu_e(\boldsymbol{v}_1)}\right) \tag{1.15}$$

where P_d^{EC} indicates the EC power density. It can be clearly seen from this expression that a positive net current drive $j > 0$ can be achieved thanks to the difference in collisionality $\nu_e(\boldsymbol{v}_2) < \nu_e(\boldsymbol{v}_1)$. Following the work of Fisch and Boozer, the ECCD efficiency can be expressed as a function of the electron temperature T_e, the electron density n_e and the plasma effective charge Z_{eff} as

$$\eta_{ECCD} \equiv \frac{j_{EC}}{P_d^{EC}} \simeq \frac{\varepsilon_0^2}{ln\Lambda \cdot R \cdot n_e e^3} \frac{T_e}{Z_{eff} + 5}, \tag{1.16}$$

where $ln\Lambda$ is the Coulomb logarithm, R is the plasma major radius and ε_0 is the vacuum permittivity.

There are several factors which can influence the ECCD efficiency. Among them it is worth to cite the effect of trapped particles and of the toroidal injection angle.

Trapped particles

For a particle in a tokamak the magnetic moment is an adiabatic invariant. Assuming that the particle's kinetic energy E_k is conserved, in the non-relativistic limit, the following equation holds

$$E_k = \frac{mv_\parallel^2}{2} + \mu B = \text{const.} \tag{1.17}$$

As a particle moves along its orbit from the outer region to the inner region of a tokamak, the magnetic field strength rises. Since μ remains constant, to satisfy the energy conservation principle, a reduction in the parallel velocity $v_\parallel$ of the particle is expected. One can imagine to have a particle in a tokamak with initial parallel and perpendicular velocities $v_\parallel = v_{\parallel,0}$ and $v_\perp = v_{\perp,0}$ respectively, in a point where the magnitude of the magnetic field is $B = B_0$. The energy conservation implies that the parallel velocity $v_\parallel$ vanishes if

$$\frac{v_{\perp,0}^2}{v_{\parallel,0}^2 + v_{\perp,0}^2} \geq \frac{B_0}{B_{\max}}, \tag{1.18}$$

where B_{max} represents the highest magnetic field strength encountered by the particle as
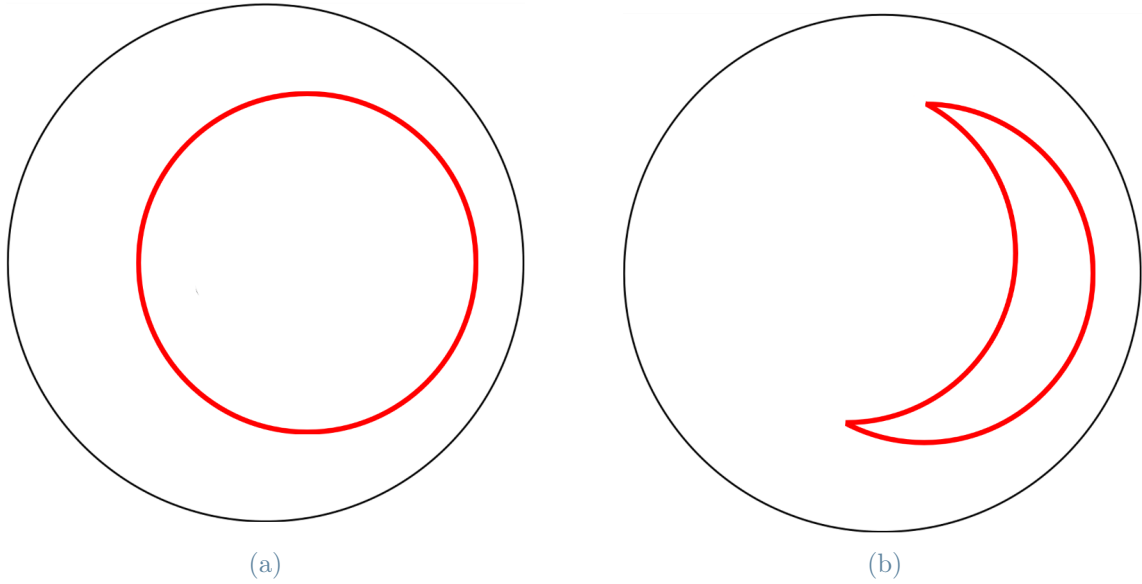
Figure 1.8: Illustration of the guiding center trajectories projected on the tokamak poloidal plane: (a) passing trajectory - (b) trapped trajectory.

it moves along its orbit. If this condition is fulfilled, the parallel velocity $v_\parallel$ changes sign, the particle will reverse direction and bounce back, resulting in an orbit that resembles a banana shape when projected onto a poloidal cross-section. These orbits are called *trapped* orbits, or informally, banana orbits in tokamaks, because the particle is effectively confined between two poloidal angles in the magnetic field, causing it to bounce back and forth. On the other hand, particles with smaller initial ratios of $v_{\perp,0}/v_{\parallel,0}$ will be able to complete an orbit without reversing direction and instead follow *passing* or *circulating* orbits. It is worth mentioning that trapped particles do not contribute to the plasma current. Consequently, cyclotron absorption occurring within the trapped region leads to a degradation of the current drive efficiency. Despite power deposition taking place outside the trapped electron region, it is plausible for the EC wave absorption to push some of the resonant electrons from the passing region into the trapped region. This not only diminishes the current drive efficiency but may also result in a current component running counter to the desired direction. Due to the bounce motion, the distribution function becomes quickly symmetrized inside the trapped region, thereby prompting symmetric detrapping on both sides of the trapped region boundaries (positive and negative $v_\parallel$). Therefore, asymmetric trapping, followed by symmetric detrapping, may create a net current running in the injected wave direction, which is referred to as the Ohkawa effect [72].
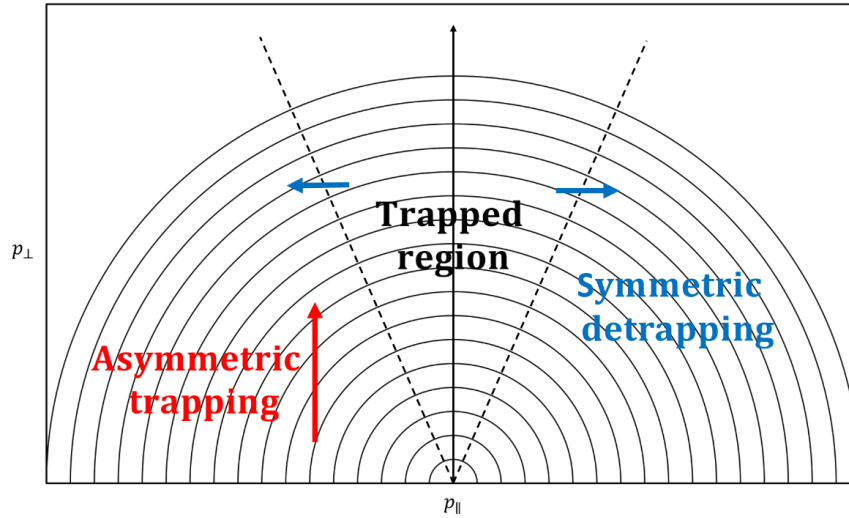
Figure 1.9: Symmetric detrapping and asymmetric trapping illustration.

Toroidal injection angle

The efficiency of ECCD is reliant on the parallel refractive index $N_\parallel$ with respect to the wave frequency ω. Intiuitively, an increase in $N_\parallel$ causes the Electron Cyclotron wave to resonate with higher energy electrons. This, in turn, enhances the current-carrying capacity of the wave. However, this effect is counteracted by a decrease in the number of high-energy electrons. Thus, there exists an optimal finite value for $N_\parallel$, corresponding to an optimal toroidal angle for EC injection [45].

1.3.2. Runaway generation

In a tokamak, the current carried by the plasma must exceed a certain technical threshold known as the Alfvén current, which typically has a value of 17kA. In a fusion reactor, the tokamak current will typically have to be three orders of magnitude larger than the Alfvén current. Under normal conditions, the bulk electrons in the plasma serve as the primary current carriers, with electron thermal velocities far exceeding the average plasma velocity. However, in certain cases, a small fraction of highly supra-thermal electrons may become significant or even dominant current carriers. This is due to the fact that the friction force decreases with increasing electron speed for fast electrons The phenomenon of acceleration arises when the magnitude of the force applied to an electron by a macroscopic electric field exceeds the magnitude of the braking force caused by collisions with other particles within the plasma. As a result, these electrons can undergo "unlimited" acceleration by an electric field, an effect first predicted in 1925 and now known as the *runaway* phenomenon

[21].

The earliest comprehensive description of electron runaway was provided in 1959 by Dreicer [34, 35] who considered a homogeneous plasma consisting of electrons and ions in thermal equilibrium. From the Fokker-Planck kinetic theory, an equation was derived that characterizes the temporal evolution of the average momentum exhibited by electrons in a plasma subjected to an external electric field and collisions, namely

$$\frac{\partial p_\parallel}{\partial t} + eE_\parallel = -p_{th}\nu_{ee}\Psi(p) \tag{1.19}$$

where $\nu_{ee} = e^4 m_e n_e \ln\Lambda/4\pi\varepsilon_0^2 p_{th}^3$ is the thermal electron collision frequency, $\ln\Lambda$ is the Coulomb logarithm[7], $p_{th} = \sqrt{2m_e T_e}$ is the thermal momentum and the function $\Psi(p)$ describes the energy-dependence of the collisional friction as depicted in figure 1.10. The
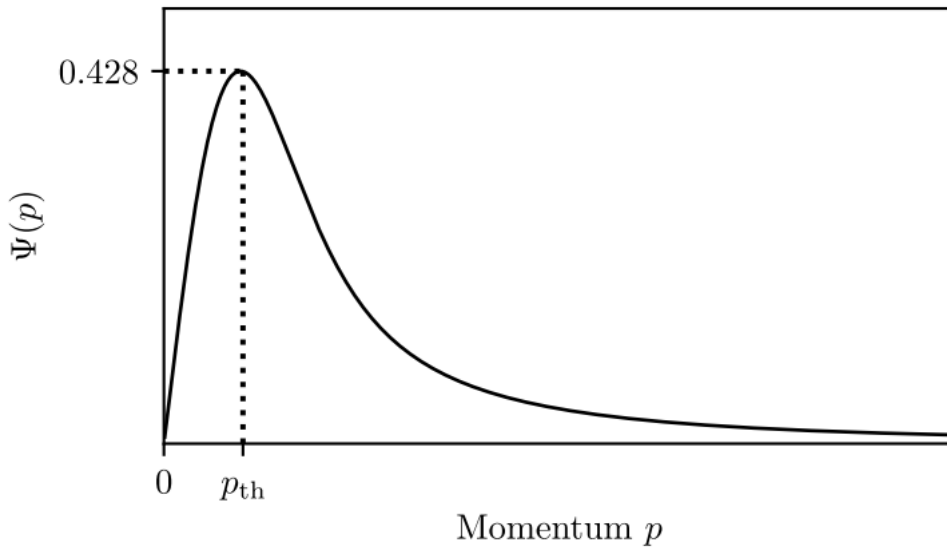
Figure 1.10: Graphical representation of the dimensionless function $\Psi(p)$, which describes the momentum-dependent nature of the collisional friction force that an electron undergoes within a plasma [53].

function Ψ exhibits a monotonically increasing behavior as a function of p until the momentum p_{th} is reached, beyond which it decreases. In the limit as p approaches infinity, the function $\Psi(p) \approx p_{th}^2/(mv)^2$ while decreasing in magnitude as v^{-2}. Ultimately, the function approaches a small but non-zero value as the velocity tends to the speed of light c.

If one normalizes the equation (1.19) to $2p_{th}\nu_{ee}$, it is possible to express the electric field

---

[7]It is a plasma parameter that for applications related to runaway electrons in tokamaks reaches values between 10 and 20.

term as $E_\parallel/E_D$ with $E_D = 2p_{th}\nu_{ee}/e$ called the *Dreicer field*. This peculiar field constitutes a threshold value of strength above which electron runaway can be used to characterize the electric field above which all electrons runaway, since the maximum of Ψ is independent of temperature. As a result of the decreasing trend displayed by $\Psi(p)$ for $p > p_{th}$, any electron that reaches sufficiently high velocity for the electric field to overcome the collisional friction will exhibit unbounded acceleration. Consequently, an electron moving with $v \gg v_{th} = p_{th}/m_e$ will undergo runaway behavior when the electric field exceeds a certain critical value, namely

$$eE_\parallel \geq p_{th}\nu_{ee}\Psi(p) \approx \nu_{ee}\frac{p_{th}^3}{m_e^2 v^2} = \frac{e^4 n_e \ln\Lambda}{4\pi\varepsilon_0^2 m_e v^2}. \tag{1.20}$$

It is noteworthy that owing to the fundamental speed limit imposed by the speed of light c, electrons will not exhibit runaway behavior when the electric field intensity is below the critical threshold value

$$E_c = \frac{e^4 n_e \ln\Lambda}{4\pi\varepsilon_0^2 m_e c^2} = \frac{T_e}{mc^2}E_D. \tag{1.21}$$

Using the relativistic relation between velocity and momentum, it is also possible to calculate, for a given $E_\parallel$ the minimum critical speed of the slowest runaway electrons as

$$\frac{v_c}{c} = \sqrt{\frac{E_c}{E_\parallel}} \iff \frac{p_c}{m_e c} = \frac{1}{\sqrt{E_\parallel/E_c - 1}}. \tag{1.22}$$

The maximum value of $\Psi(p)$ corresponds to a critical value of the electric field $E_\parallel$, above which all electrons in the plasma will undergo instantaneous runaway behavior:

$$eE_\parallel \geq p_{th}\nu_{ee}\max\left(\Psi(p)\right) \approx 0.428 p_{th}\nu_{ee} = 0.214 eE_D, \tag{1.23}$$

so that if $E_c < E_\parallel < 0.214E_D$, not all the electrons will be immediately accelerated, but only a fraction. In a plasma system, collisions work to maintain the electron distribution in a state of thermal equilibrium. This means that any gaps in the distribution created by runaway electrons will be filled by collisional diffusion processes, resulting in a gradual leaking of particles into the velocity region above the threshold value (v_c). Consequently, the bulk component of the distribution will gradually lose particles, leading to the conversion of all electrons to runaways, even at electric field values lower than the threshold value of $0.214eE_D$. This diffusive leakage of particles into the runaway region is known as the Dreicer runaway generation mechanism. While this is a common mechanism for

generating runaway electrons, any particle with a velocity greater than v_c will be continuously accelerated and run away, regardless of its past. This includes interactions such as electron-electron knock-on collisions, radioactive β-decay of elements producing energetic electrons (i.e tritium in tokamaks), and collisions with cosmic radiation.

A comprehensive investigation of the implications of runaway electrons (REs) in tokamaks necessitates a wider perspective that incorporates other pertinent physics. The high inductance of the system implies that the electric field cannot be considered a constant, as it varies considerably with the evolution of the REs, while altering the current is a more challenging task. Consequently, a simultaneous analysis of the kinetics of the REs and the changing electric field must be given priority in the research.

1.4. Electron Cyclotron Emission Diagnostics

Electron cyclotron emission (ECE) is produced by the resonant radiation emission by electrons as they gyrate in a magnetic field with a frequency around multiple integers n of the cyclotron frequency Ω_c. ECE is observed in the upper microwave to lower terahertz frequency range of magnetically confined fusion plasmas for electrons moving with velocities $v \ll c$, and its detection requires the ability to measure spectral intensities at around $\sim 1\,\mathrm{pW}/(\mathrm{m}^2 \cdot \mathrm{Hz} \cdot \mathrm{srad})$. While these specifications present technical challenges, the potential of ECE diagnostics to offer measurements of cyclotron emission with high temporal resolution makes this technique highly attractive both for fast electron studies and electron temperature reconstruction. ECE diagnostics can be found at nearly all magnetically confined fusion facilities, including JET [64, 80, 82] , ASDEX Upgrade [27, 78], DIII-D [4, 85, 89], W7-X [79], LHD [65, 71], KSTAR [62], and TCV [10, 12, 61]. In ECE, it is important to distinguish between the high-field side (HFS) and low-field side (LFS). In fact, since in a tokamak $B \propto 1/R$, the magnetic field on the HFS has a greater strength, while the LFS has a lower strength than the magnetic field at the center of the plasma. The spectral intensity I_ω measured at a frequency ω can be mapped to a unique position where the resonance condition $\omega = n\Omega_c(R_{\mathrm{cold}})$ is met, as the cyclotron frequency is distinct for each radial position. Neglecting the finite velocity of electrons in a plasma, this position is referred to as the *cold resonance* position.

1.4.1. Vertical ECE diagnostics

Over the years, ECE has been successfully used to diagnose plasma parameters such as electron temperature and density fluctuations. However, obtaining quantitative information on the non-thermal electron population can be challenging when using a horizontal
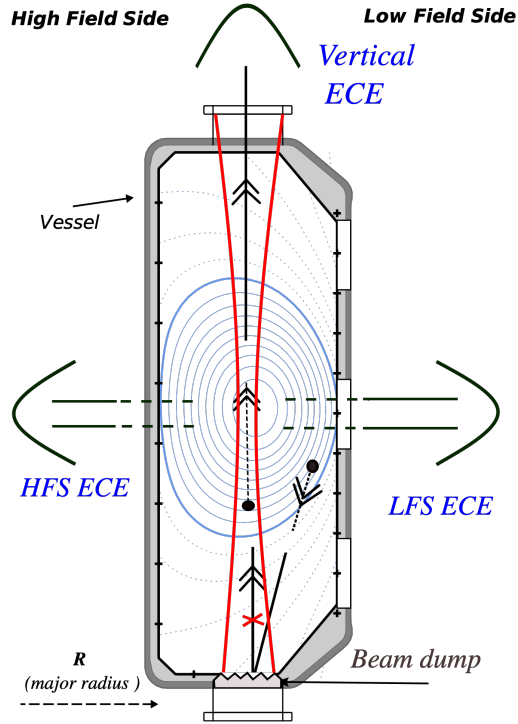
Figure 1.11: Illustration of the different ECE configurations on TCV [8]

line of sight. This is due to the difficulty in determining the energy of non-thermal electrons, which makes it complicated to attribute the radiation to a specific radial location in the plasma.

Horizontal lines of sight can cause radiation from non-thermal electrons to originate in different regions depending on electron energy. A vertical line of sight can avoid this issue. Additionally, the Vertical ECE configuration allows for a more direct determination of electron energies, as the ECE spectrum broadening due to the magnetic field gradient can be reduced. In fact, since the tokamak magnetic field scales as $\sim 1/R$, if one fixes the radial position, the electron cyclotron frequency in the weakly relativistic limit is proportional to

$$\omega_{\text{ece}} \propto \frac{n}{\gamma}. \tag{1.24}$$

Therefore, the frequency of the VECE is determined only by the harmonic number and the energy of the electrons. When the radiation can be attributed to a single harmonic, any broadening in frequency can be attributed to energy broadening alone. This allows a direct calculation of electron energy from the frequency of the emitted radiation.

In the 1980s and 1990s, works on PLT [50], ALCATOR [60], and TORE SUPRA [43, 44] focused on the Vertical ECE configuration for the characterization of non-thermal

electrons. However, this configuration also has its limitations. For example the emission from non-thermal electrons can compete with thermal radiation from different regions in the plasma at the same frequency, especially if the line of sight is not isolated from wall reflected radiation. To mitigate this issue, retro-reflectors or microwave beam dumps can be used at the termination of the line of sight. However, isolation of the line of sight can be challenging if the refraction in the plasma shifts the line of sight out of the dump or retro-reflector. Additionally, density or frequency constraints may be necessary to limit the effect of refraction. In the early 1990s, Vertical ECE studies on DIII-D [59] were limited to higher frequencies to mitigate the effects of plasma refraction, which resulted in severe harmonic overlap.

This diagnostic has the potential to resolve the lower energies of the distribution and can be particularly useful for studying non-thermal electrons created during electron cyclotron current drive (ECCD) or for runaway electrons of energies in the order of a few hundreds of keV [8].

1.5.   Thesis Outline

This work focuses on the study of suprathermal electron dynamics in the TCV tokamak by modelling the ECE. The development of a new ECE synthetic diagnostic (the YODA code) accounting for arbitrary numerical distributions is the main outcome of this master thesis. To calculate the ECE synthetic intensity for any arbitrary line of sight, YODA takes in input different quantities:

- The magnetic equilibrium reconstructed by the LIUQE code;

- Raytracing parameters calculated by the C3PO code;

- The numerical electron distribution function calculated by the 3D bounce-averaged Fokker-Planck code LUKE.

After this general introduction (**chapter 1**), the thesis develops as follow:

In **chapter 2:** *Electron Cyclotron Emission and Absorption Modelling*, starting from the general description of electromagnetic phenomena in matter, the theory of electron cyclotron emission is presented. Also, the radiation transport equation is derived and the wave propagation of electromagnetic waves in weakly inhomogeneous media is described. At the end, the Fokker-Planck equation is presented.

In **chapter 3:** *Experimental setup*, the main characteristics of the TCV tokamak, along with its electron cyclotron resonance heating system and its vertical ECE diagnostic is

described.

In **chapter 4:** *ECE numerical modelling*, all the modelling efforts needed to simulate the resonant EC emission and (re)absorption processes are detailed. The chapter starts from the description of the raytracing code C3PO used to model the vertical ECE antenna pattern. Then it goes through the description of relevant features of the 3D bounce-averaged Fokker-Planck code LUKE needed to calculate the electron distribution function in non-thermal plasma scenarios. Then, the implementation and the thermal validation of the new ECE synthetic diagnostic (the YODA code) is detailed.

In **chapter 5:** *Suprathermal electrons at the tokamak à configuration variable*, YODA is used to simulate some vertical ECE measurements from two ECCD shots (#73217 and #72644).

2 | Electron Cyclotron Emission and Absorption Modelling

This chapter offers a thorough description of the theory of electron cyclotron emission and absorption. Section 2.4 describes the fundamental principles that form the basis of this theory. To provide a complete understanding, section 2.1 employs the linear description of electromagnetic phenomena to systematically review all the theory's basic components. This includes examining wave propagation in a weakly inhomogeneous medium, as outlined in section 2.2, and introducing the radiation transport equation, discussed in section 2.3. Additionally, section 2.4.3 presents the theory of blackbody emission for thermal plasmas, and the chapter concludes with an overview of the theoretical description of non-thermal electron distribution functions. In this thesis, this is accomplished through solving the Fokker-Planck equation using the LUKE code, as described in section 2.5.

2.1. Linear Description of Electromagnetic Phenomena

In the study of physical processes within matter, it is often necessary to consider a large number of particles at a macroscopic level. This allows for the treatment of the medium as a continuous entity, disregarding the underlying discrete nature of the microscopic components. Maxwell's equations in conjunction with source terms provide a comprehensive and adequate explanation of the electromagnetic phenomena that occur within:

$$\nabla \cdot \boldsymbol{E}(\mathbf{r}, t) = \frac{\rho_{\text{ext}}(\mathbf{r}, t) + \rho_{\text{int}}(\mathbf{r}, t)}{\varepsilon_0}, \tag{2.1a}$$

$$\nabla \cdot \mathbf{B}(\mathbf{r}, t) = 0, \tag{2.1b}$$

$$\nabla \times \mathbf{E}(\mathbf{r}, t) = -\frac{\partial \mathbf{B}(\mathbf{r}, t)}{\partial t}, \tag{2.1c}$$

$$\nabla \times \mathbf{B}(\mathbf{r}, t) = \mu_0(\mathbf{J}_{\text{ext}}(\mathbf{r}, t) + \mathbf{J}_{\text{int}}(\mathbf{r}, t)) + \frac{1}{c^2}\frac{\partial \mathbf{E}(\mathbf{r}, t)}{\partial t}. \tag{2.1d}$$

These equations link the macroscopic fields $\mathbf{E}$ and $\mathbf{B}$ at the position $\boldsymbol{r}$ at time t to the sources that created them, as defined in terms of the spatial charge density ρ and the current density $\mathbf{J}$. The symbols ρ_{ext} and $\mathbf{J}_{\text{ext}}$ denote the external sources, whereas ρ_{int} and $\mathbf{J}_{\text{int}}$ indicate the sources internal to the medium. The electric permittivity and magnetic permeability of empty space are ε_0 and μ_0 respectively, and c is the speed of light.

The continuity equation, that can be obtained by combining equations 2.1a and 2.1d,

$$\frac{\partial \rho}{\partial t} + \nabla \cdot \mathbf{J} = 0, \tag{2.2}$$

states that the amount of electric charge in any volume of space can only change by the amount of electric current flowing into or out of that volume through its boundaries,therefore it implies the charge conservation.

However, without appropriate initial and boundary conditions, this mathematical problem is not complete. Furthermore, it is also needed to make sure to have enough independent equations to solve the system for all of the unknowns. This last requirement underlines a severe missing ingredient in the problem: the connection between the electromagnetic fields and the properties of the medium one is dealing with. The system, therefore, is not closed, but one can address this issue under suitable and general assumptions. In fact, it is feasible to establish a theory for the linear response of the medium, since a linear relation between fields and the media may be sufficient to adequately describe a vast class of phenomena.

In the most general case, according to linear electrodynamics, this relation between fields and sources can be taken into account by writing the constitutive relations

$$\mathbf{P}(\mathbf{r}, t) = \int_V \int_{-\infty}^t \underline{\underline{\chi}}(\mathbf{x}, \mathbf{x'}, t, t') \cdot \mathbf{E}(\mathbf{x'}, t') \mathrm{d}^3 x' \mathrm{d} t', \tag{2.3}$$

$$\mathbf{J}(\mathbf{r}, t) = \int_V \int_{-\infty}^t \underline{\underline{\sigma}}(\mathbf{x}, \mathbf{x'}, t, t') \cdot \mathbf{E}(\mathbf{x'}, t') \mathrm{d}^3 x' \mathrm{d} t', \tag{2.4}$$

$$\mathbf{D}(\mathbf{r}, t) = \int_V \int_{-\infty}^t \underline{\underline{\varepsilon}}(\mathbf{x}, \mathbf{x'}, t, t') \cdot \mathbf{E}(\mathbf{x'}, t') \mathrm{d}^3 x' \mathrm{d} t', \tag{2.5}$$

where $\underline{\underline{\chi}}$ is the electric susceptibility tensor, $\underline{\underline{\sigma}}$ is the electric conductivity tensor and $\underline{\underline{\varepsilon}}$ is the dielectric tensor (or permittivity), while $\boldsymbol{P}$ and $\boldsymbol{D}$ are the polarization vector and electric displacement vector, respectively.

The relations 2.4 - 2.5 are characterized by non-locality both in time, such that the value of a quantity at a particular time instant is dependent on the electric field at previous times instants, and spatial locations, where the properties at a certain point in space are contingent upon the properties of other points. This results in the manifestation of *spatial* and *temporal* dispersion.

In fact, since matter has a finite inertia when responding to a given field, the phenomenon of temporal dispersion may appear an intuitive idea. The medium's reaction will thus not be instantaneous, and this attribute appears to be reasonably common among most materials. A non-locality in space refers to the capability of the medium to transmit information from one point to another. For example, electromagnetic phenomena can do this by using charged particles that move within the body with a specific characteristic length that is related to the medium considered.

This description may be confined to the scenario of a homogeneous medium. By assuming spatio-temporal periodic perturbations, the Fourier analysis of equation (2.4) can be performed with the unperturbed state defined as $E = 0$ and $B = B_0$. This enables the description of the medium's behavior in terms of monochromatic waves in both time and space. Since in the remainder of this section, all the equations live in the Fourier space, for convenience, from now on the dependence of $\boldsymbol{E}$ and $\boldsymbol{B}$ on the wave vector $\mathbf{k}$ and the frequency ω are left implicit. At this point it is possible to Fourier transform Maxwell's equations in order to turn them into algebraic equations:

$$\mathbf{k} \cdot \mathbf{E} = -\frac{i}{\epsilon_0}(\rho_{\text{ext}} + \rho_{\text{int}}), \tag{2.6a}$$

$$\mathbf{k} \cdot \mathbf{B} = 0, \tag{2.6b}$$

$$\mathbf{k} \times \mathbf{E} = \omega\mathbf{B}, \tag{2.6c}$$

$$\mathbf{k} \times \mathbf{B} = -i\mu_0(\mathbf{J}_{\text{ext}} + \mathbf{J}_{\text{int}}) - \varepsilon_0\mu_0\omega\mathbf{E}. \tag{2.6d}$$

By multiplying equation (2.6c) with $\boldsymbol{k}$ from the left and substituting in equation (2.6d), it is possible to find the *wave equation* in Fourier space

$$\frac{c^2}{\omega^2}\mathbf{k} \times (\mathbf{k} \times \mathbf{E}) + \mathbf{E} = -\frac{i\omega_0 c^2}{\omega}(\mathbf{J}_{\text{ext}} + \mathbf{J}_{\text{int}}). \tag{2.7}$$

Introducing the *dispersion tensor*

$$\underline{\underline{\Lambda}} = N^2\left(\frac{\boldsymbol{kk}}{k^2} - \underline{\underline{I}}\right) + \underline{\underline{\varepsilon}}, \tag{2.8}$$

where $\mathbf{N}$ is the *refractive index* vector

$$\mathbf{N} = \frac{c}{\omega}\mathbf{k}, \tag{2.9}$$

and $\underline{\underline{I}}$ is the unit tensor, it is possible to derive the equation

$$\underline{\underline{\Lambda}} \cdot \boldsymbol{E} = \frac{i\mu_0 c^2}{\omega}\boldsymbol{J}_{\text{ext}}. \tag{2.10}$$

In the absence of external currents, i.e. $J_{\text{ext},i} = 0$, equation (2.10) reduces to

$$\underline{\underline{\Lambda}} \cdot \boldsymbol{E} = \mathbf{0}. \tag{2.11}$$

With equation (2.11) the description of the macroscopic electromagnetic fields in matter has been formulated as a homogeneous set of equations in the electric field $\mathbf{E}$. In order to find a non-trivial solution to equation (2.11), the condition that the determinant $\underline{\underline{\Lambda}}$ be zero must be imposed

$$\det(\underline{\underline{\Lambda}}) = 0. \tag{2.12}$$

This is the so called *dispersion relation* which, for a given frequency ω, defines the possible refractive index N.

The refractive index can be decomposed, with respect to the local direction of the magnetic field $\hat{\boldsymbol{b}} = \boldsymbol{B_0}/B_0$, in cylindrical components $N_\parallel = \boldsymbol{N} \cdot \hat{\boldsymbol{b}}$ and $N_\perp = ||\boldsymbol{N} \times \hat{\boldsymbol{b}}||$. Therefore, the dispersion relation can be solved for either $\omega(N_\parallel, N_\perp)$, $N_\parallel(\omega, N_\perp)$ or $N_\perp(\omega, N_\parallel)$. By finding the eigenvectors of the wave equation it is possible to determine the polarization of the eigenmodes.

In general, the condition $\det(\boldsymbol{\Lambda}) = 0$ leads to a complex perpendicular refractive index $N_\perp = N_{\perp,\text{r}} + N_{\perp,\text{i}}$ if the quantities ω and $N_\parallel$ are assumed to be real[1]. The dispersion tensor $\boldsymbol{\Lambda}$ con be decomposed into its hermitian and anti-hermitian parts $\boldsymbol{\Lambda} = \boldsymbol{\Lambda}^H + i\boldsymbol{\Lambda}^A$, where $\boldsymbol{\Lambda}^H = (\boldsymbol{\Lambda} + \boldsymbol{\Lambda}^\dagger)/2$ and $\boldsymbol{\Lambda}^A = (\boldsymbol{\Lambda} - \boldsymbol{\Lambda}^\dagger)/2i$. When $|\Lambda_{ij}^A| \ll |\Lambda_{ij}^H|$, the *weak damping approximation* (or WKB approximation) can be exploited [31, 74].

---

[1]$N_{\perp,\text{r}}$ and $N_{\perp,\text{i}}$ are respectively the real and the imaginary parts of $N_\perp$.

2.2. Wave Propagation in a Weakly Inhomogeneous Medium

Now it is possible to continue the discussion with an examination of a weakly inhomogeneous medium in which radiation is transmitted, leading to the formulation of a suitable approximation in which it is possible to associate a trajectory to the radiation passing through a plasma, referred to as the geometric optics approximation.

In the WKB approximation, it can be shown [74] that $|N_{\perp i}| \ll |N_{\perp r}|$ and $|N_{\perp r}|$ can be determined by solving the approximate wave equation

$$\mathbf{\Lambda}^H(N_{\perp r}) \cdot \mathbf{E}_k = 0 \tag{2.13}$$

with the corresponding dispersion relation $\Lambda^H = det\mathbf{\Lambda}^H = 0$. The time-averaged density of the energy flow is

$$\boldsymbol{S} = -\frac{\epsilon_0 c}{4} \frac{\mathrm{d}}{\mathrm{d}\boldsymbol{N}} \left(\boldsymbol{E}_k^* \cdot \Lambda \cdot \boldsymbol{E}_k \right) \tag{2.14}$$

and the time averaged density of dissipated power P can be expressed as

$$P = \frac{\epsilon_0 \omega}{2} \boldsymbol{E}_k^* \cdot \mathbf{\Lambda}^A \cdot \boldsymbol{E_k} \tag{2.15}$$

The ray damping is mainly related to the imaginary part of the wave vector that can be calculated by $N_{\perp i} = (c/2\omega)P/S_\perp$ with $S_\perp = \|\boldsymbol{S} \times \boldsymbol{b}\|$.

Exploiting the WKB approximation, from now on $\boldsymbol{k}$, $\boldsymbol{N}$ and $\boldsymbol{E}_k$ will refer to the zero-order solution of $\mathbf{\Lambda}^H(N_{\perp r}) \cdot \mathbf{E}_k = 0$ with respect to the small parameter

$$\delta \sim max(|\Lambda_{ij}^A|/|\Lambda_{ij}^H|) << 1 \tag{2.16}$$

and the dispersion relation $\mathbf{\Lambda}$ will refer to its Hermitian part $\mathbf{\Lambda}^H$. The advantage of the weak damping approximation is that within this framework it is possible to decouple the propagation and the absorption processes in the wave calculations.

The WKB asymptotic expansion enables the *ray-tracing* representation of wave propagation, allowing wave characteristics – such as the conductivity tensor, group velocity, and Fourier space description – that are typically applicable to uniform plasmas to be taken into account locally in a slowly inhomogeneous plasma. For these kind of media, the necessary conditions to be satisfied are that $L \gg \lambda = 2\pi/|\boldsymbol{k}|$ and $t \gg T = 2\pi/\omega$ where L and t are the characteristic spatial and temporal scales of the inhomogeneities [40].

The first step to derive the the equations which describe the ray trajectory is to introduce the *eikonal* function[2] $\Psi(\mathbf{r}', t)$ such that

$$\mathbf{k}(\mathbf{r}', t) = \nabla \Psi(\mathbf{r}', t), \quad \omega(\mathbf{r}', t) = -\frac{\partial \Psi(\mathbf{r}', t)}{\partial t}. \tag{2.17}$$

Using this function it is possible to express the fields and the sources as oscillating functions both in space and in time:

$$\mathbf{E}(\mathbf{r}', t) = \frac{1}{2} \left(\mathbf{E}_0(\mathbf{r}', t) e^{i\Psi(\mathbf{r}', t)} + \mathbf{E}_0^*(\mathbf{r}', t) e^{-i\Psi^*(\mathbf{r}', t)} \right) \tag{2.18}$$

$$\mathbf{J}(\mathbf{r}', t) = \frac{1}{2} \left(\mathbf{J}_0(\mathbf{r}', t) e^{i\Psi(\mathbf{r}', t)} + \mathbf{J}_0^*(\mathbf{r}', t) e^{-i\Psi^*(\mathbf{r}', t)} \right) \tag{2.19}$$

where the complex conjugate is indicated by an asterisk. In this context, the quantities $\mathbf{E}_0$, $\mathbf{J}_0$ and k are slowly varying functions in space and time, i.e., their relative variation is of the order of $\delta \ll 1$ within a single spatial or temporal oscillation, where

$$\delta = \frac{2\pi}{\omega} \left| \frac{1}{\eta} \frac{\partial \eta}{\partial \eta} \right| + \frac{2\pi}{|\boldsymbol{k}|} \left| \frac{1}{\eta} \nabla \eta \right| \tag{2.20}$$

and $\eta(\boldsymbol{r}, t)$ is a scalar function characterizing the plasma. Under these assumptions, keeping only terms up to first order during the linearization of the Maxwell's equations, the wave equation and the dispersion relation obtained for the case of uniform medium can be found, but with the difference that now $\boldsymbol{k}$, ω and Λ are explicit functions of the position $\boldsymbol{r}$ and the time t [40], so that the dispersion equation $\det \Lambda(\boldsymbol{k}, \omega, \boldsymbol{r}, t) = 0$ is a first order non-linear differential equation in Ψ.

The coordinates k_j of the wavevector $\boldsymbol{k}$ and the coordinates r_i of the position vector $\boldsymbol{r}$ have to be canonically conjugate because the eikonal function Ψ is independent of the choice of the ray trajectory. For the same reason, also the frequency ω and the time t are canonically conjugate.

Remembering the Hamilton canonical equations for a single particle, where the action S, the hamiltonian H and the momentum $\boldsymbol{p}$ are related by

$$\boldsymbol{p} = \frac{\partial S}{\partial \boldsymbol{r}} \qquad H = -\frac{\partial S}{\partial t}, \tag{2.21}$$

---

[2]The assumption that the surface of constant phase of the propagating wave is a smooth function in space is made by introducing the wave vector as the gradient of the phase, which adds a further restriction on the applicability of the WKB approximation. If the wave absorption occurs after an integration period that is longer than the maximum Liapunov exponent, which describes the rate of separation of infinitesimally close trajectories, the ray tracing has thus lost its physical significance [74].

and the first derivative with respect to time of position and momentum are

$$\frac{\mathrm{d}\boldsymbol{r}}{\mathrm{d}t} = -\frac{\partial H}{\partial \boldsymbol{p}}, \tag{2.22}$$

$$\frac{\mathrm{d}\boldsymbol{p}}{\mathrm{d}t} = -\frac{\partial H}{\partial \boldsymbol{r}} \tag{2.23}$$

By equating the eikonal function Ψ with the action S, the wave frequency ω with the Hamiltonian H, and the wave vector $\boldsymbol{k}$ with the momentum $\boldsymbol{p}$, it is possible to establish a correlation between wave propagation, under geometric optics approximation, and particle motion. Following the Hamiltonian formalism, the general form of the *ray equations* can be expressed as

$$\frac{d\mathbf{r}}{dt} = -\left(\frac{\partial \Lambda/\partial \mathbf{k}}{\partial \Lambda/\partial \omega}\right)_{\Lambda=0} \tag{2.24}$$

$$\frac{d\mathbf{k}}{dt} = \left(\frac{\partial \Lambda/\partial \mathbf{r}}{\partial \Lambda/\partial \omega}\right)_{\Lambda=0} \tag{2.25}$$

$$\frac{d\omega}{dt} = -\left(\frac{\partial \Lambda/\partial t}{\partial \Lambda/\partial \omega}\right)_{\Lambda=0} \tag{2.26}$$

The trajectory $\mathbf{r}(t)$ travelled by the wave with the group velocity $\mathbf{v}_g = \partial\omega/\partial\mathbf{k}$ can be obtained from equation (2.24) , while eqs. (2.25) and (2.26) are related to the variations that $\mathbf{k}$ and ω have to experience in order to satisfy the dispersion relation.

In this thesis, equations (2.24)-(2.26) are solved using the C3PO code, the details of which will be discussed in more detail in section 4.1.

2.2.1. Cold Plasma Dispersion Relation

By solving the ray equations (2.24)-(2.26) it is possible to calculate the wave trajectory through the plasma, assuming to know the dispersion relation form. The numerical calculation of the dispersion relation is outside the scope of this thesis, in fact it is carried out in a special module of the LUKE-C3PO suite which calculates it under the assumptions associated with a *cold magnetised plasma*. In the following section, only the analytical treatment of this problem is considered.

Referring to a cold magnetized plasma, with the magnetic field $\boldsymbol{B_0}$ oriented along the z

axis, it is possible to demonstrate that the dielectric tensor reduces to [83]:

$$\varepsilon = \begin{pmatrix} \varepsilon_1 & -i\varepsilon_2 & 0 \\ i\varepsilon_2 & \varepsilon_1 - N^2 & 0 \\ 0 & 0 & \varepsilon_3 \end{pmatrix} \tag{2.27}$$

where

$$\varepsilon_1 = 1 - \frac{X}{1 - Y^2}, \qquad \varepsilon_2 = \frac{XY}{1 - Y^2}, \qquad \varepsilon_3 = 1 - X \tag{2.28}$$

and

$$X = \frac{\omega_p^2}{\omega^2}, \qquad Y = \frac{\Omega_c}{\omega}. \tag{2.29}$$

By respecting the coordinate system such that the wave vector $\boldsymbol{k}$ lies in the xz plane, one can write the dispersion tensor as

$$\underline{\underline{\Lambda}} = \begin{pmatrix} \varepsilon_1 - N_\parallel^2 & -i\varepsilon_2 & N_\parallel N_\perp \\ i\varepsilon_2 & \varepsilon_1 - N^2 & 0 \\ N_\parallel N_\perp & 0 & \varepsilon_3 - N_\perp^2 \end{pmatrix} \tag{2.30}$$

and then setting the determinant equal to zero $det(\underline{\underline{\Lambda}}) = 0$, the dispersion relation can be found as

$$A \cdot N_\perp^4 + B \cdot N_\perp^2 + C = 0 \tag{2.31}$$

where A,B and C are coefficient functions of the dielectric tensor elements defined as follows:

$$A = \varepsilon_1 \tag{2.32a}$$

$$B = (\varepsilon_1 + \varepsilon_3) N_\parallel^2 - [(\varepsilon_1 + \varepsilon_2)(\varepsilon_1 - \varepsilon_2) + \varepsilon_1\varepsilon_3] \tag{2.32b}$$

$$C = \varepsilon_3(N_\parallel^2 - (\varepsilon_1 + \varepsilon_2))(N_\parallel^2 - (\varepsilon_1 - \varepsilon_2)) \tag{2.32c}$$

After that, the dispersion function may be factored as

$$\Lambda = \varepsilon_1 \Lambda_+ \Lambda_- = \varepsilon_1 (N^2 - N_+^2)(N^2 - N_-^2), \tag{2.33}$$

where

$$N_\pm^2 = 1 - X - \frac{1}{2}XY^2 \frac{1 + N_\parallel^2 \pm \sqrt{(1 - N_\parallel^2)^2 + 4N_\parallel^2(1 - X)/Y^2}}{1 - X - Y^2} \tag{2.34}$$

are the two roots of the equation. The solution N_- is known as the Ordinary mode (O) because it is described by the same dispersion relation as an isotropic medium and corresponds to a fully transversal wave in perpendicular propagation with the electric field

aligned to the external magnetic field. The wave that is connected to the solution N_+ is known as the eXtraordinary mode (X), and it contains both transverse and longitudinal components in its electric field, which is parallel to the external magnetic field. These are the 2 main polarizations of an electron cyclotron wave and they are thoroughly described in the next section.

When computing the trajectory of cyclotron waves with ray and beam tracing codes, it is customary to ignore kinetic effects since, in most cases, the cold dielectric tensor is adequate to characterize the ray paths in a plasma [36–38]. While the aforementioned method may generally yield accurate results, it is important to cite that the impact of kinetic effects turns out to be non negligible in close proximity to cut-off layers, especially as the refractive index approaches a purely imaginary value. [67].

If the electrons are fast (at least in weakly relativistic regime), the electron cyclotron waves can propagate even when the refractive index determined by the cold dispersion relation is purely imaginary. In Ref [88], it is shown that the propagation near a resonance layer can be different from the cold dispersion approximation, due to kinetic *warm* plasma effects. Actually, most of the beam and ray-tracing codes still use the cold plasma dispersion relation [37, 38, 74] since that there are two main problems in the calculation of the ray path from a dielectric tensor which takes into account relativistic effects:

- Near a resonance layer, the group velocity of the wave and the real part of the refractive index approach zero [88];

- A numerical approach is needed to calculate the fully relativistic dispersion relation, since an analytical solution does not exist;

Nevertheless, because the spatial length of the resonance is typically small compared to the total length of the ray path (in ECE measurements in tokamak plasmas) the distortion of the ray trajectory caused by resonances is negligible [86], therefore using the cold plasma dispersion relation is an acceptable approximation.

2.2.2.   EC Waves Polarizations in magnetized plasmas

In general, the the lines-of-sight of electron cyclotron emission (ECE) diagnostics are not straight because the radiation is susceptible to refraction. The polarization of the wave affects how much light is refracted. Electron cyclotron waves can have two separate, decoupled polarization states in the cold plasma approximation, indicating with θ the angle formed between the wave vector and the magnetic field [16, 33]:

- If $\theta = \pi/2$ (perpendicular polarization), the polarization mode is called the *eX-*

traordinary mode (X) and the electric field $\boldsymbol{E}$ of the wave is perpendicular to the equilibrium magnetic field $\boldsymbol{B_0}$;

- If $\theta = 0$ (parallel polarization) the polarization mode is the *ordinary mode (O)* where $\boldsymbol{E}$ is parallel to $\boldsymbol{B_0}$;

In the vacuum limit, both modes are just transverse and linearly polarized. In a plasma, this is only true for the ordinary mode, whereas the extraordinary mode produces a longitudinal contribution to $\boldsymbol{E}$ that is parallel to the wave vector $\boldsymbol{k}$, and it is therefore elliptically polarised.

Both of the fundamental modes must be transverse and circularly polarized in both a vacuum and a plasma in the case of $\theta = 0$. Thus, there are two polarized waves: the *right-handed* polarized wave, for which $\boldsymbol{E}$ rotates in the direction of electron gyration, and the *left-handed* polarized wave, for which $\boldsymbol{E}$ rotates in the direction of ion Larmor motion.

The eXtraordinary mode shifts into the right-handed mode for $\omega > \omega_p$ when the angle θ of propagation is continuously varied from $\pi/2$ to 0, while the ordinary mode becomes the left-handed. Except for in one specific case, the X-mode is almost always more strongly coupled to the plasma than the O-mode. Therefore the former mode is called the *strong* mode, while the second one is called the *weak* mode.

Formally, the names X-mode and O-mode only apply to propagation perpendicular to the magnetic field. Today this nomenclature is however also applied to arbitrary propagation directions, and this generalization will also be applied in this thesis for the purpose of simplicity [33].

2.2.3. EC Waves Accessibility

The wave's ability to propagate trhough the plasma is dependent on the value of N^2, where N^2 and $N^2 = \infty$ correspond to *cutoff* and *resonance*, respectively. To determine the wave's accessibility, cutoffs and resonances are plotted on the CMA diagram (Figure 2.1).

X-mode injection is more complex than O-mode injection due to the R-cutoff when launching from the low field side. Launching the fundamental resonance X-mode wave from the high field side results in a density cutoff twice that of O-mode. However, this is challenging in practice due to tokamak geometry. To overcome these limitations, second harmonic X-mode heating can be adopted from the low field side by doubling the injection frequency.
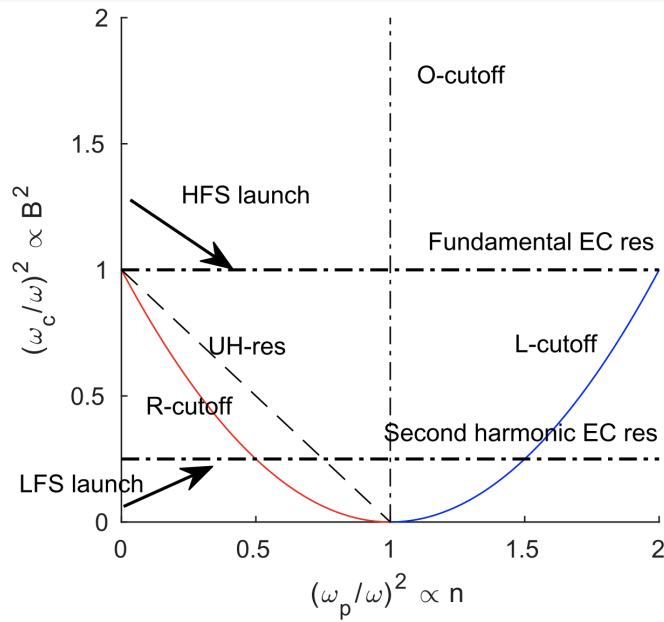
Figure 2.1: CMA diagram

2.3. The Radiation Transport Equation

Having described how to model the electromagnetic radiation trajectory and how its group velocity and wave vector changes as it propagates through a weakly inhomogeneous material, in this section the main purpose is to point out the theory describing how the energy carried by a wave can evolve. In the geometric optics approximation, wherein the wave propagation is described using rays, it is possible to derive an energy conservation law called *radiation transport equation*. To understand its main aspects, it is necessary to at least summarize its derivation [5].

Consider, to start with, a cylindrical volume element of an optical inhomogeneous medium, as shown in Figure (2.2). A radiation beam of intensity I_ω and solid angle $\mathrm{d}\Omega_1$ enters one face of the cylinder at an angle ξ_1 to the normal **n**. The incoming beam is bent due to the medium's inhomogeneity, therefore the radiation that exits has an angle of $\xi_2 \neq \xi_1$ and an intensity $I_\omega + \mathrm{d}I_\omega$ within a solid angle $\mathrm{d}\Omega_2$. Assuming that the medium is loss free and that there are no sources or sink terms for the radiation, it is possibile to write the energy balance:

$$(I_\omega + \mathrm{d}I_\omega)da \, \cos(\xi_2)\mathrm{d}\Omega_2\mathrm{d}\omega - I_\omega da \cdot cos(\xi_1)\mathrm{d}\Omega_1\mathrm{d}\omega = 0 \qquad (2.35)$$

which corresponds to the energy conservation equation for radiation propagating along a bunch of rays. If the medium is homogeneous, the considered wave obeys Snell's law of
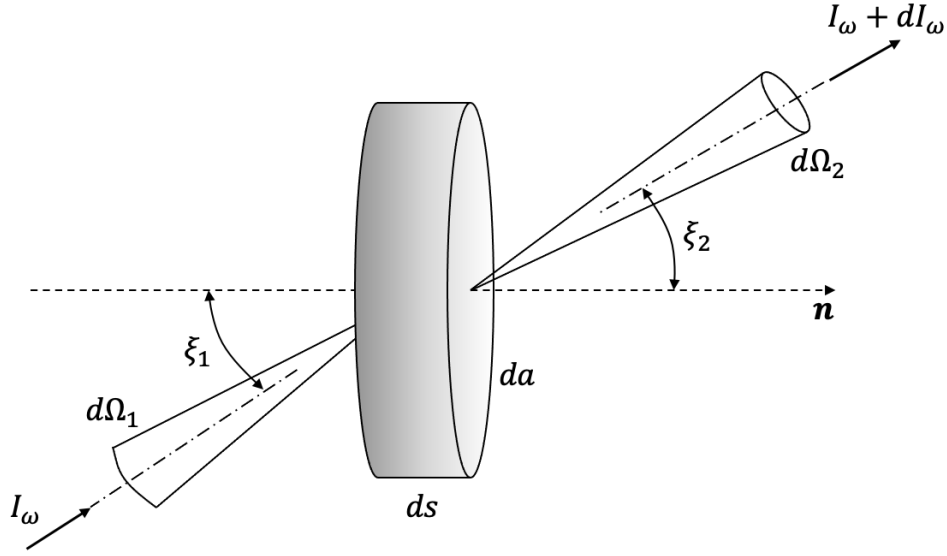
Figure 2.2: Radiation entering a small volume of plasma and leaving it after experiencing a little degree of refraction because to a variation in refractive index values on the two sides of the elementary cylinder.

refraction

$$N_2 \sin(\xi_2) = N_1 \sin(\xi_1) \tag{2.36}$$

where N_1 and N_2 are the refraction index of the 2 sides of the cylindrical volume.

In these conditions (isotropic medium and lossless), it is found that

$$N^2 \, \mathrm{d}a \, cos(\xi) \, \mathrm{d}\Omega = \text{const.} \tag{2.37}$$

so that, from equation (2.35), the classical result of geometrical optics is obtained [5]:

$$\frac{I_\omega}{N^2} = \text{const.} \tag{2.38}$$

Keep in mind that $I_\omega = constant$ is valid along a ray propagating in vacuum, and it is independent of the observer's distance from the source. This property makes this quantity highly useful in describing the emission properties of radiating bodies.

By relaxing the assumption of a homogeneous body, for an anisotropic medium Snell's law holds only for certain waves propagating in certain unique directions relative to the static magnetic field: a generalization of equation (2.38) is then necessary.

To proceed into the derivation, the technique outlined in [5] uses the analogy between the ray trajectory and Hamilton's equations expanded to an ensemble of many particles, and an expression equivalent to (2.37) is found:

$$N_r^2 \, \mathrm{d}a \, cos(\xi) \, \mathrm{d}\Omega \; = \; constant \tag{2.39}$$

where N_r is called *ray refractive index*, as

$$N_r^2 = \left| N^2 sin(\theta) \frac{\sqrt{1 + \left(\frac{1}{N}\frac{\partial N}{\partial \theta}\right)^2}}{\frac{\partial}{\partial \theta}\left[\frac{cos(\theta) + \left(\frac{1}{N}\frac{\partial N}{\partial \theta}\right)sin(\theta)}{\sqrt{1 + \left(\frac{1}{N}\frac{\partial N}{\partial \theta}\right)^2}}\right]} \right| \tag{2.40}$$

where θ is the angle formed by the wave vector $\mathbf{k}$ and the external magnetic field $\mathbf{B_0}$. The meaning of the ray refractive index is different from that of the refraction index: $\mathbf{N}$ describes the ray trajectory along the wave vector $\mathbf{k}$, while $\mathbf{N_r}$ is related to the energy flux along the group velocity $\mathbf{v_g}$ of the wave. At this point, the energy conservation equation for an anisotropic medium leads to

$$\frac{I_\omega}{N_r^2} = constant. \tag{2.41}$$

This equation describes the transfer of radiation in an anisotropic passive media which neither emits, absorbs nor scatters radiation.

Since every real physical process involves a loss of energy, such lossy media should also be considered. These types of media can support spontaneous electric and magnetic oscillations and thus they are capable of absorbing and emitting radiation.
The quantity of interest in the study of radiation transport is the spatial variation of the energy flux. One can do so by proceeding to use the dispersion equation (2.31) to obtain the complex value of k (for real ω). Thus, the exponential decrease in the amplitude of the wave is specified by $-\mathrm{Im}(k)$ where the minus sign comes from a proper definition of the Fourier components as $\exp(i\omega t - i\mathbf{k} \cdot \mathbf{r})$. What is called *absorption coefficient* α_ω is twice the imaginary part of the wave vector, but since $\mathbf{k}$ and $\mathbf{v}_g/|\mathbf{v}_g|$ can make an angle $\beta \neq 0$, the decrease in intensity along the ray trajectory can be written as

$$\alpha_\omega(s) = -2\,\mathrm{Im}(k)\,cos\beta \tag{2.42}$$

where s denotes the point along the ray path. α has the dimensions of reciprocal length

$[L^{-1}]$. In the transport equation, the absorption of energy experienced by the rays is given by

$$-\alpha_\omega\, I_\omega\, \mathrm{d}s\, \mathrm{d}a\, cos\xi\, \mathrm{d}\Omega\, \mathrm{d}\omega \tag{2.43}$$

If the considered volume is also a source of radiation, an emissivity coefficient j_ω can be introduced as the power generated per unit volume of medium per frequency interval $\mathrm{d}\omega$ per steradian, which is flowing along the ray path. Its contribution to the energy balance can be expressed as

$$j_\omega\, \mathrm{d}s\, \mathrm{d}a\, cos\xi\, \mathrm{d}\Omega\, \mathrm{d}\omega \tag{2.44}$$

Finally, inserting the sum of (2.43) and (2.44)– the net power produced or consumed in the volume – in the right-hand side of the energy balance equation (2.35) and using the relation $N_\mathrm{r}^2\, \mathrm{d}a\, cos\xi\, \mathrm{d}\Omega = const$, a relation between the absorption and emission characteristics of the medium and the evolution of radiation intensity along the ray path may be found. It is called the *radiation transport equation* (or equation of radiation transfer):

$$\frac{\mathrm{d}}{\mathrm{d}s}\left(\frac{I_\omega(s)}{N_{\omega,r}^2(s)}\right) = \frac{1}{N_{\omega,r}^2(s)}\left(j_\omega(s) - \alpha_\omega(s)I_\omega(s)\right) \tag{2.45}$$

The goal of this thesis is to solve equation (2.45) numerically. Before doing so, however, some additional physical insight can be gained by manipulating the equation analytically. In fact, defining the *source function*:

$$S_\omega(s) = \frac{1}{N_{\omega,r}^2(s)}\frac{j_\omega(s)}{\alpha_\omega(s)} \tag{2.46}$$

and the *optical depth*:

$$\tau(s) = -\int_L^s \alpha_\omega(s')ds' \tag{2.47}$$

where the distance travelled by the ray path is L. Using this, equation (2.45) can be rewritten as

$$\frac{\mathrm{d}}{\mathrm{d}\tau}\left(\frac{I_\omega(s)}{N_{\omega,r}^2(s)}\right) = \frac{I_\omega(s)}{N_{\omega,r}^2(s)} - S_\omega(s). \tag{2.48}$$
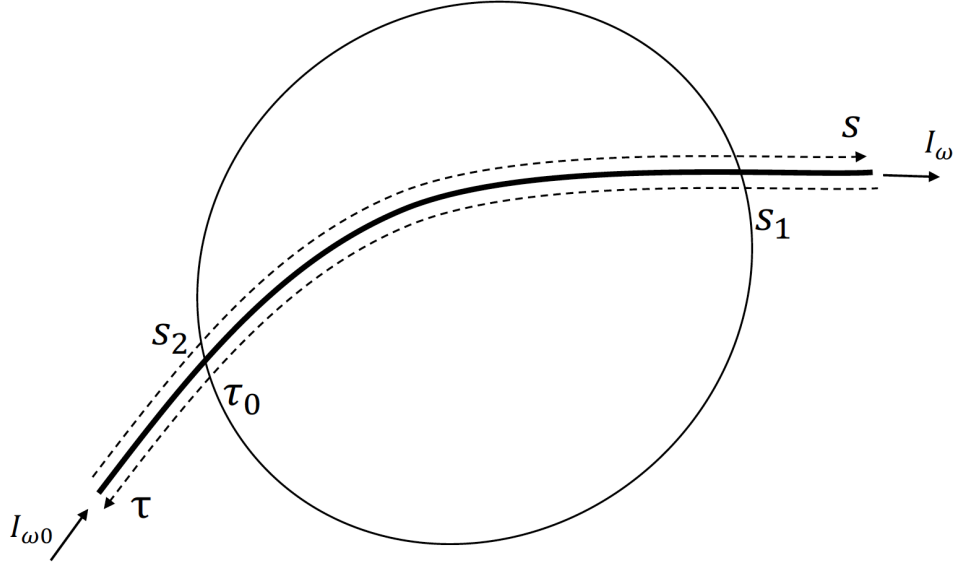
Figure 2.3: Schematic representation of the ray path s and the optical depth τ through a certain plasma volume. The optical depth is measured from the point of emergence.

In this form, it is trivial to integrate it along the ray path s to get

$$\frac{I_\omega(s_2)}{N_{\omega,r}^2(s_2)}e^{-\tau(s_2)} = \frac{I_\omega(s_1)}{N_{\omega,r}^2(s_1)}e^{-\tau(s_1)} + \int_{\tau(s_1)}^{\tau(s_2)} S_\omega(s)e^{-\tau}d\tau \qquad (2.49)$$

In this case s_1 is the point in which the ray leaves the plasma, while s_2 is the one in which it enters, therefore $\tau(s_2) = \tau(s_1) = \tau_0$ and $N_{\omega,r}^2(s_2) = N_{\omega,r}^2(s_1) = 1$. Since the intensity of the ray in the position in which it enters in the plasma is $I_\omega(s_2) = I_{\omega,0}$, the emerging intensity along the ray could be expressed as:

$$I_\omega = I_{\omega,0}e^{-\tau_0} + \int_0^{\tau_0} S_\omega(\tau)e^{-\tau}d\tau \qquad (2.50)$$

The observed intensity is expressed by this equation as the product of the emission at all interior points along the ray, decreased by a factor $e^{-\tau}$ expressing the re-absorption by the intervening material, and the intensity of the radiation incident from behind, also lowered by absorption [40].

All contributions coming from outside the medium, as well as radiation emanating from the body further away from the collecting optics are dampened if $\tau(s_1) - \tau(s_2) >> 1$.

Typically, it is assumed that radiation emitted from plasma regions where $\tau > 2$ will be nearly entirely reabsorbed before it reaches the collection optics. Therefore, only

radiation emitted from regions where $\tau < 2$ will effectively contribute to the collected radiation intensity for a broadened ECE layer. In fact, if $\tau > 2$ plasmas are considered to be *optically thick* for the specified frequency [42]. Since in that case, the plasma is perfectly absorbing at the considered frequency, it emits like a *blackbody*.

2.3.1. Plasma Optical Thickness Effects

The plasma optical thickness τ_0 affects which approximations are allowed when solving the radiation transport equation [40]:

- If $\tau_0 << 0$, it means that the plasma is *optically thin* and then the absorption can be considered negligible. In this case, the presence of the plasma has essentially no effect on the emitted radiation, and therefore:

$$I(\omega) \simeq I_0 + \frac{\omega^2}{8\pi^3 c^2} \int_0^L \frac{j(\omega, s)}{N_{\omega,r}^2} \mathrm{d}s. \tag{2.51}$$

  There is no re-absorption effect, and the observed intensity is effectively the sum of the emission contributions from all of the volume elements along the ray plus the incoming radiation due to reflections;

- If $\tau_0 \sim 1$ the intensity attenuation due to absorption cannot be neglected since the factor $exp(-\tau_0)$ this is not small enough. In that case in equation (2.50) has to be considered, which means that also the details of the incoming radiation I_0 is of importance.

- If $\tau_0 >> 1$ the plasma is said to be *optically thick* and the re-absorption processes are strong. For this scenario, the incident radiation can be neglected up to a spatial position in the plasma where $\tau_0 \geq 1$. The expression for the observed intensity simply reduces to

$$I(\omega \approx \int_0^L j_\omega(s) e^{-\tau(s)} \mathrm{d}s. \tag{2.52}$$

2.4. Electron Cyclotron Absorption and Emission

After having described both the propagation of the EC waves and their transport of energy, the aim here is to present a general theory explaining how a magnetically confined plasma responds to radiation at frequencies around the electron cyclotron harmonics $n\Omega_c$. The complete treatment includes a detailed discussion of the phenomena of absorption and emission of radiation in a weakly inhomogeneous medium and the derivation of the

current and the correlation tensors within the relativistic kinetic theory framework. Only the final expressions of the absorption and of the emission coefficient are provided in this section.

Calculating the EC absorption coefficient $\alpha_\omega(s)$ and emission coefficient $j_\omega(s)$ is a necessary step to solve the radiation transport equation (2.45). The collective motion of the electrons may be disregarded in a tenuous plasma when dispersion is negligible, and the emissivity and absorption coefficient can be computed as the sum of the contributions from each electron. To make these calculations rigorously the refractive index must satisfy $N_\omega \sim 1$ because the total emissivity is expressed as the momentum space integral of the single electron emissivity weighted with the electron distribution function [54]. However, for the plasma scenarios and frequency range in which the ECE is useful, this condition is in general not met [33]. For the purposes of this thesis, a suitable approximation for the absorption coefficient can be found in literature [2, 16, 17].

In the weak damping approximation, the collisionless absorption of electromagnetic waves can be treated using the Poynting theorem. Therefore the absorption coefficient along the direction of the energy flux $\boldsymbol{s} = \boldsymbol{S}(\boldsymbol{k}, \omega)/|\boldsymbol{S}(\boldsymbol{k}, \omega)|$ can be expressed as [16]

$$\alpha_\omega(s) = \frac{\omega}{4\pi} \frac{\boldsymbol{E}^* \cdot \boldsymbol{\varepsilon_a} \cdot \boldsymbol{E}}{|\boldsymbol{S}(\boldsymbol{k}, \omega)|} \tag{2.53}$$

where the Fourier transform of the undamped wave electric field is $\boldsymbol{E} = \boldsymbol{E}(\boldsymbol{k}, \omega)$, while $\boldsymbol{\varepsilon_a}$ is the anti-Hermitian part of the dielectric tensor $\boldsymbol{\varepsilon} = \boldsymbol{\varepsilon_h}(\boldsymbol{k}, \omega) + i\boldsymbol{\varepsilon_a}(\boldsymbol{k}, \omega)$, and $\boldsymbol{\varepsilon_h}$ is its Hermitian part .

For what concerns the energy $\boldsymbol{S}(\boldsymbol{k}, \omega)$, it is useful to remember that it is composed of 2 components: the Poynting flux that represents the flow of electromagnetic energy and the sloshing flux which is thought to arise from particles moving coherently with the wave:

$$\boldsymbol{S}(\boldsymbol{k}, \omega) \equiv \frac{c}{4\pi} \Re(\boldsymbol{E} \times \boldsymbol{B}^*) - \frac{\omega}{8\pi} \frac{\partial \varepsilon_{h,ij}}{\partial \boldsymbol{k}} E_i^* E_j \tag{2.54}$$

Except for the O-mode at $\omega = \Omega_c$ and the X-mode around $\omega = 2\Omega_c$ when $(\omega_p/\omega)^2 > 1$, the sloshing flux for EC waves is small in comparison to the Poynting vector[3], therefore the sloshing flux can be neglected. It should be noted that equations (2.53) makes no mention of the group velocity, hence it is assumed that this formulation will be true even when the dielectric tensor quickly changes with the wave frequency, as it does near the resonance [17].

---

[3]The sloshing flux is important only if non-zero finite temperature effects are included in the dispersion relation.

Since the resonances in the EC range occur at different harmonics of the cyclotron frequency Ω_c, the total anti-Hermitian part of the fully relativistic dielectric tensor [18] has to be expressed as the sum of each n'th harmonic contribution is $\varepsilon_a = \sum_{n=1} \varepsilon_a^{(n)}$, where

$$\varepsilon_a^{(n)} = -\pi \left(\frac{\omega_p}{\omega}\right)^2 \int \frac{d^3p}{\gamma} \delta\left(\gamma - N_\| p_\| - \frac{n\Omega_c}{\omega}\right) \boldsymbol{V_n V_n^*} \cdot \hat{R}_n f(p_\|, p_\perp) \qquad (2.55)$$

and $\int \mathrm{d}^3p = 2\pi \int_0^{+\infty} p_\perp dp_\perp \int_{-\infty}^{+\infty} dp_\|$ indicates the momentum space average and $f(p_\|, p_\perp)$ the electron distribution function in the momentum space $(p_\|, p_\perp)$. Furthermore, the electron momentum $\boldsymbol{p} = p_\| \hat{\boldsymbol{b}} + \boldsymbol{p}_\perp$ is normalized to the thermal momentum $p_{th} = m_e c$. Furthermore

$$\boldsymbol{V_n} = \frac{1}{N_\perp} \frac{n\Omega_c}{\omega} \left(J_n, \frac{ib}{n} J_n', \frac{\omega}{n\Omega_c} N_\perp p_\| J_n\right) \qquad (2.56)$$

$$\hat{R}_n = \frac{n\Omega_c}{\omega} \frac{1}{p_\perp} \frac{\partial}{\partial p_\perp} + N_\| \frac{\partial}{\partial p_\|} \qquad (2.57)$$

with $J_n = J_n(b)$ the Bessel function of the first kind of order n (which is the harmonic number), the argument $b = \frac{\omega}{\Omega_c} N_\perp p_\perp$, $J_n' = dJ_n/db$ and $f(p_\|, p_\perp)$ is the electron distribution function which has the dimensions of (phase-space) density [17].

Now by inserting the equation (2.55) into equation (2.53) it is possible to retrieve the absorption coefficient for the n-th harmonic expressed as an integral in a cylindrical, dimensionless momentum space:

$$\alpha_\omega^{(n)}(s) = -2\pi^2 \frac{\omega_{p,0}^2}{c_0 \omega} \int \int \left(\frac{n}{\bar{\omega} N_\perp}\right)^2 \left|\left(\tilde{e}_x + \frac{\bar{\omega} N_\perp}{n} p_\| \tilde{e}_z\right) J_n(b) - \frac{ib}{n} J_n'(b) \tilde{e}_y\right|^2 \times$$
$$\hat{R} f(s, p_\perp, p_\|) \times \qquad (2.58)$$
$$\delta\left(\gamma - p_\| N_\| - \frac{n}{\bar{\omega}}\right) \frac{p_\perp}{\gamma} dp_\perp dp_\|$$

keeping in mind that the absorption coefficient (2.58) is a local quantity (dependent on the position s along the ray) for a plasma in a weakly inhomogeneous magnetic field.

On the other hand, the equation (2.9) of Ref. [87] may be used to calculate the emissivity of the n-th harmonic from the absorption coefficient expressed by equation (2.58):

$$j_\omega^{(n)}(s) = m_e c_0^2 \frac{N_{\omega,r}^2 \omega_{p,0}^2 \omega}{4\pi c_0^3} \int \int \left(\frac{n}{\bar\omega N_\perp}\right)^2 \left|\left(\tilde e_x + \frac{\bar\omega N_\perp}{n}p_{||}\tilde e_z\right)J_n(b) - \frac{ib}{n}J_n'(b)\tilde e_y\right|^2 \times$$

$$f(s, p_\perp, p_{||}) \times \quad (2.59)$$

$$\delta\left(\gamma - p_{||}N_{||} - \frac{n}{\bar\omega}\right)\frac{p_\perp}{\gamma}dp_\perp dp_{||}.$$

In both the equations (2.58) and (2.59), the relativistic factor is $\gamma = \sqrt{1 + p_{||}^2 + p_\perp^2}$, while $\bar\omega = \frac{\omega}{\Omega_c}$ and the vector $\tilde e = (\tilde e_x, \tilde e_y, \tilde e_z)$ is the polarization vector. Perhaps, the most important feature of these equations is that $f(s, p_{||}, p_\perp)$ can be any arbitrary electron distribution function, locally dependent on the ray position s: this allows the use of a numerical distribution function, as will be further discussed in next chapters.

For what concerns the coordinate system, it follows the Stix convention, where k is located in the x-z plane , and the z axis is aligned with B (Figure 2.4):

$$\boldsymbol{B}_0 = (0, 0, B_0), \quad \boldsymbol{k} = (k_x, 0, k_z)$$
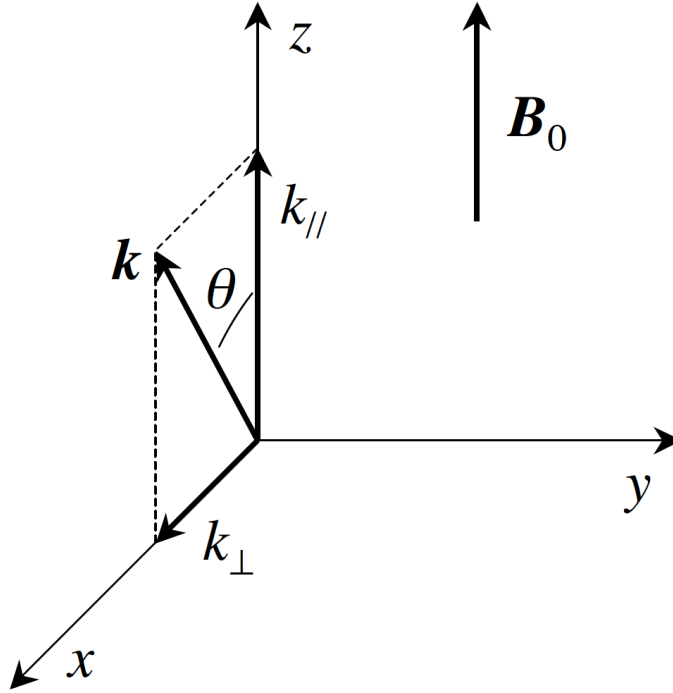
Figure 2.4: Cartesian coordinate system in relation with the orientation of the magnetic field **B** and the wave vector **k** (the Stix convention).

Therefore, the *polarization vector* $\tilde{e} = (\tilde{e}_x, \tilde{e}_y, \tilde{e}_z)$ follows this coordinate system and it is expressed as the electric field normalized by the modulus of the poynting flux. It is also important to underline that all the quantities derived from the cold plasma dispersion relation, namely $N_\parallel$, $N_\perp$, N_ω and $\tilde{e}$ are intrinsically dependent on the ray poisition s. Summing up all the contributions for the different harmonics, it is possible to find the global absorption coefficient $\alpha_\omega(s)$ and emissivity $j_\omega(s)$:

$$\alpha_\omega(s) = \sum_{n=1}^{+\infty} \alpha_\omega^{(n)}(s) \;\; , \;\; j_\omega(s) = \sum_{n=1}^{+\infty} j_\omega^{(n)}(s) \tag{2.60}$$

In conclusion, the emissivity and the absorption coefficient can be seen as the composition of two different contributions weighted by the electron distribution function or its directional derivative in the momentum space: the *polarization filter* and the *relativstic resonance condition*.

2.4.1. Polarization Filter

The factor
$$|\tilde{e} \cdot V_n^*|^2 = \left(\frac{n}{\bar{\omega} N_\perp}\right)^2 \left| \left(\tilde{e}_x + \frac{\bar{\omega} N_\perp}{n} p_\parallel \tilde{e}_z\right) J_n(b) - \frac{ib}{n} J_n'(b) \tilde{e}_y \right|^2 \tag{2.61}$$

takes into account the finiteness of the electron Larmor radius as well as the wave polarization [2]. Once the cold plasma dispersion relation is calculated along the ray path it is also possible to calculate the absolute value of the polarization vector as the eigenvector of the wave equation in the Fourier space, namely the equation (2.11), as

$$\tilde{e} = (E_x, -iE_y, E_z), \tag{2.62}$$

normalized to the modulus of the poynting flux. The equation (2.62) contains two components: the $E_x - iE_y$, which corresponds to the right-handed polarization and is associated with the electric field perpendicular to the magnetic field B_0, and the linear polarization E_z, aligned with the equilibrium magnetic field direction [17].

2.4.2. Relativistic EC Resonance Condition

As is possible to observe from the expressions of $\alpha_\omega(s)$ and $j_\omega(s)$, because of the presence of a delta function in both formulas, not all the electrons described by the distribution function $f(p_\parallel, p_\perp)$ contribute to the integral. In fact, the ECE resonance condition may be expressed as follows and has to be fulfilled in order for a particle to contribute to the

integrals:

$$\gamma - n\frac{\Omega_c}{\omega} - N_\| p_\| = 0. \tag{2.63}$$

From this expression it is clear that the electron cyclotron emission and absorption processes involve only the portion of the electron population which fulfills (2.63) in the momentum space.

Since this condition is a direct consequence of the conservation of energy and momentum, it is possible to rewrite the expression (2.63) as

$$\omega - k_\| v_\| = \frac{n\Omega_c}{\gamma} \tag{2.64}$$

in fact, since the electrons are moving along the magnetic field lines, when the frequency ω of the wave, Doppler shifted by the factor $k_\| v_\|$, matches an integer multiple of the cyclotron frequency Ω_c corrected by the relativistic γ factor, the interaction between those electrons and the waves occurs.

Since $\gamma = \sqrt{1 + p_\perp^2 + p_\|^2}$, for the electron cyclotron waves which $|N_\|| < 1$ the resonance condition makes a half ellipse in momentum space $(p_\|, p_\perp)$ [33]:

$$p_\perp(p_\|) = \sqrt{\left(N_\| p_\| + \frac{n\Omega_c}{\omega}\right)^2 - p_\|^2 - 1} \tag{2.65}$$

This resonance half-ellipse exists only if

$$n\frac{\Omega_c}{\omega} \geq \sqrt{1 - N_\|^2} \tag{2.66}$$

where the equal sign corresponds to a null size ellipse [40]. For the full perpendicular propagation, when $N_\| = 0$ all the electrons have the same energy because the resonance condition reduces to

$$\gamma = n\frac{\Omega_c}{\omega} \tag{2.67}$$

It is then clear that, for $N_\| = 0$, only the relativistic effects can explain the wave-particle interaction. There is a pole in momentum space and a non-zero anti-hermitian part of the dielectric tensor in the wave-particle resonance[17]. Referring to Figure (2.5), the energy of the resonating electrons is different between perpendicular $(N_\| = 0)$ and oblique $(N_\| \neq 0)$ propagation [40]:

- If $(N_\| = 0)$, when $n\frac{\Omega_c}{\omega}$ increases, the interactions between waves and electrons occur first with low energy electrons and then with more energetic ones;
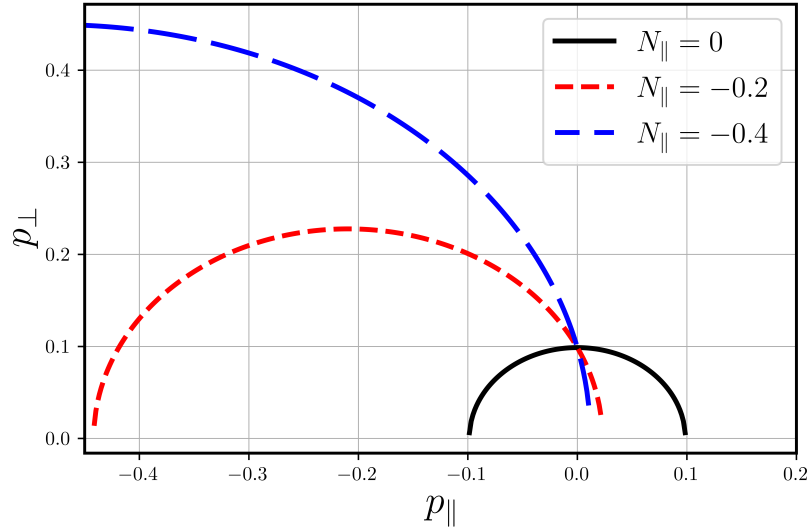
Figure 2.5: Plot for different $n\frac{\Omega_c}{\omega}$ of the resonance condition in the case of perpendicular propagation $N_\parallel = 0$ (in black) which is centered around $p_\parallel = 0$ and oblique propagation $N_\parallel = -0.2$ and $N_\parallel = -0.4$ (in red and blue) which is shifted towards positive $p_\perp$ with a bigger curvature radius.

- If $((N_\parallel \neq 0)$, interactions occur first with high energy particles and then with weakly energetic ones and then again with high energetic, but in the opposite half of the momentum space.

If one fixes a magnetic field strength and a propagation direction, it is possible to find a critical upper frequency

$$\omega_{\text{crit}} = n\Omega_c(1 - N_\parallel^2)^{-1/2} \tag{2.68}$$

so that there is electron cyclotron radiation only if $\omega < \omega_{\text{crit}}$. As $N_\parallel$ increases, corresponding to an increasing angle between the magnetic field and the wave propagation direction, this limit is shifted up (*frequency up-shift*).

On the other hand, if the frequency is fixed, it is also possible to find a critical value for the magnetic field at which the resonance occurs

$$B_{\text{crit}} = \frac{m_e c}{e}\frac{\omega}{n}(1 - N_\parallel^2)^{1/2}. \tag{2.69}$$

It sets a lower limit for the EC absorption and emission processes which occur only if $B > B_{\text{crit}}$. Since in a tokamak, the overall magnetic field strength varies radially roughly as $B(R) \propto 1/R$, where R is the major radius of the vacuum chamber coordinate, the resonance occurs only from a radius value $R = R_{\text{crit}}$ where $B(R_{\text{crit}}) = B_{\text{crit}}$. Also

this critical values up-shifts if $N_\parallel$ increases. This constrain constitutes a limit for the application of vertical LOS in the ECE operation, since the major radius R is fixed, while it isn't true for oblique and horizontal LOS.

2.4.3. Thermal Plasmas

The Maxwell-Jüttner distribution represents the distribution function, , it is normalized so that its momentum-space integral is one for a relativistic, thermal plasma:

$$f_{e,\mathrm{MJ}}(s, p_\perp, p_\parallel) = \frac{1}{4\pi\Theta K_2(1/\Theta)} \mathrm{e}^{-\gamma/\Theta} \tag{2.70}$$

where $\Theta = T_e/(m_e c_0^2)$ with T_e expressed in energy units, while K_l with order $l = 2$ denotes the modified Bessel function of the second kind, also referred to as the *MacDonald* function.

Since the main interest of this thesis is to study suprathermal electron populations described by distribution functions slightly different from the Maxwell-Jüttner, the calculations of the absorption coefficient and the emissivity, and then of the radiation intensity are allowed also for arbitrary numerical distribution functions. A more detailed description of the distribution functions used to obtain synthetic ECE intensities is presented in the next chapters.

If the plasma is in thermal equilibrium one can express the absorption coefficient as a function of the emissivity via the *Kirchhoff law*

$$I_{BB,\omega}(s) = \frac{1}{N_{\omega,r}^2}\frac{j_\omega(s)}{\alpha_\omega(s)} \simeq \frac{1}{N_{\omega,r}^2}\frac{\omega^2 T_e}{(2\pi)^3 c_0^2}. \tag{2.71}$$

The right hand side of the equation (2.71) is the so called *Rayleigh-Jeans* approximation for the emitted blackbody intensity $I_{BB,\omega}$ where the electron temperature is expressed in energy units.

In the case of blackbody emission (as discussed in section 2.3), the intensity source function (2.46) could be expressed as

$$S_\omega = \frac{\omega^2}{(2\pi)^3 c^2} T_{\mathrm{rad},\omega} \tag{2.72}$$

where $T_{rad,\omega}$ is also expressed in energy units and it is known as *radiation temperature*. Making use of the equation (2.46), this temperature can be expressed as a function of the

absorption and emission as

$$T_{\text{rad},\omega} = \frac{(2\pi)^3 c^2}{\omega^2} \frac{1}{N_{\omega,r}^2} \frac{j_\omega(s)}{\alpha_\omega(s)}. \tag{2.73}$$

Substituting the full expressions for the absorption coefficient (eq. (2.58)) and emissivity (eq. (2.59)) into equation (2.73) and considering a relativistic Maxwellian distribution function

$$T_{\text{rad},\omega} = -m_e c^2 \frac{\sum_n \int \int |\tilde{e} \cdot \boldsymbol{V}_n^*|^2 f_{e,\text{MJ}} \delta\left(\gamma - p_{||} N_{||} - \frac{n}{\omega}\right) \frac{p_\perp}{\gamma} dp_\perp dp_{||}}{\sum_n \int \int |\tilde{e} \cdot \boldsymbol{V}_n^*|^2 \hat{R} f_{e,\text{MJ}} \delta\left(\gamma - p_{||} N_{||} - \frac{n}{\omega}\right) \frac{p_\perp}{\gamma} dp_\perp dp_{||}} \tag{2.74}$$

Then equation (2.74) simplifies to

$$T_{\text{rad},\omega} = \Theta m_e c_0^2 = T_e \tag{2.75}$$

Therefore a thermal plasma follows the same Kirchhoff rule as a blackbody, because the source function S_ω which is the ratio between j_ω and α_ω, is proportional to the electron plasma temperature[54].

2.5.   Non-Thermal Plasmas

In certain plasma scenarios, the system deviates from thermal equilibrium, leading to a significant perturbation to the electron distribution. This section commences by outlining several mechanisms that result in the generation of fast electrons, which are particularly relevant to this thesis, followed by a succinct discussion on the kinetic modeling of non-thermal electron distribution functions.

2.5.1.   Fokker-Planck Modelling of the Non-Thermal Electron Distribution Function

Due to the computational limitations of describing a tokamak plasma using a single particle model, statistical methods have been devised which utilize a time-dependent equation to describe the evolution of the particle distribution function $f(t, x, v)$. In this thesis it is presented only an introduction to these complex topics, in fact for an in-depth understanding of these concepts, interested readers are directed towards relevant literature sources [49].

From Boltzmann Equation to Fokker-Planck Equation

A plasma kinetic theory can be developed by postulating that the forces acting on ions and electrons arise from the self-consistent electric and magnetic fields that they experience. Within the framework of kinetic theory, the total electric $\boldsymbol{E}$ and magnetic $\boldsymbol{B}$ fields, and also the distribution function f, are typically expressed through a perturbative first order expansion

$$\boldsymbol{E}(\boldsymbol{x},t) = \boldsymbol{E}_0(\boldsymbol{x},t) + \tilde{\boldsymbol{E}}(\boldsymbol{x},t) \tag{2.76a}$$

$$\boldsymbol{B}(\boldsymbol{x},t) = \boldsymbol{B}_0(\boldsymbol{x},t) + \tilde{\boldsymbol{B}}(\boldsymbol{x},t) \tag{2.76b}$$

$$f = f_0(\boldsymbol{x},\boldsymbol{p},t) + \tilde{f}(\boldsymbol{x},\boldsymbol{p},t) \tag{2.76c}$$

where the quantities labelled with a zero as a subscript indicate the averaged macroscopic components, while $|\tilde{\boldsymbol{E}}| \ll |\boldsymbol{E}_0|$, $|\tilde{\boldsymbol{B}}| \ll |\boldsymbol{B}_0|$ and $|\tilde{f}| \ll |f_0|$ are the microscopic fluctuating components, arising from particle interactions. The macroscopic distribution function[4] $f(t,x,p)\mathrm{d}x\mathrm{d}p$ is the number of particles in an infinitesimal phase-space volume x and p (i.e. the number of particles at position x and with momentum p). Since the macroscopic fields are described by the Maxwell equations (2.1),one needs to sum up the contributions from all particles, expressing the sources of the electromagnetic fields as the velocity (or momentum) moments of the electron distribution function as:

$$n(\boldsymbol{x},t) = \int f(\boldsymbol{x},\boldsymbol{p},t)d\boldsymbol{p} \tag{2.77a}$$

$$\mathbf{j}(\boldsymbol{x},t) = \frac{e}{m} \int \boldsymbol{p}f(\boldsymbol{x},\boldsymbol{p},t)d\boldsymbol{p}. \tag{2.77b}$$

This procedure is possible only because Maxwell's equations are a set of linear equations.

In the limit of a collisionless plasma, where the collisions between particles can be neglected, the evolution of the distribution function in time is governed by the Vlasov equation:

$$\frac{\partial f}{\partial t} + \frac{\boldsymbol{p}}{\gamma m}\frac{\partial f}{\partial \boldsymbol{x}} + q\left(\boldsymbol{E} + \frac{\boldsymbol{p}}{\gamma m} \times \boldsymbol{B}\right)\frac{\partial f}{\partial \boldsymbol{p}} = 0. \tag{2.78}$$

when collisions are accounted for, the Vlasov equation (2.78) can be modified to incorporate collisional effects by including a term that describes the resulting modification of the distribution function. This modified form of the equation is commonly known as the Boltzmann equation, or sometimes the Vlasov-Boltzmann equation and can be expressed

---

[4]Only electrons are considered in this thesis, so that all the quantities describe properties of the electron population.

as

$$\frac{\partial f}{\partial t} + \frac{\boldsymbol{p}}{\gamma m}\frac{\partial f}{\partial \boldsymbol{x}} + q\left(\boldsymbol{E} + \frac{\boldsymbol{p}}{\gamma m} \times \boldsymbol{B}\right)\frac{\partial f}{\partial \boldsymbol{p}} = C[f]. \tag{2.79}$$

The term $C[f]$ is known as *collision operator*. In the case when one treats collisions as dominated by long range Coulomb interaction, it is possible to say that the momentum exchange per each collision is small. This kind of operator is called a *Fokker-Planck* collision operator that can be expressed in an advection-diffusion form [53]

$$C[f] = \frac{\partial}{\partial \boldsymbol{p}}\left[-\boldsymbol{A}f + \mathbb{D}\frac{\partial f}{\partial \boldsymbol{p}}\right] \tag{2.80}$$

where from [6] and [20] is it possible to express the *dynamical friction coefficient* $\boldsymbol{A} = \sum_j \boldsymbol{A}_{ij}$ and the *diffusion coefficient* $\mathbb{D} = \sum_j \mathbb{D}_{ij}$. For example, Luke [30] solves a version of equation (2.73) which has been averaged over particle orbits. This average is known as a *bounce-average* and it is valid if the collision time is much longer than the poloidal transit time (i.e. the time it takes for a particle to return to the same poloidal angle)[5].

---

[5]More details about the involved timescales are provided in section 4.2

3 | Experimental Setup

In this chapter, the experimental framework employed in this thesis is outlined. In section 3.1, an overview is provided of the main characteristics of the Electron Cyclotron Heating system of TCV, which is of critical importance in the formation of suprathermal electrons. It is followed by a dedicated discussion one the Vertical-ECE diagnostic [8] developed and utilized on TCV (section 3.2).

3.1. The TCV Tokamak

The *Tokamak à Configuration Variable* (TCV) [51] is a medium sized, highly elongated tokamak device designed for the investigation of plasma shape effects on confinement and stability (see Figure 3.1). In operation since 1992, TCV allows the generation of a wide range of plasma shapes without the requirement for hardware modifications. The device's main operational parameters are comprehensively summarized in Table 3.1.

Parameter	Symbol	Value
Major radius	R_0	0.88 m
Minor radius	a	0.25 m
Aspect ratio	$\varepsilon = R_0/a$	~ 3.5
Vacuum vessel elongation	κ_{TCV}	2.9
Toroidal field on axis	B_0	<1.54 T
Plasma current	I_p	<1MA
Loop voltage	V_{LOOP}	<10 V
Disharge duration	/	<4 s

Table 3.1: Main TCV parameters

The TCV vessel's elongated design affords the ability to generate a wide range of plasma shapes, facilitated by the device's set of sixteen independently powered field coils. Through TCV's shaping capabilities, a broad spectrum of plasma configurations have been achieved, including highly elongated plasmas and negative triangularity arrangements, explored for the study of plasma confinement (see Figure 3.2) [52, 68, 69]. Furthermore, TCV has been utilized to examine the impact of plasma shaping on runaway electron beam formation
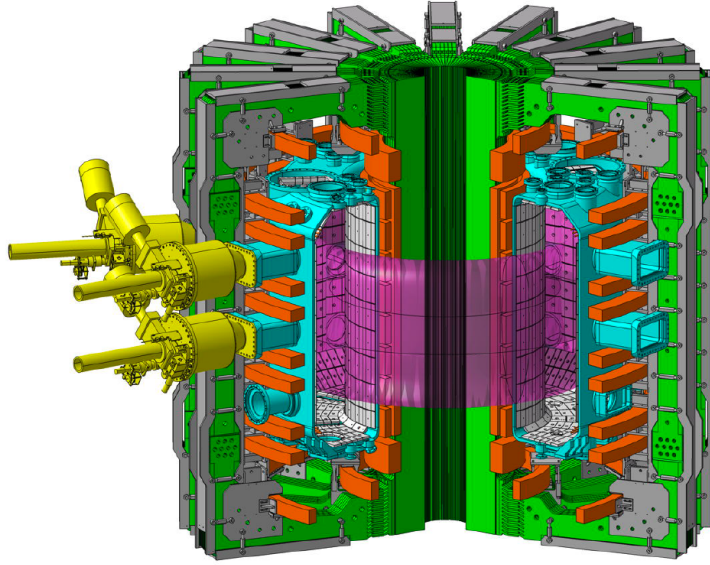
Figure 3.1: Schematic drawing of the TCV tokamak: ports for ECRH power injection (yellow), vacuum chamber and access ports (cyan), poloidal field coils and Ohmic transformer (orange), toroidal field coils (green), graphite-covered PFCs (white), plasma (pink).

[32] and to study electron transport enhancement by Electron-Cyclotron plasma-wave interaction [23].

The first wall of TCV is nearly entirely covered with graphite tiles, thereby making carbon the primary plasma impurity. The use of graphite as the main wall material has several advantages for fusion experiments, including its resistance to melting in vacuum and its ability to sublimate at temperatures above 3750 °C, leading to robustness against accidental plasma wall contact. Additionally, graphite is a low-Z material, meaning its radiation losses have a limited impact on core plasma performace, as opposed to high-Z materials such as tungsten. Despite its widespread use in fusion experiments, carbon is not suitable for use in a fusion reactor due to its high retention of hydrogen isotopes, which would result in significant amounts of tritium being retained in the reactor PFCs [22].

3.1.1. The TCV ECRH/ECCD System

TCV is equipped with a versatile Electron Cyclotron Resonance Heating (ECRH) and Electron Cyclotron Current Drive (ECCD) system [73]. This system comprises two gyrotrons, operating at a frequency of 82.7 GHz, with a nominal power output of 680 kW and three additional gyrotrons, operating at 118 GHz, with a nominal power output of 480 kW. Additionally, there are two dual frequency gyrotrons with a nominal power out-
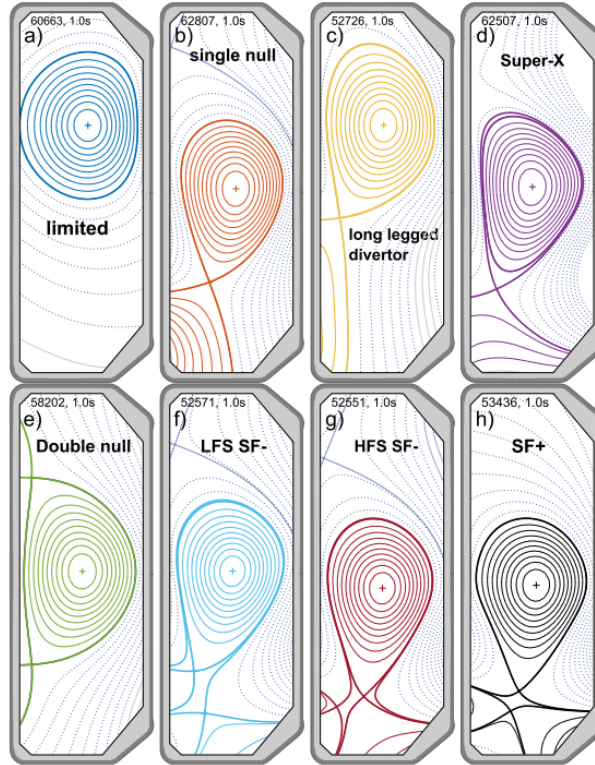
Figure 3.2: TCV shapes: a) limited plasma, b) conventional single null, c) long-lagged divertor, d) super-X, e) connected double null, f) LFS snowflake minus (SF-), g) HFS snowflake minus, h) snowflake plus (SF+)

put of $1000\,kW$, capable of heating at either $84\,GHz$ or $126\,GHz$. The total ECRH power installed on TCV is approximately $4800\,kW$ which is exceptionally high for a machine having a volume of approximately $4\,m^3$. The polarization of the electromagnetic wave injected by the gyrotrons is carefully selected to be in the X-mode, because it has been demonstrated that this polarization results in optimal power absorption. The heating of the plasma electrons provided by the gyrotrons is achieved through the cyclotron resonance at either the second (X2) or the third (X3) harmonic of the cyclotron frequency. These gyrotrons are connected to launchers, which serve the purpose of directing the beam into the plasma, and are positioned in the top ports, equatorial and upper-lateral ports as depicted in figure 3.3 .

The ECCD experiments conducted on TCV primarily utilize the (X2) gyrotrons, which are typically integrated with a launcher located at an equatorial port of the machine. In general, the desired radial location of the beam power deposition is regulated by the selected magnetic field value [73]. The toroidal and poloidal directions of the beam (in the reference frame of the plasma) are controlled by the launcher angles, specifically the toroidal angle, φ_L, and the poloidal angle θ_L . This last angle can be adjusted during
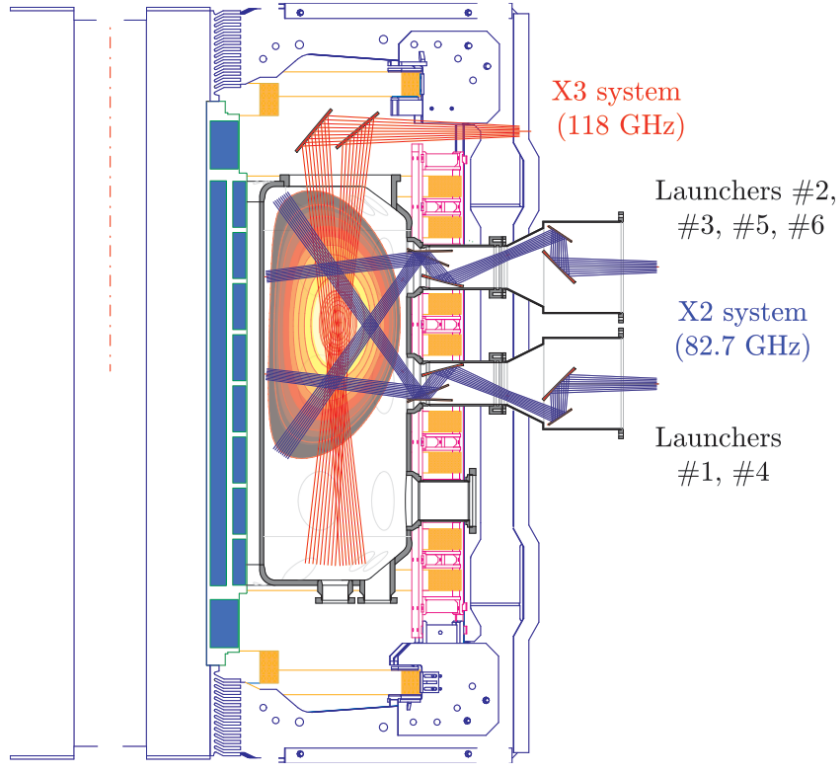
Figure 3.3: Illustration of the TCV poloidal cross section including ECRH/ECCD ports

discharges, allowing for the variation of the toroidal direction of the injected beam within the plasma. On the other hand, the toroidal angle, φ_L, can only be adjusted between different plasma discharges.

3.2. The TCV Vertical ECE

In this section, the TCV VECE system is outlined following the work of [10]. The description of the radiometer system for the VECE is provided in section 3.2.1. Section 3.2.2 is devoted to outlining the optical configuration of the antenna which generates a vertical line of sight with finite horizontal dimensions. The vertical LOS terminates on a viewing dump [84] (section 3.2.3) to prevent background radiation pollution as recommended from previous studies on Alcator C [60], PLT [63] and DIII-D [59].In section 3.2.4, the plasma conditions necessary for Vertical ECE measurements with the diagnostic's available components are envisioned, resulting in an operational window for plasma operations that can ensure the measurement of non-thermal emission from an isolated vertical region of the plasma, free from harmonic overlap. Finally, in section 3.2.5, the estimation of the energies and energy resolution that can be observed by the system is presented.

3.2.1. The Heterodyne Radiometers

The heterodyne radiometers provide a high temporal and spectral resolution and good sensitivity in a moderate frequency band. The frequency range for ECE measurements is contingent upon the particular application and the strength of the magnetic field, which determines the fundamental cyclotron frequency (f_{ECE} GHz ≈ 28B"). In a low magnetic field machine such as TCV (where $0.9\,\text{T} < B_0 < 1.54\,\text{T}$), ECE measurements have been performed in the past with frequencies up to around $110\,\text{GHz}$. Heterodyne radiometers have proven to be effective in detecting ECE in previous experiments on TCV, either for the High Field Side ECE [12] or the Low Field Side ECE [61]. Given their successful implementation in the past, a detection system incorporating heterodyne radiometers was chosen for Vertical ECE measurements in order to investigate non-thermal ECE within the low harmonic region of the spectrum.

The Vertical ECE diagnostic on TCV is equipped with a set of four heterodyne radiometers. These radiometers consist of 42 channels, which are connected to a high-performance acquisition card, the *ACQ42ELF* from *D-TACQ Solutions Ltd*, for digitalization of data. One of the radiometers, with 24 channels, was developed by A. Tema Biwolè [7] and covers a frequency range of 78-114GHz. The other three radiometers, each with 6 channels, were received from *Forschungszentrum Julich GmbH*. One of these radiometers can switch between two LO frequencies to cover the range 89-104 GHz or 133-148 GHz, while the others cover the frequencies 104-114 GHz and 125-130 GHz. A sketch of the overall frequency coverage is summarized in figure 3.4 which shows also an overlap of frequencies, allowing simultaneous measurements of the same frequencies with different radiometers (e.g for X-mode and O-mode separation).
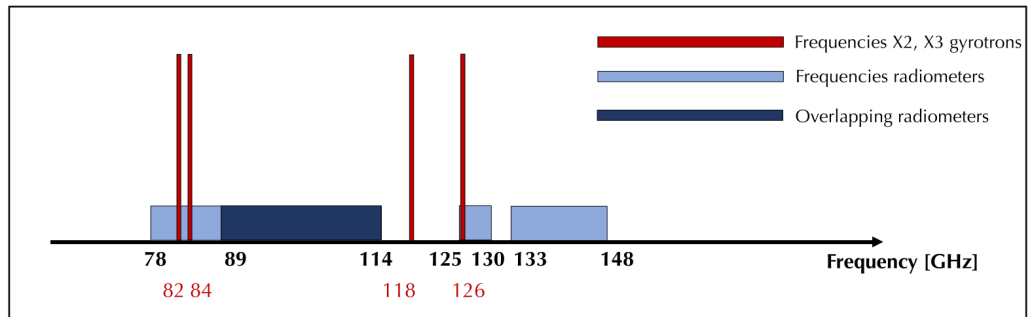
Figure 3.4: Frquency coverage of the TCV ECRH-ECCD system and of the heterodyne radiometers

The time resolution allowed by the radiometers is sufficient for the VECE measurements. The minimum acquisition time of $10\,\mu\text{s}$ is shorter than the typical acceleration time for electrons in TCV (Δt ms to gain a kinetic energy of $511\,\text{keV}$

Frequecy Band Peak Power

A very important feature of each radiometer channel is that, around the central frequency exists also a frequency band with a finite extent. In fact, it has been demonstrated that the radial extent of the channel bandwidth can be calculated as

$$\Delta R = R_0 \frac{\delta f}{f}, \tag{3.1}$$

which for a frequency of 100 GHz is ~ 0.67 com, which is less than the ECE emission layer ~ 2 cm.

Each radiometer channel exhibits a parabolic intensity profile, as illustrated in figure 3.5. If a single pass emission signal[1] reaches its maximum value, it is likely that the highest
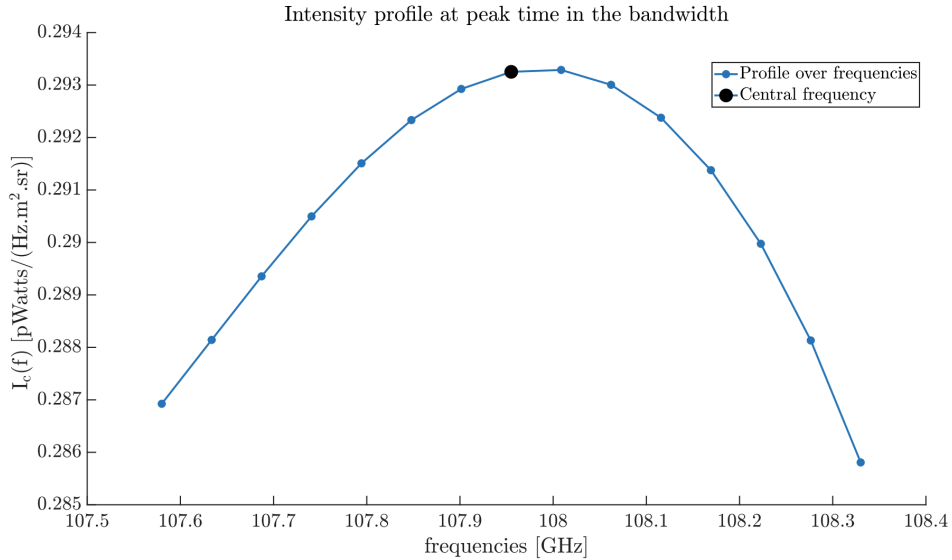
Figure 3.5: SPECE modelled intensity in the bandwidth.

point of the emission layer in the plasma corresponds with the central frequency of the bandwidth. To calculate the power of the bandwidth, one must integrate the spectral intensity over the bandwidth frequencies, solid angle Ω_S, and effective antenna area A, using the formula

$$P_{BW} = \int I(f) \mathrm{d}f \mathrm{d}A \mathrm{d}\Omega_S. \tag{3.2}$$

By making the assumption that $\mathrm{d}A\mathrm{d}\Omega_S \simeq \lambda^2 = 1/f^2$, the formula for the power bandwidth simplyfies to

$$P_{BW} \approx \int 2\pi c^2 \int \frac{I(f)}{f^2} \mathrm{d}f. \tag{3.3}$$

---

[1]Without taking into account any reflection from the tokamak walls.

3.2.2.   The VECE Antenna

The design of the VECE antenna incorporates an optical configuration that aims to generate a LOS within the tokamak while maintaining minimal radial extent. The implementation of this design features a top port with a diameter of 20 cm, upon which an ellipsoidal mirror with a focal length of approximately 61 cm is securely attached. The top port aperture is located at a height of 163.4 cm from the machine floor, and the center of the mirror is situated approximately 101 cm above the mid-plane of the vessel.

The plasma radiation, after passing through the focusing mirror, is gathered by an oversized corrugated waveguide with a diameter of 63.5 mm. The waveguide aperture is situated approximately 72 cm from the center of the mirror and serves as a means of transporting the plasma radiation to a quasi-optical telescope. The telescope, designed by Thomas Keating, is equipped with several components to facilitate the detection of the plasma radiation. These components include a wire grid polarizer, broadband scalar horns, and focusing mirrors. The wire grid polarizer separates the incoming beam into two polarizations, which are then each collected by a horn and fed into the transmission lines for detection. The antenna is designed to center the beam at the major radius $R = 88$ cm of the port, while keeping its radial extent at the mid-plane of the vessel to a minimum. The desired height of the beam waist is approximately 20 cm, at the vessel height Z, to ensure that the beam waist is positioned within the plasma for the majority of experiments conducted on TCV.

The alignment of the antenna system during TCV openings is achieved through the use of a laser that is directed from one of the horns of the quasi-optical telescope. Despite the stability of this alignment being subject to discussion, given factors such as mechanical vibrations of the vessel, the misalignment of the LOS can be monitored during plasma experiments. This allows for the deduction of physics results even in instances where the LOS has deviated from the vertical direction. The size of the beam is characterized by the extent of the $1/e^2$ intensity level within the assumed Gaussian beam model. As per the design, the beam waist has a radius of 3 cm (measured at 100 GHz) and is positioned approximately 20 cmabove the mid-plane of the vessel, at a distance of 81 cm from the mirror and 95 cm from the machine floor. The size of the beam at the mirror and the machine floor are 4 cm and 5 cm, respectively. The ellipsoidal mirror is intended to produce a beam waist of 4 cm at the position of the waveguide, located 72 cm from the mirror in the direction of the detection system. The divergence of the beam in vacuum is calculated to be 2.14°, making the beam well collimated over the 176 cm path from the mirror to the machine floor.
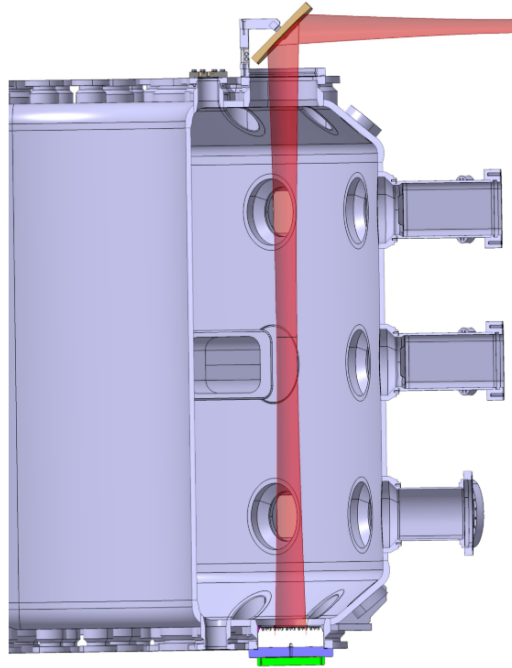
Figure 3.6: Layout of the VECE antenna beam pattern in the TCV vessel
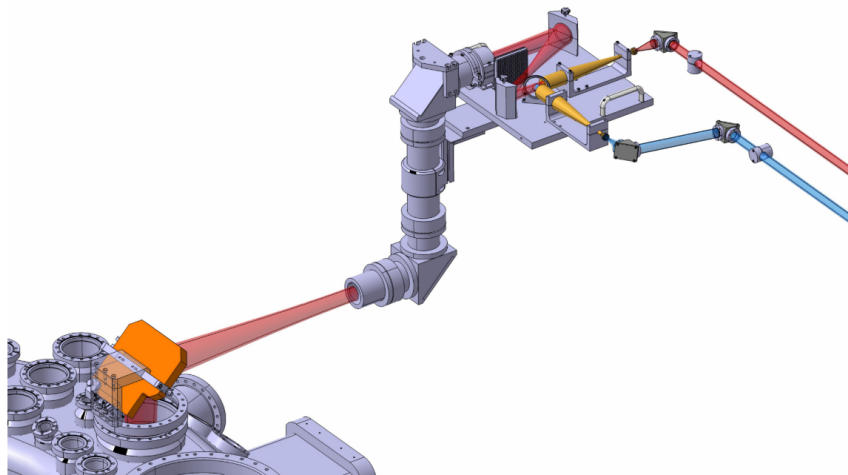
Figure 3.7: Layout of the Vertical ECE antenna beam pattern out of the TCV vessel

For what concerns the polarization tracking, it is important to mention that in the quasi-optical telescope, the wire grid polarizer (depicted in Figure 3.8) is designed to separate incoming radiation into two polarizations, which are assumed to be vertical and horizontal for the X and O mode, respectively, assuming that the polarization has not been altered by reflections on the components of the antenna. The wire grid reflects the polarization with its electric field parallel to its fibers and allows the polarization with its electric field perpendicular to pass through. For Vertical ECE experiments, the direction of

the magnetic field vector is calculated taking into account both its poloidal and toroidal components. The direction of the electric field vectors for the O and X mode polarizations
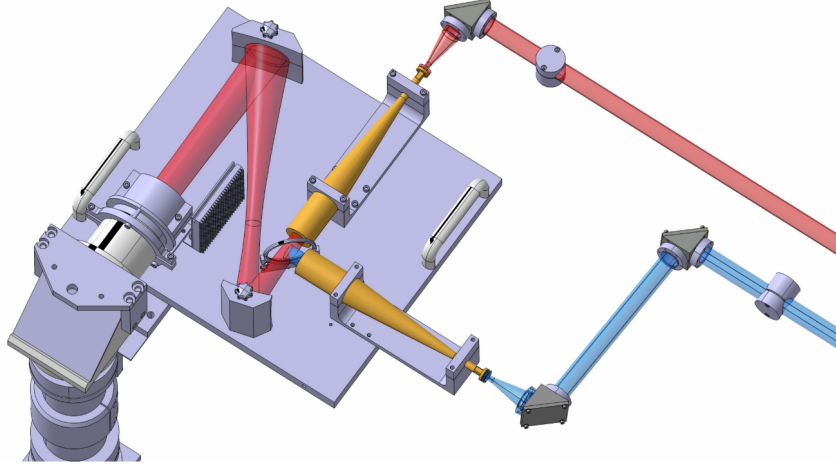
Figure 3.8: Layout of the Vertical ECE antenna beam pattern out of the TCV vessel

is inferred, and the polarizations are separated at the wire grid after being propagated through the mirror using ECPOL [39]. The poloidal component of the magnetic field can shift the ideal polarizations (vertical and horizontal) by a few degrees, making it critical to ensure precise alignment to avoid cross polarization at the grid. This is because the ratio of X to O mode intensities in a typical thermal plasma is on the order of 10^2, and any cross polarization of just 1% would completely obscure the original O mode emission from the plasma.

3.2.3. The Millimeter-Range Viewing Dump

The viewing dump in TCV is made of MACOR, a machinable glass-ceramic material that meets the requirements of high electromagnetic absorption and compatibility with the high temperature and high vacuum environment of the tokamak. MACOR glass-ceramics have been found to have absorption coefficients of $0.08 < \alpha \, (\mathrm{mm}^{-1}) < 0.15$ [1] in the frequency range relevant to the measurements.

Figure 3.9: TCV viewing dump design.

MACOR has a continuous operating temperature of $800\,°\mathrm{C}$, a peak temperature of $1000C$, and is capable of withstanding high heat fluxes. Additionally,it is strong, non-porous, and radiation-resistant, making it an ideal candidate material for the viewing dump [28]. The optimal shapes for the viewing dump in the tokamak are triangular grooves, an array

of horns, or pyramid arrays. The triangular pyramids have dimensions of approximately $10\,\text{mm} \times 10\,\text{mm} \times 11.6\,\text{mm}$, with an angle of 45 degrees between adjacent faces, which leads to 4 reflections for a normally incident ray on the MACOR , thereby increasing the absorption. The size of the pyramids was selected to be approximately $1\ cm$, based on the MACOR's optical thickness. The diameter of the dump is limited by the available space within TCV.

Prior to the installation of the viewing dump on TCV, measurements of the dump properties revealed an average off-axis reflectivity of below $-35\,\text{dB}$ and an on-axis reflectivity of approximately $-30\,\text{dB}$, based on the average value over frequency. In 2019, after years of exposure in the tokamak, the on-axis reflectivity of the dump was measured and found to have an average value of around $-31\,\text{dB}$ in the range of 110 to $170\,\text{GHz}$ and $-35\,\text{dB}$ in the range of 70 to $110\,\text{GHz}$. These results were obtained using an uncalibrated vector network analyzer (VNA) and may overestimate the dump's reflectivity. However, they are fully consistent with the first measurements of the dump's properties taken prior to its installation, indicating that the dump's performance has not been significantly impacted by the plasma. In practical terms, the reflectivity of the dump can be considered to be below $-30\,\text{dB}$, meaning that it reflects approximately 0.1% of incident wave power and absorbs approximately 99.9% of it.

In figure 3.10, a cross-section of TCV, including a representation of the MACOR viewing dump and the VECE antenna, is presented. Radiation reaching the antenna may come from the LFS region that lies outside of the LOS, following the path $1' - 2 - 3$. This type of radiation is unwanted and requires evaluation of the dump's off-axis reflectivity. On the other hand, radiation originating from within the vertical LOS takes the path $1 - 2 - 3$.

3.2.4. The Plasma Conditions for VECE Measurements

After having described the main characteristics of the VECE setup, in this section the set of plasma conditions required for the measurements are detailed. The main aim for the diagnostic is to detect only radiation originating from an isolated vertical volume of plasma. There are two main issues that one wants to avoid when dealing with VECE measurements:

- The EC wave refraction in the plasma affects the direction of the antenna pattern, potentially causing a reduction in the signal received by the detection system. To minimize this effect, the conditions that lead to the minimum amount of refraction in the plasma must be identified and studied;

- It is necessary to ensure that the EC waves within the LOS are not cut off.
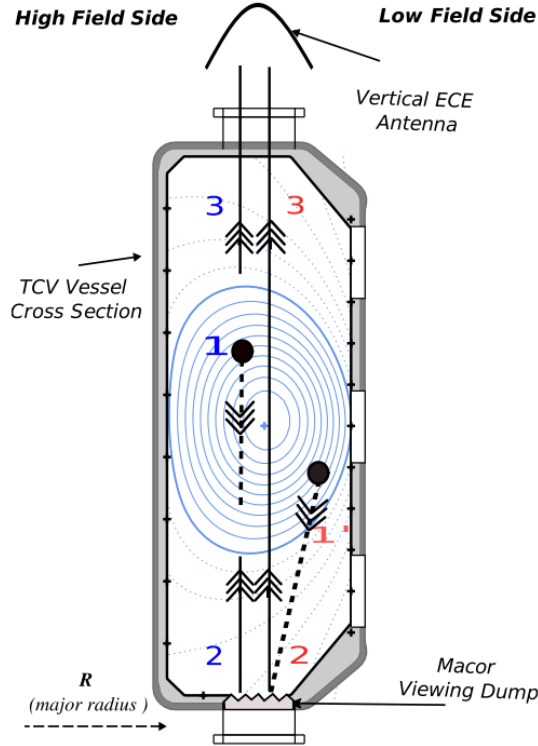
Figure 3.10: Schematic representation of the wanted and unwanted radiation for VECE measurements.

For the latter problem, using the cold plasma wave theory for perpendicular wave propagation [16] [47], it can be found that the cut-off density for the O-mode is a function of the wave frequency only, while the cut-off density for the X-mode is influenced by both the wave frequency and the magnetic field, through the cyclotron frequency [8, 9]. To express the results in the most conservative way possible, the calculation of the minimum cut-off electron densities were performed using a relatively low frequency of 80 GHz and the maximum value of the TCV magnetic field equal to 1.54 T, finding that for the O-mode $n_e \sim 7.94 \times 10^{19} \, \mathrm{m}^{-3}$, while for the X-mode $n_e \sim 3.67 \times 10^{19} \, \mathrm{m}^{-3}$. The cut-off density limit is lower in the extraordinary mode, but the experiments for which one is typically interested in VECE, the densities are usually below this cut-off limit. It is noteworthy that the majority of vertical ECE experiments utilize an $f_{\mathrm{RF}} \sim 80$ GHz X2 ECHR beam to create non-thermal electrons. Therefore, in such experiments, it is necessary to stay below the X-mode cut-off density limit to prevent the gyrotron wave from entering a cut-off state. Many other plasma experiments for vertical ECE require even lower densities.

On the other hand, minimizing the beam refraction in the plasma means determining an optimal range of electron densities that results in the majority of the antenna beam intensity falling within the viewing dump after its interaction with the plasma. The first

step, well detailed in Ref.   [8], was to simulate the beam propagation inside the plasma with the SPECE code [40] that is able to accurately mimic the VECE antenna pattern, but neglecting any diffraction. It has been shown that at high frequencies near 150 GHz, the majority of the beam intensity falls within the viewing dump up to a density of $3.7 \times 10^{-19}\,\mathrm{m}^{-3}$. This density limit is practical for the operation of the Vertical ECE diagnostic in most plasma conditions. However, at low frequencies, the situation is not practical due to the refraction constraints. For this case it is demonstrated that the maximum density of $1.2 \times 10^{-19}\,\mathrm{m}^{-3}$, half of the beam intensity at 80 GHz would miss the dump, setting a stringent maximum density limit for refraction at below $1 \times 10^{-19}\,\mathrm{m}^{-3}$. This severely limits the operational window of the Vertical ECE and requires a solution.

Of the various methods, only one was found to be effective in widening the range of VECE measurements: a variation of the magnetic field. To completely understand how this method works it is necessary to stress the fact that the problem of antenna beam refraction should not be considered separately from the multiple wall reflections of radiation in the tokamak. In fact, when the antenna beam pattern moves away from the viewing dump, there is a risk of contamination of non-thermal emission by background radiation from multiple wall reflections. In this scenario, the measured radiation is a mixture of both the background radiation and non-thermal radiation, making it challenging to separate the two. Although reflection models exist and are widely used by various ECE synthetic diagnostics, in the case of a vertical LOS, these models are inefficient because they are unable to model the complex geometry of TCV tiles in sufficient detail, and they do not take into account the diffraction effects between the tiles' aperture and the change of the EC wave polarization at each reflection.

Methods to minimize the background radiation

The background radiation can only come from specific radial locations, referred to as cold resonances of the contributing harmonics. The radial location of the cold resonance $R_{n,\mathrm{cold}}$ of a given harmonic n and ECE frequency, depends exclusively on the magnetic field B_0 within the machine as

$$R_{\mathrm{n,cold}} = \frac{neB_0R_0}{2\pi m_e f_{\mathrm{n,ece}}}, \tag{3.4}$$

where $R_0 = 0.88\,\mathrm{m}$ is the TCV major radius. According to theory [8–10], only two consecutive harmonics can contribute to the background radiation on TCV. Given the magnetic fields and frequency range on TCV, the cold resonance of the first harmonic cannot be located within the vessel. The background radiation is instead primarily caused by the higher harmonics, which are optically thick for extraordinary polarization. This

means that the background radiation that can be measured by the refracted antenna beam on TCV originates as X-mode emission from a specific location that is determined by the magnetic field. In figure 3.11 the radial location of the harmonics contributing to the background radiation is shown for selected frequencies. The emission layers, which are not shown for simplicity, are located at the high field side of each vertical line representing the major radius of the cold resonances. A schematic LOS is also drawn to indicate the vertical region from which direct emission originates. In Figure 3.11a, the X2 harmonic, a key contributor to the background radiation, has its cold resonace within the tokamak vessel. In this case, multiple wall reflections of the original X2 emission can contaminate the downshifted third harmonic emission in the $92 - 104\,\mathrm{GHz}$ frequency band if the LOS is refracted out of the dump. In Figure 3.11b, the field is lowered to keep the X2 emission outside the machine in the 92-104 GHz frequency band, resulting in clean operation of the diagnostic with relaxed density constraints and no need for a viewing dump. However, the gyrotrons cannot heat the plasma at the second harmonic at this field value. Figure 3.11c shows a good compromise: the field value allows the gyrotrons to heat the plasma near its center, and the X2 resonance location of the ECH frequency even lies within the LOS. The diagnostic can measure the downshifted fourth harmonic emission from non-thermal electrons in the 133-148 GHz frequency band, again without the need for a viewing dump and with relaxed density constraints related only to wave cut-off [8].
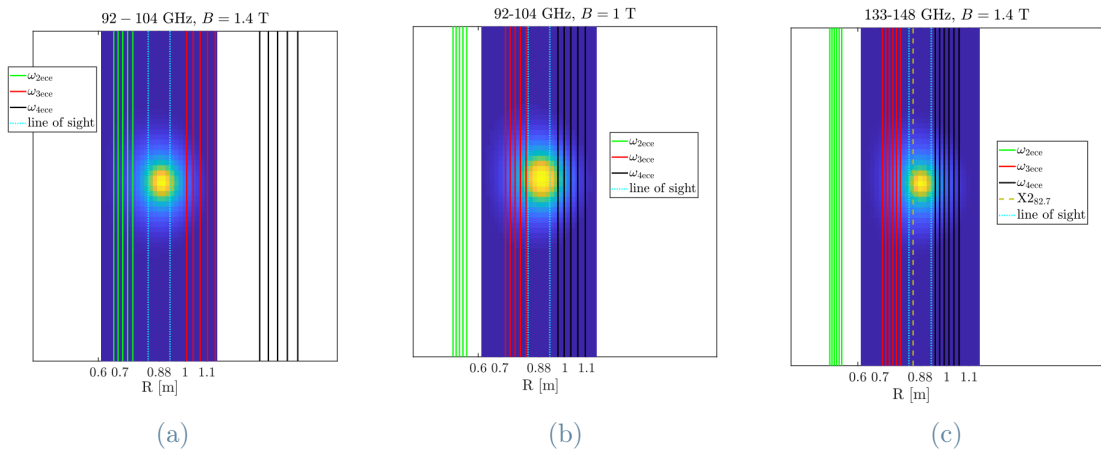
Figure 3.11: Radial location of the harmonics contributing to the background radiation for selected frequencies and magnetic field values.

Since the majority of the ECE radiometers primarily fall between 78 GHz and 114 GHz, careful adjustment of the experimental parameters is necessary to obtain accurate measurements also in this frequency range. As pointend out by A. Tema Biwolè [8] future

radiometer designs for the Vertical ECE on TCV should prioritize the frequency range of 120-170 GHz as it offers the capability of obtaining clean measurements of non-thermal X4/O4 and X3/O3 emission with minimal restrictions on experimental parameters.

3.2.5. The VECE Energy Range and Resolution

In order to assess the electron energy resolution of the VECE, one notes that the relativistic Lorentz factor γ of a resonant electron, in the case where there is no harmonic overlap, is related to the measured frequency and magnetic field via:

$$\gamma \propto \frac{B}{\omega} \propto \frac{B}{f} \tag{3.5}$$

It can be demosntrated [8] that the total uncertainty of the experimentally inferred relativistic factor is the sum of five different contributions:

$$\frac{\delta\gamma}{\gamma} = \frac{\delta\gamma}{\gamma}\Big|_{\text{beam}} + \frac{\delta\gamma}{\gamma}\Big|_{\text{doppler}} + \frac{\delta\gamma}{\gamma}\Big|_{\text{instrument}} + \frac{\delta\gamma}{\gamma}\Big|_{\text{poloidal}} \simeq 13\% \tag{3.6}$$

The "*beam*" factor contributes approximately 7% to the overall uncertainty and reflects the broadening induced by the limited spatial extent of the antenna pattern. The "*Doppler*" factor represents approximately 4% of the uncertainty and encompasses the uncertainties associated with the Doppler effect. The "*instrument*" factor, which amounts to approximately 1%, accounts for the frequency broadening resulting from a 750 MHz bandwidth around each recorded frequency. Lastly, the "*poloidal*" factor, estimated to be around 1%, considers that the magnetic field is not perfectly constant along the verical VECE LOS.

From the expression of the relativistic kinetic energy $E = (\gamma - 1)mc^2$, it can be shown that

$$\frac{\delta E}{E} = \frac{\delta\gamma}{\gamma}\left(1 + \frac{mc^2}{E}\right). \tag{3.7}$$

Equation 3.7 shows that with the uncertainty in gamma fixed, the resolution at higher electron energies is better than at lower.
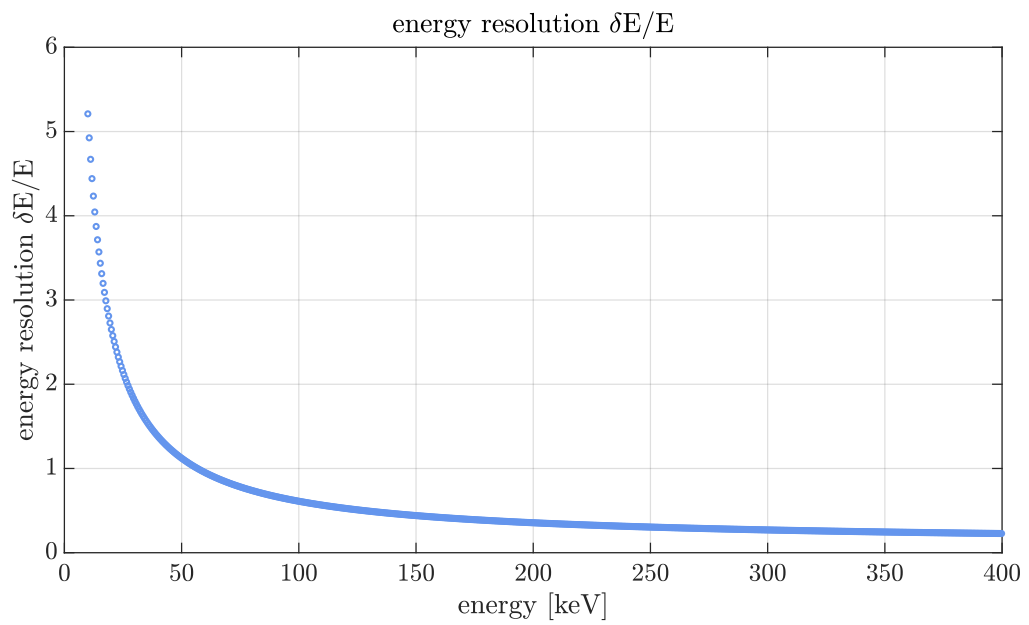
Figure 3.12: Energy resolution of the Vertical ECE diagnostic calculated with a constant $\delta\gamma/\gamma \approx 10\%$ [8].

4 | ECE Synthetic Diagnostic: the YODA code

In this chapter a new ECE synthetic diagnostic, the YODA code and its integration in the STARWARS suite, is presented. The input parameters for YODA are obtained from the C3PO raytracing code [74], which is described in section 4.1, and from the bounce-averaged Fokker-Planck code LUKE (presented in chapter 4.2) which calculates the electron distribution function for different plasma scenarios. The numerical implementation of YODA, along with its validation for thermal plasmas through comparison with the SPECE code [40], is described in section 4.3. The scheme represented in figure 4.1 shows how YODA is embedded in the LUKE-C3PO environment.
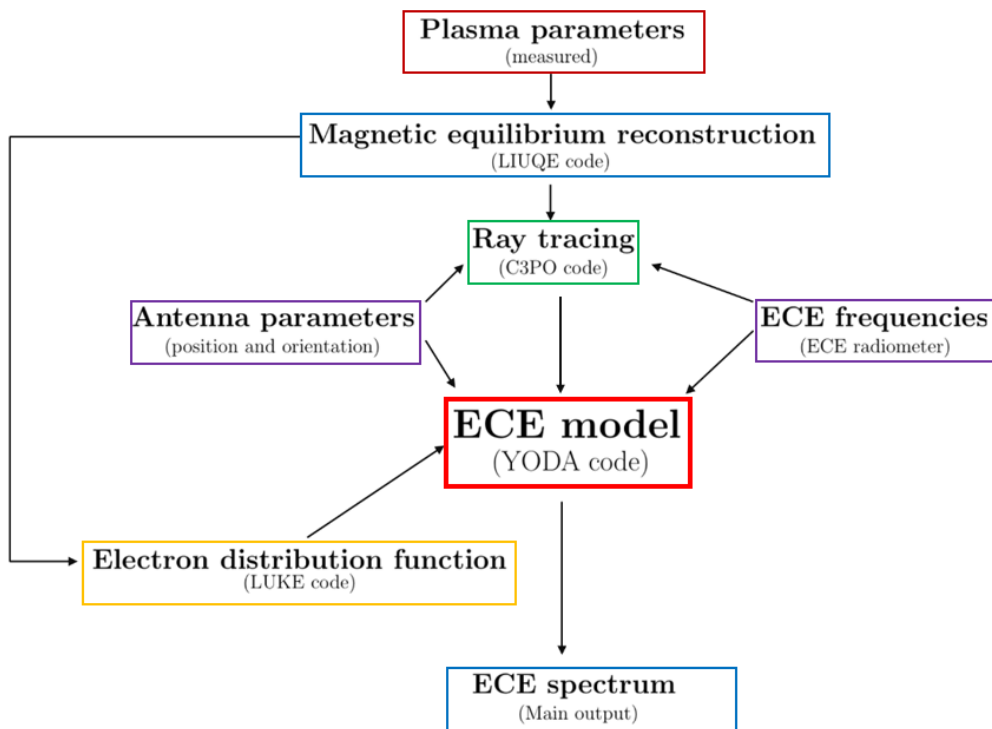
Figure 4.1: Schematic representation of the YODA role in the LUKE-C3PO environment

Before entering into the merit of the complex modelling chain developed to simulate the ECE spectrum, it is worth to clarify the used coordinate system in both the configuration space and in the momentum space.

Momentum Space

Two different momentum space coordinates are considered:

- The cylindrical coordinate system $(p_\parallel, p_\perp, \varphi)$, where $p_\parallel$ and $p_\perp$ are respectively the parallel and the perpendicular components (with respect to the magnetic field lines) of the momentum normalized to the thermal one, while φ is the gyro-angle. This system is the natural system for the wave-particle interaction, in fact YODA is based mostly on these coordinates.

- The spherical coordinate system (p, ξ, φ), where $p = |\boldsymbol{p}|$ is the magnitude of the momenutm, while $\xi = \boldsymbol{p} \cdot \boldsymbol{B}/(pB)$ is the cosine of the pitch angle. This coordinate system is a natural coordinate system for collisions, therefore it is the primary system used in LUKE for an accurate description of collisions.

A formal definition of all these coordinate systems can be found in [30], and they are illustrated in figure 4.2.

These two coordinate systems can be exchanged simply applying the relations $p_\parallel = p\xi$ and $p_\perp = p\sqrt{1 - \xi^2}$.

Configuration Space

To take advantage of the axisymmetry and flux-surface magnetic configuration of tokamaks, specific coordinates must be used in the configuration space. From all the different coordinate systems, it is relevant to define the most important two for this thesis.

The first is the toroidal coordinate system (R, Z, ϕ), where R is the distance from the axis of the tokamak and Z the distance along this axis. This coordinate system is defined by local orthogonal basis vectors $(\hat{R}, \hat{Z}, \hat{\phi})$. It is depicted in figure 4.3.

The second is the flux coordinate system (ψ, θ, φ), where ψ is the poloidal magnetic flux, θ is the poloidal angle and φ the toroidal angle. In the approximations used in LUKE, the motion of particles can be accurately described by their movement along magnetic field lines. Consequently, particles move along surfaces that have a constant value of ψ, which represents a constant of motion. In the poloidal plane, the position of a particle on the flux surface can be characterized by the poloidal angle θ, which is defined as the
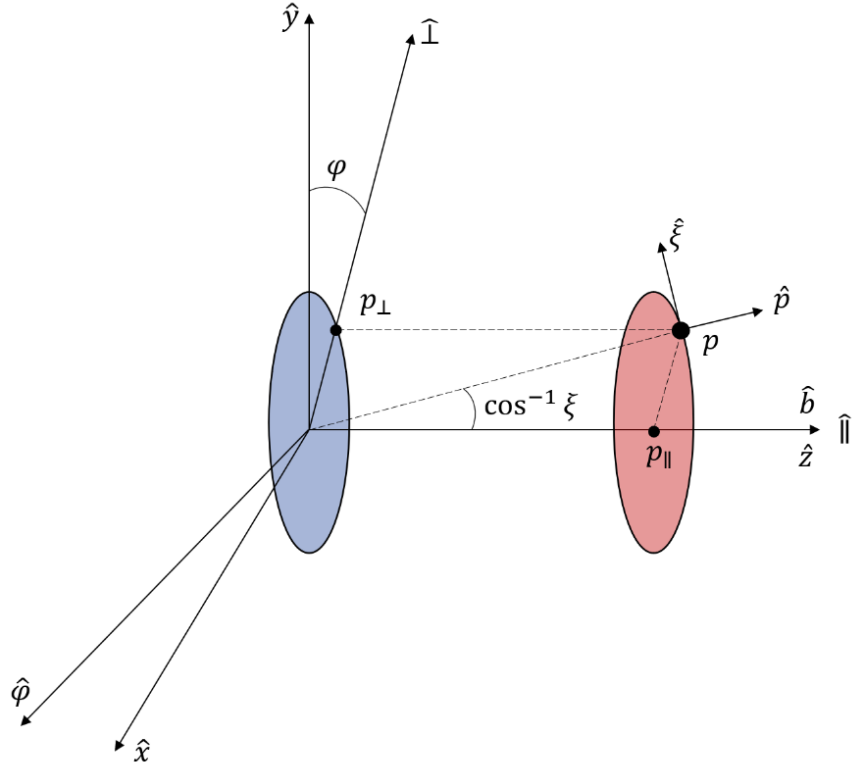
Figure 4.2: Momentum space coordinate systems $(p_\parallel, p_\perp, \varphi)$ and (p, ξ, φ).

angle between the particle position and the outer midplane, with the origin located at the magnetic axis. On the other hand, the toroidal angle refers to the angle between the particle's position and some reference position in the tokamak, in the toroidal direction. Figure 4.4 illustrates the definition of the configuration space coordinates.

4.1. Ray-tracing: the C3PO code

In this thesis, the C3PO [74] code is employed as a raytracing code. It serves two purposes:

1. The mimicking of the VECE antenna pattern;

2. The simulation of the wave-particle interaction due to ECH.

The latter use of C3PO is a routine application on TCV, whereas its utilization for mimicking the antenna pattern of an ECE diagnostic has never been done before this study. Before entering into the details of the VECE antenna pattern mimicking, it is valuable to provide an overview of C3PO.

C3PO is made to calculate power and power deposition resulting from radio frequency
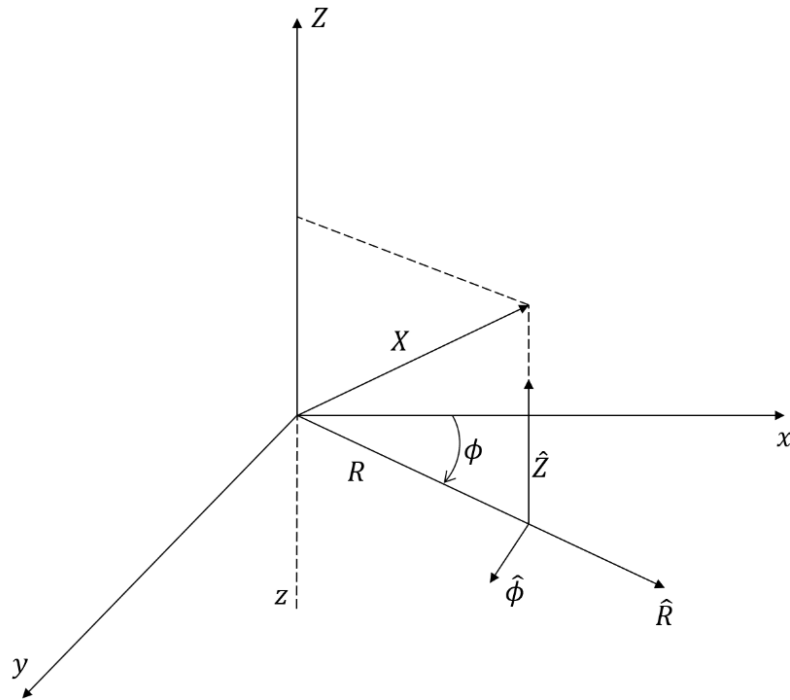
Figure 4.3: Tokamak toroidal coordinate system (R, Z, ϕ) in the configuration space.
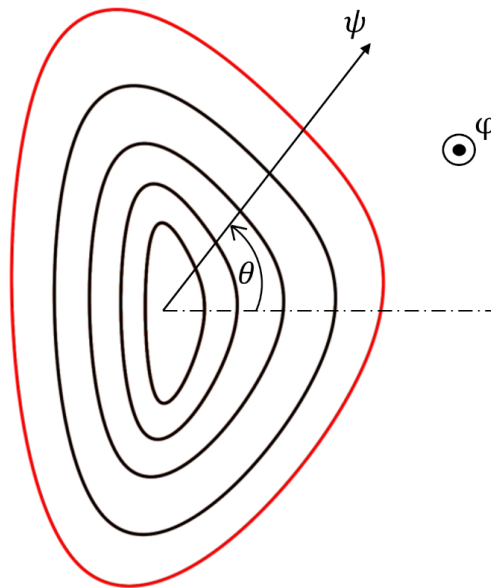
Figure 4.4: Illustration of the 3D configuration space coordinate system used by LUKE - C3PO - YODA in a tokamak magnetic geometry. Any point in the plasma is parameterised by the poloidal magnetic flux ψ, the poloidal angle θ and the toroidal angle φ (directed out of the paper) [53].

(RF) waves in plasmas[1], starting from a magnetic equilibrium reconstruction, an electron density profile and an electron temperature profile given as input[2].
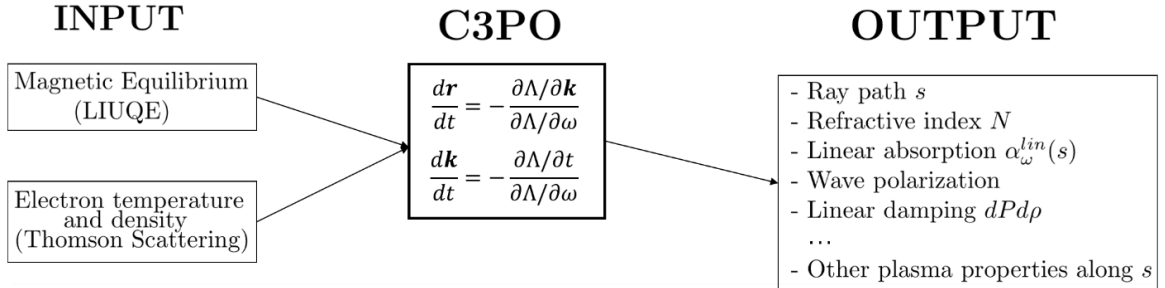
Figure 4.5: Schematic representation of the C3PO input and output

The ray-tracing approach is based on a *reciprocity theorem* for the calculation of the received ECE power. The reciprocal problem is related to the original problem by launching a wave from the antenna, allowing it to propagate into the reciprocal plasma, and being absorbed by the electron cyclotron resonance. To do that, it is mandatory to obtain a comprehensive understanding of the wave characteristics within the propagating medium. In plasmas that are quasi-stationary, wherein the scale of equilibrium changes is much larger than the wavelength, it is feasible to compute the propagation of the waves from antenna or mirror conditions as well as the equilibrium properties through the use of ray-tracing techniques. This methodology has been extensively employed in the analysis of lower-hybrid (LH) and electron cyclotron (EC) wave propagation [11, 14, 56, 75]. In axisymmetric toroidal plasmas, many ray-tracing codes [55, 66, 81] adopt the toroidal coordinate system (R, Z, φ), due to its simplicity in the implementation of differential equations resulting from its orthogonality.

The utilization of magnetic flux coordinates (ψ, θ, φ) in the C3PO code is a noteworthy advantage despite its more complex metrics [74] (an illustration of this coordinate system is depicted in figure 4.4). This is due to three benefits:

- Only 1D interpolations are necessary for flux functions, such as the equilibrium density and temperature;

- The poloidal direction described by the angular coordinate θ leverages Fourier series for efficient and precise interpolations and the computation of derivatives of any order;

---

[1] YODA does not use C3PO to calculate the RF power absorbed, but to mimick the ECE antenna pattern.

[2] In the framework of this thesis the magnetic equilibrium is reconstructed by the LIUQE code and the temperature/density profiles are provided by the Thomson scattering.

- This system is the same used in the Fokker-Planck solver LUKE [30], allowing a better coupling between the two codes.

This curvilinear coordinate system associated with an axisymmetric toroidal MHD equilibrium with nested magnetic flux surfaces, primarily focuses on studying the propagation of any RF wave in the volume enclosed by the magnetic separatrix. The C3PO code has been created to support arbitrary wave frequencies, including those in the lower hybrid and electron cyclotron frequency ranges, as long as the WKB approximation is still applicable. The code structure is flexible and enables the selection of various dielectric tensor types, including *cold* plasma, *warm* plasma [15], and kinetic plasma in the non-relativistic, weakly relativistic, or fully relativistic regime. In addition to ray tracing, the software determines several wave properties relevant to heating and current drive calculations, such as polarization, energy flow, and linear absorption. C3PO calculations are based on a 6th order Runge-Kutta scheme and it employs a spline-Fourier expansion to interpolate the magnetic equilibria, yielding efficient and precise calculations. The code is implemented as a C language mexfile and it was extensively benchmarked for different wave types, comparing its results to both established codes and analytical models. The outcomes of the benchmarks demonstrate the code's accuracy and reliability [74]. For a detailed description and use of C3PO it is possible to refer to [74] and [31].

4.1.1.   Mimicking the VECE Antenna Pattern

As already outlined, the main purpose of the C3PO code in YODA is to mimick the ECE antenna pattern in its vertical configuration described in section 3.2.2.

To simulate this Gaussian antenna pattern, a vertical synthetic EC wave launcher is constructed using the C3PO-MATLAB interface, specifying all the launching parameters according to the real antenna parameters:

- $R_L = 0.88$ is the last mirror radial position of the center [m];

- $Z_L = 0.99$ is the last mirror vertical position of the center$[m]$;

- $\varphi_L = 0$ is the last mirror toroidal position of the center $[rad]$;

- $\alpha_L = \pi$ is the launching direction from the last mirror center (horizontal angle with respect to the R axis);

- $\beta_L = \pi$ is the launching direction from the last mirror center (vertical angle with respect to Z axis);

- ω_{RF} is the launched angular frequency to be simulated $[rad/s]$;

- $P_L = 10^6$ is the launched power $[W]$;

- $w_0 = 0.03$ is the beam waist $[m]$;

- $z_L = 0.2$ is the distance from the last mirror center to the waist $[m]$;

- $mmode$ is the selected polarization (1 for the X-mode and 0 for the O-mode).

In this way, the rays are launched from the antenna position and they are propagated through the plasma until the last closed flux surface (LCFS). The ray trajectories in the vacuum before and after the separatrix are modeled as straight lines. Only a single passage of the rays through the plasma is necessary, since YODA does not model the reflection from the tokamak inner walls. It is also important to stress the fact that, since the ray-tracing is performed only for points within the last closed flux surface (LCFS), the wave polarization at the plasma boundary outlet is assumed to be conserved until the antenna.

The EC emission layer width is a critical factor that affects ray propagation in antenna patterns. This factor becomes particularly significant in top-launched configurations, where some rays may miss the emission layer due to its finite spatial width, making it necessary to increase the number and optimize the disposition of rays in the pattern. It is interesting to note that the emission layer width is not a significant issue in horizontal LOS configurations, as a single ray traveling horizontally toward the emission layer is unlikely to miss it. However, when launching rays from the top, the situation becomes more complicated. Some rays may mimic the antenna pattern but miss the emission layer, resulting in an inaccurate representation of the true intensity distribution. To address this, the number of rays must be optimized to ensure the most accurate representation of the antenna pattern. The

Figure 4.6: Poloidal view of a C3PO simulation of the *VECE* antenna pattern (#73003 t = 1.9s X-mode).

C3PO code is capable of using an arbitrary number of rays n_{rays} inside the antenna beam as

$$n_{rays} = n_{angular}\, n_{radial}$$

where $n_{angular}$ is the number of rays in the same angular position, while n_{radial} is the
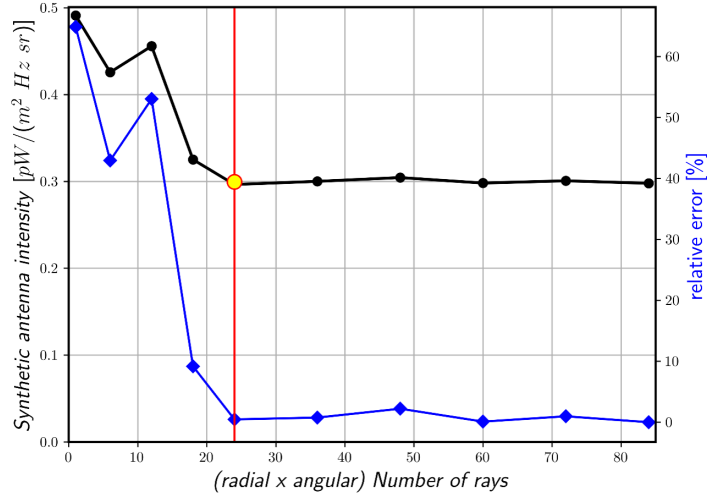
Figure 4.7: Convergence study of the minimum number of rays needed to model the antenna pattern: shot #73003 $t = 1.9$s (X-mode)

number of rays in the same radial position. Every ray of the pattern carries the same power,

therefore the gaussian shape of the antenna pattern is obtained only by an appropriate placement of the rays in the pattern[3] and, the overall synthetic intensity at the antenna $I_\omega(s_{ant})$ calculated by YODA can be simply expressed as

$$I_\omega(s_{ant}) = \frac{\sum_{n=1}^{n_{rays}} I_\omega^{(n)}(s_{ant})}{n_{rays}}, \tag{4.1}$$

where $I_\omega^{(n)}(s_{ant})$ is the synthetic intensity calculated for the nth ray in the pattern. In order to determine the minimum number of rays required to ensure adequate coverage of the entire antenna pattern, it is necessary to calculate the synthetic antenna intensity with YODA using various patterns made by different number of rays, and perform a convergence study with respect to the antenna intensity $I_\omega(s_{ant})$.

In figure 4.7 it is shown that the minimum number of rays required in the pattern is 24, distributed in a 6×4 configuration (4 concentric circles with on each 6 rays not equally spaced) which is shown in figure 4.8. Another aspect of the construction of the VECE synthetic antenna pattern concerns the fact that, during a plasma disharge, the line of sight can depart from its perfect vertical orientation due to mechanical vibrations. For TCV, usually, the LOS shifts towards the HFS of the machine, as obeserved in [8]. In

---

[3]It means that, since the rays are not weighted directly in the carried power, their position in the pattern is calculated by C3PO in order to mimic a Gaussian beam pattern.

(a)   (b)
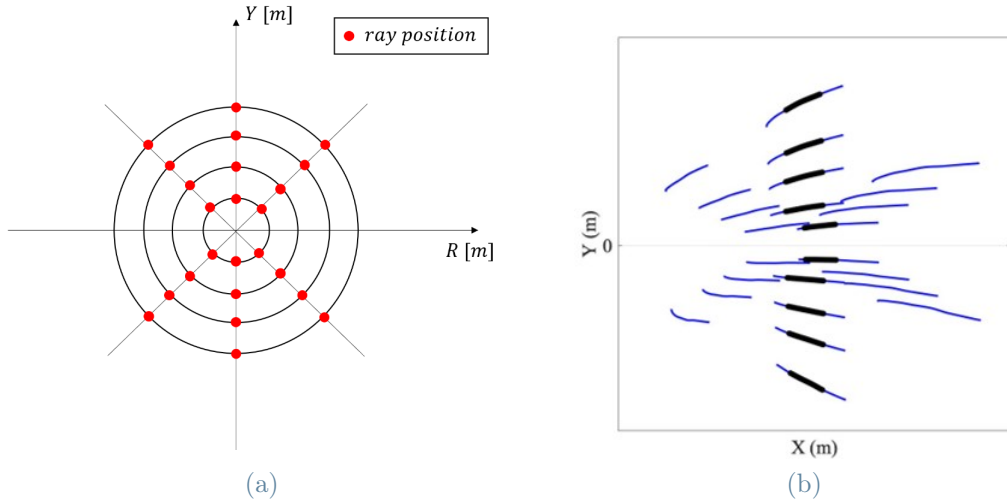
Figure 4.8: Toroidal zoom view of the antenna pattern: (a) Schematic representation of the VECE antenna pattern - (b) C3PO simulation of the VECE antenna pattern (#73003 $t = 1.9s$).

order to take into account this, it is possible to use an optimization process to match the correct β angle, in the C3PO launcher.

4.2. Fokker-Planck Equation Modelling: the LUKE code

The solution of the Fokker-Planck equation (2.79) describes the evolution of the electron distribution function in the momentum space. Initially, a Maxwellian equilibrium distribution undergoes diffusion in momentum space, resulting in an asymmetric distribution due to the influence of the radio frequnecy wave field, Coulomb collisions, and external electric fields. This is the fundamental cause of the presence of non-inductive plasma current. Solving the Fokker-Planck equation represents the primary modeling technique for ECCD plasmas in this thesis and the main modelling tool is LUKE [30].

The LUKE code is a fully relativistic 3D bounce-averaged Fokker-Planck solver and it is strongly coupled with the ray-tracing code C3PO. LUKE can process any numerical equilibrium data from a TCV shot, which is obtained from the LIUQE magnetic equilibrium reconstruction code [70]. Additionally, it can take in other parameters such as the EC injected power, mirror angles, wave polarization, as well as electron temperature, and effective charge (Z_{eff}) data acquired from the Thomson scattering, soft X-ray, and charge exchange diagnostics. LUKE takes also into account the impact of an applied electric field, specifically the inductive loop voltage (VLOOP). The code is formulated in

a numerically conservative formalism, ensuring the conservation of the electron density, thereby facilitating an accurate treatment of the current drive problem.

In the next sections, starting from the time scales involved in the description of the electron dynamics, an introduction on the drift kinetic equation is provided along with a description of the anomalous radial transport operator and the induction equation implemented in LUKE.

4.2.1. Time Scales and Length Scales

The Fokker-Planck equation is solved by LUKE assuming a ordering for various time scales such that a magnetic field that is strong enough to ensure that the electron gyro-motion period (Ω^{-1}) is significantly shorter than both the collision time τ_c and bounce times τ_b. The *collision time* is a measure of the typical timescale over which a particle undergoes deflection from its unperturbed trajectory by a *significant* deflection angle. This deflection occurs through the cumulative effect of numerous small deflections. A mathematical expression for this characteristic time is given by [30]

$$\tau_c = \frac{4\varepsilon_0 m^2 v_T^3}{q^4 \, n \, \ln \Lambda}, \tag{4.2}$$

where v_T is the thermal velocity and n is the plasma density. On the other hand, the *bounce time* is defined as the time it takes for the particle to complete a full turn in the poloidal angle (for trapped and passing particles respectively) through the integration of the particle's (gyro-center) orbit

$$\tau_b = \oint \frac{\mathrm{d}l_B}{v_\parallel}, \tag{4.3}$$

where l_B is the arc-lenght along the magnetic field line.

It is assumed that electrons remain on a particular flux-surface for a duration that is considerably longer than the poloidal electron bounce time. This assumption is equivalent to expressing the condition as $\tau_b \ll \tau_d \approx \tau_f$, where τ_f is the typical timescale for fast electron radial transport and τ_d denotes the time for an electron to drift radially across the plasma for a distance of the order of the plasma minor radius r_p, owing to the magnetic field gradient and curvature

$$\tau_d \simeq \frac{2\pi \, R_p \, r_p}{v_T \, \rho_L} \frac{B}{B_\phi}. \tag{4.4}$$

where R_p is the plasma major radius, ρ_L is the Larmor radius and B_ϕ is the toroidal component of the magnetic field. In addition, it is assumed that trapped electrons undergo multiple bounce motions probably covered by the ordering above. The aforementioned

assumptions can be expressed using the following time scales sequence:

$$\Omega_c^{-1} \ll \tau_b \ll \tau_c \ll \tau_d \approx \tau_f \ll \tau_{eq} \qquad (4.5)$$

where the equilibrium evolution time scale is represented by the last factor τ_{eq}.

For what concerns the length scales, the main assumption is the zero orbit width (ZOW) limit in which the Larmor radius and the orbit width resulting from magnetic drifts are considerably smaller than the length scale over which the magnetic field exhibits significant variations

$$\rho_L, \rho_{drift} \ll \frac{B}{|\nabla B|} \qquad (4.6)$$

where ρ_{drift} refers to the gyro-averaged distance deviation from the flux surface.

4.2.2. The Bounce-averaged Fokker-Planck equation

Various orderings have been used in the derivation of the bounce-averaged Fokker-Planck equation to reduce the dimensionality of the problem. In fact, the electron distribution function in the guiding-center approximation exhibits a 2D structure in both configuration space (ψ, θ) and momentum space (p, ξ), thus forming a 4D space.

However, when the collisionality is low (i.e. the ratio of the detrapping frequency to the bounce frequency is very low), the fast bounce motion allows the 3D Fokker-Planck equation to be derived via an additional averaging process [26]. Consequently, the solution of the bounce-averaged Fokker-Planck equation for the electron distribution function can be expressed as a function of ψ, p and ξ.

In the small gyro-radius limit [30, 45], the Fokker-Planck equation (2.79) can be reduced to the so called *drift kinetic equation* for the electron distribution function f_e as

$$\frac{\partial f_e}{\partial t} + \{f_e, H_e\} = \sum_s \mathcal{C}(f_e, f_s) + \sum_n \mathcal{Q}_{RF,n}(f_e) + \mathcal{E}(f_e) + \mathcal{S}(f_e), \qquad (4.7)$$

where H_e is the Hamiltonian for electrons and $\{...\}$ the Poisson brakets. The right hand side of equation (4.7) accounts for physical phenomena affecting the electron distribution function f_e. The *collision* operator $\mathcal{C}(f_e, f_s)$ accounts for the collisions between the electrons and the other species s, the ohmic electirc field is accounted for by the *Ohmic* operator $\mathcal{E}(f_e)$, the quasilinear (QL) *diffusive* operator $\mathcal{Q}_{RF,n}(f_e)$ describes the EC plasma-wave interaction during the Electron Cyclotron Heating (ECH) phase, while $\mathcal{S}(f_e)$ is an *ad-hoc transport* operator. In this thesis, LUKE also solves the Ampère-Faraday equation

commonly known as the *induction* equation [29].

In the following, some details on the quasilinear operator and on the induction equation used in LUKE are described.

The Quasilinear Diffusion Operator and the Ad-Hoc Radial Transport Operator

In the configuration space $(v_\perp, v_\parallel, \rho)$ the QL diffusive operator can be written as

$$\mathcal{Q}_{RF,n} = \nabla \cdot (\mathbb{D}_{EC,n} \cdot \nabla f_e), \tag{4.8}$$

where the tensor

$$\mathbb{D}_{EC,n} = D_{EC,n}(v_\perp, v_\parallel, \rho) \begin{pmatrix} s^{\perp\perp} & s^{\perp\parallel} & 0 \\ s^{\parallel\perp} & s^{\parallel\parallel} & 0 \\ 0 & 0 & 0 \end{pmatrix}. \tag{4.9}$$

The factor $D_{EC,n}$ in the equation (4.9) is the *diffusion coefficient* and $s^{\perp\perp}$, $s^{\perp\parallel}$, $s^{\parallel\perp}$ and $s^{\parallel\parallel}$ are the phase space diffusion tensor elements [26]. The wave propagation is solved by the ray-tracing software C3PO , which is directly coupled to LUKE, allowing three-dimensional configurations of the electromagnetic waves.

Since in LUKE, the drift kinetic equation (4.7) is bounce averaged and linearized, the turbulent transport is suppressed by construction [24]. To overcome this issue, it is possible to use an *ad-hoc* transport operator $\mathcal{S}$ in a diffusion-convection approximation

$$\mathcal{S} = \nabla \cdot (\mathbb{D}_r \cdot \nabla f_e - \boldsymbol{F}_r f_e), \tag{4.10}$$

where $\mathbb{D}_r$ is the radial *diffusion coefficient* and $\boldsymbol{F}_r$ describes a pinch effect [26]. In this way, the radial electron transport can be controlled by changing the value of the diffusion coefficient in order to match the experimental plasma current.

The Induction equation

In LUKE, to take into account the electric field response to a varying current density, the induction equation is needed. This equation can be obtained by combining Ampère's and Faraday's laws, respectively:

$$\nabla \times \boldsymbol{B} = \mu_0 \boldsymbol{J} \tag{4.11}$$

$$\nabla \times \boldsymbol{E} = -\frac{\partial \boldsymbol{B}}{\partial t}. \tag{4.12}$$

Taking the curl of equation (4.12) and plugging in equation (4.11), after using the relations $\nabla \times (\nabla \times \boldsymbol{E}) = -\nabla^2 \boldsymbol{E}$ and $\nabla \cdot \boldsymbol{E} = 0$, it is possible to find the expression

$$\nabla^2 \boldsymbol{E} = \mu_0 \frac{\partial \boldsymbol{J}}{\partial t}, \tag{4.13}$$

commonly known as *induction equation*. The electric field **E** results from either a non-zero electrostatic potential Φ or it can be induced by means of a transformer or by a time variation of the plasma current:

$$\boldsymbol{E} = -\nabla \Phi + \frac{\partial \boldsymbol{A}}{\partial t}, \tag{4.14}$$

where $\boldsymbol{A}$ is the magnetic vector potential. The electrostatic potential arises due to transport, vanishing in the toroidal direction. The potential is typically of the order $\sim T_e/e$ [48], which allows one to assume that the induced component of the electric field is purely toroidal for the problems solved by LUKE. Here the assumption is that the electric field variation arises either due to transformer action, or that the plasma current decays sufficiently slowly that $|\Delta \Phi| \gg |\partial \boldsymbol{A}/\partial t|$. As a result, the induction equation reduces to a single partial differential equation

$$\nabla^2 E_\phi = \mu \frac{\partial J_\phi}{\partial t}, \tag{4.15}$$

where the subscript ϕ stands for the toroidal component of the considered physical quantities. By projecting the toroidal electric field on the direction parallel to the magnetic field, it is possible to determine the parallel component of the magnetic field

$$E_\parallel = (\boldsymbol{b} \cdot \hat{\phi}) E_\phi. \tag{4.16}$$

It is also possible to correlate the electric field E_ϕ to the tokamak loop voltage:

$$V_{loop} = \oint E_\phi R \mathrm{d}\phi = 2\pi R E_\phi. \tag{4.17}$$

The loop voltage is measured at the plasma edge, therefore it is possible to find the boundary condition

$$E_\phi(\psi = \psi_a) = \frac{V_{loop,a}}{2\pi R(\psi_a)}. \tag{4.18}$$

LUKE solves an induction equation which is the toroidal projection of the general equation in an axisymetric geometry, in the form

$$\frac{B_0}{\bar{q}(\psi)} \frac{\partial}{\partial \psi} \left(B_0 \, l(\psi) \frac{\partial V_{loop}}{\partial \psi} \right) = 2\pi \mu_0 \frac{\partial \langle J_\phi \rangle}{\partial t}, \tag{4.19}$$

where

$$l(\psi) = \frac{1}{B_0} \int_0^{2\pi} \frac{r|\nabla \psi|}{2\pi \, R} \mathrm{d}\theta, \tag{4.20}$$

$$\bar{q}(\psi) = \int_0^{2\pi} \frac{1}{2\pi \cos \alpha} \frac{r B_0}{|\nabla \psi|} \mathrm{d}\theta. \tag{4.21}$$

The brackets $\langle ... \rangle$ refer to the flux average of a quantity $\Gamma(\psi, \theta)$ as

$$\langle \Gamma \rangle (\psi) = \frac{1}{\bar{q}(\psi)} \int_0^{2\pi} \frac{1}{2\pi \cos \alpha} \frac{r B_0}{\Gamma} (\psi, \theta) \, \mathrm{d}\theta. \tag{4.22}$$

While, to define the rotational angle α, it is necessary to define a local orthonormal basis $\left(\hat{\psi}, \hat{s}, \hat{\phi} \right)$ as

$$\hat{\psi} = \frac{\nabla \psi}{|\nabla \psi|}, \tag{4.23}$$

$$\hat{s} = \hat{\phi} \times \hat{\psi}. \tag{4.24}$$

So that the transformation from the coordinates $\left(\hat{r}, \hat{\theta} \right)$ to $\left(\hat{\psi}, \hat{s} \right)$ is defined through [30]

$$\begin{pmatrix} \hat{\psi} \\ \hat{s} \end{pmatrix} = \begin{pmatrix} \cos \alpha & -\sin \alpha \\ \sin \alpha & \cos \alpha \end{pmatrix} \cdot \begin{pmatrix} \hat{r} \\ \hat{\theta} \end{pmatrix}. \tag{4.25}$$

4.3. ECE Synthetic Diagnostic: the YODA code

The YODA code was developed as part of this thesis. Starting from the input provided by C3PO and LUKE it solves the radiation transport equation for EC waves. In the present version, it is written in Python. YODA distinguishes itself from other ECE synthetic diagnostic codes because it is able to calculate ECE spectra using any arbitrary numerical electron distribution function, making it particularly suited for suprathermal electron studies when used in its vertical antenna configuration to simulate VECE spectra. A general overview of YODA is presented in figure 4.9.
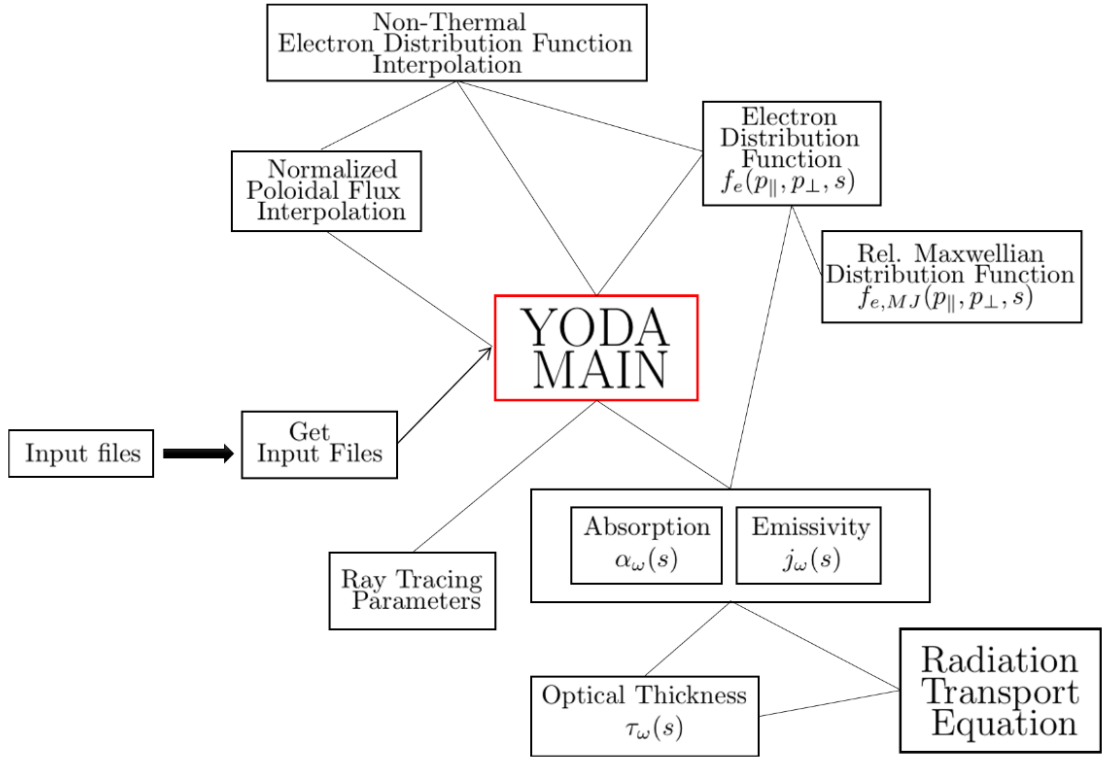
Figure 4.9: Overview of the YODA main classes and functions

4.3.1. Interpolation of ray-tracing parameters

To run a synthetic ECE simulation with YODA, the ray-tracing parameters listed in table 4.1 are needed. These quantities are directly calculated by C3PO and they are local quantities dependent on the ray path s. Since the integrands of the absorption coefficient

Table 4.1: Main reaytracing parameters calculated by C3PO.

Symbol	Parameter
s	Ray path
$N_\parallel(s)$	Refractive index parallel component
$N_\perp(s)$	Refractive index perpendicular component
$T_e(s)$	Electron temperature
$n_e(s)$	Electron density
$B(s)$	Magnetic field
$\boldsymbol{S}_{x,y,z}(s)$	Poynting Flux in cartesian coordinates
$\tilde{\boldsymbol{e}}_{x,y,z}(s)$	Polarization vector in cartesian coordinates

and of the emisivity, respectively in equations (2.58) and (2.59), are functions of the ray position s, all the ray-tracing parameters are interpolated along s using a 1D linear

interpolation scheme provided by the python scipy class *interp1d*.

4.3.2. EC Emission and Absorption

To solve the radiation transport equation, the step that requires the highest computational resources is the calculation of the absorption coefficient (equation (2.58)) and the emissivity (equation (2.59)). In principle, these two integrals are expressed as bi-dimensional integrals in the momentum space $(p_\parallel, p_\perp)$, but exploiting the properties of the Dirac delta it is possible to reduce them to one-dimensional integrals, making calculations computationally less demanding. In the following, the procedure to do this simplification is presented.

One can start by recalling one elementary property of the Dirac delta function:

$$\int_{-\infty}^{\infty} f(x)\delta^{(n)}(x-a)\,\mathrm{d}x = (-1)^n f^{(n)}(a) \tag{4.26}$$

That said, the idea is to exploit the resonance condition (namely equation (2.63)) in order to obtain it in the form $\delta\left(p_\parallel - p_\parallel(p_\perp)\right)$. To do that, one can set the resonance condition equal to zero as

$$1 + p_\perp^2 + p_\parallel^2 = \left(p_\parallel N_\parallel + \frac{n\Omega_{c,0}}{\omega}\right)^2 \tag{4.27}$$

which can be seen as a second order equation in $p_\parallel$. It can be solved finding that

$$p_{\parallel,\pm}(p_\perp) = \frac{N_\parallel \frac{n\Omega_{c,0}}{\omega} \pm \sqrt{N_\parallel^2(1+p_\perp^2) + \frac{n^2\Omega_{c,0}^2}{\omega^2} - p_\perp^2 - 1}}{1 - N_\parallel^2} \tag{4.28}$$

that is an explicit function of $p_\perp$. The equation (4.27) has two roots, therefore another property of the delta function must be taken into account. Let us express the resonance condition in its explicit form, by calling it $g(p_\parallel)$

$$g(p_\parallel) = \sqrt{p_\perp^2 + p_\parallel^2 + 1} - p_\parallel N_\parallel - \frac{n\Omega_{c,0}}{\omega}. \tag{4.29}$$

Therefore, it can be demonstrated that

$$\delta\left(g(p_\parallel)\right) = \frac{1}{\left|g'(p_{\parallel,+})\right|}\delta\left(p_\parallel - p_{\parallel,+}\right) + \frac{1}{\left|g'(p_{\parallel,-})\right|}\delta\left(p_\parallel - p_{\parallel,-}\right) \tag{4.30}$$

where the prime indicates the first derivative

$$g'(p_{\|}) = \frac{p_{\|}}{\gamma} - N_{\|}.$$ (4.31)

Then, rearranging the expression (4.30), it is found that

$$\delta\left(g(p_{\|})\right) = \left|\frac{\gamma}{p_{\|} - N_{\|}\gamma}\right| \cdot \delta\left(p_{\|} - p_{\|,\pm}(p_{\perp})\right).$$ (4.32)

At this point, the one-dimensional integral form of both the absorption coefficient and of the emissivity is retreived:

$$\alpha_\omega^{(n)}(s) = -\int_0^{+\infty} \left(\frac{n}{\bar{\omega}N_{\perp}}\right)^2 \left|\left(\tilde{e}_x + \frac{\bar{\omega}N_{\perp}}{n}p_{\|,\pm}(p_{\perp}) \cdot \tilde{e}_z\right)J_n(b) - \frac{ib}{n}J_n'(b)\tilde{e}_y\right|^2 \times$$

$$\hat{R}f(s, p_{\|,\pm}(p_{\perp}), p_{\perp}) \times$$ (4.33)

$$2\pi^2\frac{\omega_{p,0}^2}{c_0\omega}\frac{p_{\perp}}{\left(1 + p_{\|,\pm}(p_{\perp})^2 + p_{\perp}^2\right)} \cdot \frac{1}{\left|\frac{p_{\|,\pm}(p_{\perp})}{\gamma} - N_{\|}\right|}\mathrm{d}p_{\perp}$$

$$j_\omega^{(n)}(s) = \int_0^{+\infty} \left(\frac{n}{\bar{\omega}N_{\perp}}\right)^2 \left|\left(\tilde{e}_x + \frac{\bar{\omega}N_{\perp}}{n}p_{\|,\pm}(p_{\perp}) \cdot \tilde{e}_z\right)J_n(b) - \frac{ib}{n}J_n'(b)\tilde{e}_y\right|^2 \times$$

$$f(s, p_{\|,\pm}(p_{\perp}), p_{\perp}) \times$$ (4.34)

$$m_ec_0^2\frac{N_{\omega,ray}^2\omega_{p,0}^2\omega}{4\pi c_0^3}\frac{p_{\perp}}{\left(1 + p_{\|,\pm}(p_{\perp})^2 + p_{\perp}^2\right)} \cdot \frac{1}{\left|\frac{p_{\|,\pm}(p_{\perp})}{\gamma} - N_{\|}\right|}\mathrm{d}p_{\perp}.$$

These integrals are solved using adaptive quadrature algorithms present in the Python SciPy package, derived from the Fortran library QUADPACK. To account for the two roots of $p_{\|,\pm}$, both integrals (4.33) and (4.34) are evaluated as the sum of the two integrals corresponding to the $p_{\|,+}$ and the $p_{\|,-}$ cases, taking into account only the computational steps where the argument of the square root in the equation (4.28) is strictly higher than zero. Another very important point to be made in order to ensure the stability of numerical integration is that in both expressions there are points of singularity where the quadrature algorithm encounters difficulties. These singular points arise because, for some position in the momentum space, the denominator of the expression(4.32) vanishes, leading to wrong infinities. In this case, these points ζ can be expressed as

$$\zeta = \sqrt{\left(N_\parallel \cdot \sigma + n\frac{\omega}{\Omega_{c,0}}\right)^2 - \sigma^2 - 1},$$ (4.35)

where

$$\sigma = \frac{N_\parallel \cdot n\Omega_{c,0}}{\omega\left(1 - N_\parallel^2\right)}.$$ (4.36)

This problem is handled by the QUADPACK routine by splitting the integration grid near the singularity avoiding large numerical errors in the calculations [76].

In figure 4.10 it is possible to see profiles of the absorption coefficient, the optical thickness and the emissivity coefficient for an example TCV shot.

As a final remark, to calculate the absorption coefficient it is necessary to numerically compute the directional derivative present in the differential operator $\hat{R}$. To solve the problem, a two function evaluation in the symmetrized form is chosen[4] [77]:

$$f'(x) \simeq \frac{f(x+h) - f(x-h)}{2h}$$ (4.37)

where h is selected to minimize the roundoff and the truncation errors as

$$h \sim \sqrt{\frac{\varepsilon_f f}{f''}} \sim \sqrt{\varepsilon_f} x_c.$$ (4.38)

in the expression of h, ε_f it is a number which can be chosen to be comparable to the machine accuracy ε_m, while x_c is the curvature scale of the function f which can be chosen to be the variable over which the derivative is performed: in this case $p_\parallel$ and $p_\perp$. By selecting the expression , the calculated derivative achieves a fractional accuracy of $\sqrt{\varepsilon_f}$. To conclude, the expressions for both the derivatives can be written as

$$\frac{\partial}{\partial p_\perp} f(p_\parallel, p_\perp, s) = \frac{\left(f(p_\parallel(s), p_\perp(s) + h_\perp(s)) - f(p_\parallel(s), p_\perp(s) - h_\perp(s))\right)}{2h_\perp}$$ (4.39)

$$\frac{\partial}{\partial p_\parallel} f(p_\parallel, p_\perp, s) = \frac{\left(f(p_\parallel(s) + h_\parallel(s), p_\perp(s)) - f(p_\parallel(s), p_\perp(s) - h_\parallel(s))\right)}{2h_\parallel}.$$ (4.40)

---

[4]It is true for arbitrary numerical distribution functions, while if f is a Mawellian the derivatives are calculated analytically.
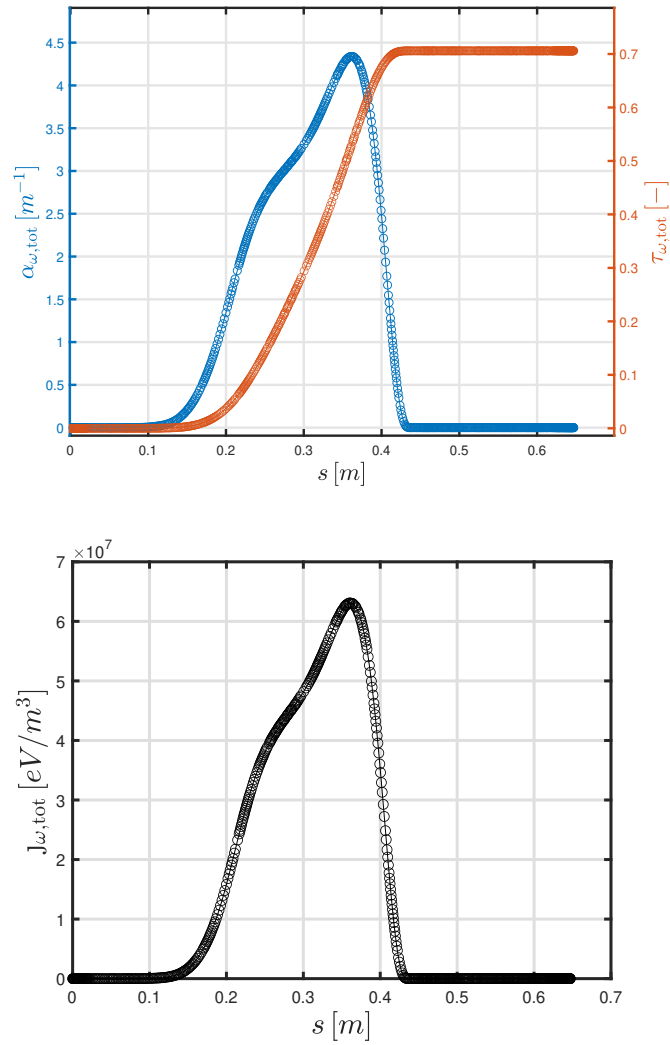
Figure 4.10: (a) Absorption coeffient and optical thickness and (b) Emissivity coefficient against the ray-path s, for the *single ray* VECE YODA simulation of the shot #73003 at $f_{ECE} = 116\,\text{GHz}$ and $t = 1.9\,\text{s}$.

4.3.3.   EC Radiation Transport

A this point, all the ingredients to solve the radiation transport equation are ready. To attain the radiation intensity at the *VECE* antenna, the hypothesis of *single pass* EC radiation (no reflection from the walls) is considered valid. Therefore, the solution of the radiation transport equation in its integral form can be written as

$$I_\omega(s_{ant}) \simeq \int_0^L j_\omega(s)e^{-\tau(s)}\mathrm{d}s. \tag{4.41}$$

The validity of this hypotesis is already discussed in chapter 3. From the *reciprocity theorem* it is possible to propagate the rays from the antenna to the dump and then trace them back from the dump to the antenna, taking as initial position $s = s_{dump}$. This method is not mandatory for ECCD scenarios when the experimental conditions for VECE measurement are matched, but it is of great importance when one is dealing with low density plasmas in the presence of a runaway electron beam since for these scenarios the dump will absorb most of the EC radiation from RE generated outside the VECE antenna pattern. Since the emission function $j_\omega(s)e^{-\tau(s)}$ is, in general, well-behaved, YODA uses a simple trapezoidal quadrature rule to solve equation 4.41, which is less computationally demanding than the adaptive quadrature rule.

4.3.4.   Numerical Distribution Function Interpolation

LUKE operates in the zero orbit-width (ZOW) limit when solving the bounce-averaged Fokker-Planck equation. This means that it disregards the Larmor radius, assuming it to be negligible, and ignores drifts. To simplify the problem, it is customary to express the Fokker-Planck equation in terms of a set of quantities that remain constant along a given flux surface. LUKE uses a set of invariants of the motion: the poloidal flux ψ, the particle momentum p, and the particle pitch $\xi_0 = \cos\theta_0$ at the location of minimum magnetic field strength[5] along the flux surface. The electron distribution function f f is independent of the poloidal angle because it satisfies *Liouville's theorem*. According to this theorem, f remains constant along phase-space orbits, and in this context, it means that f remains constant along particle orbits. Therefore, when expressing f using invariants of particle motion, which identify unique orbits, f becomes independent of the poloidal angle.

In order to evaluate cyclotron emission, it is necessary to determine the local momentum vector $\boldsymbol{p}$ of the particle. Although p is an invariant of motion and remains constant,

---

[5]The subscript 0 indicates that the quantity is evaluated at the location of minimum magnetic field strength along the flux surface.

the particle's pitch ξ varies along the flux surface. Therefore, while integrating the cyclotron emission, one must calculate the value of the LUKE distribution function using a momentum coordinate pair (p, ξ) as the input as

$$f = f[r(s), p, \xi_0(s, \xi)]. \tag{4.42}$$

Requiring that the magnetic moment $\mu = p_\perp^2/2m_e B$ remains unchanged along the flux surface, we can determine the invariant pitch ξ_0:

$$\frac{p^2(1 - \xi^2)}{2m_e B} = \frac{p^2(1 - \xi_0^2)}{2m_e B_{\min}}. \tag{4.43}$$

Then, it is possible to find a relation between ξ_0 and ξ

$$\xi_0^2 = 1 - \frac{B_{min}}{B}(1 - \xi^2) \tag{4.44}$$

Since f must be symmetric about $\xi_0 = 0$ in the trapping region, the sign of ξ_0 can be assumed to be the same as that of ξ. Consequently, in YODA, f is evaluated as

$$f = f\left[r(s), p, \operatorname{sgn}\xi\sqrt{1 - \frac{B_{\min}}{B}(1 - \xi^2)}\right]. \tag{4.45}$$

In YODA, the normalized poloidal flux ψ is interpolated using a rectangular bi-variate spline along R and Z, while the distribution function itself is interpolated using a regular grid interpolator, avoiding expensive triangulation of the input data by taking advantage of its regular grid structure.
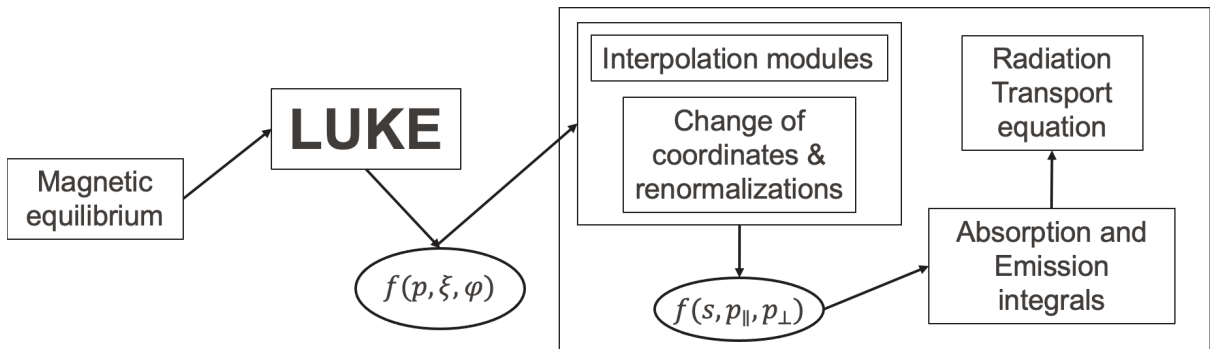
Figure 4.11: Illustration of the connection between LUKE and YODA.

4.3.5.   Thermal Benchmark

Both the YODA benchmark and the antenna pattern convergence study were done using a well diagnosed TCV plasma discharge: the #73003. In this scenario, for the first half of the shot, the magnetic field B_0 is first ramped down from ~ 1.4 T to ~ 0.9 T, while for the second part it is ramped up from ~ 0.9 T to ~ 1.4 T. This evolution of the magnetic field enables the VECE to detect only the X3 thermal radiation from the plasma, for very specific values of the magnetic field itself, without the pollution of thermal X2 emission due to reflections on the tokamak wall shown in figure 4.12. In particular, a time step of $t = 1.9$ s is selected in order to be sure to have a value of the magnetic field which allows X3 thermal emission at the selected frequency of $108.84 GHz$.
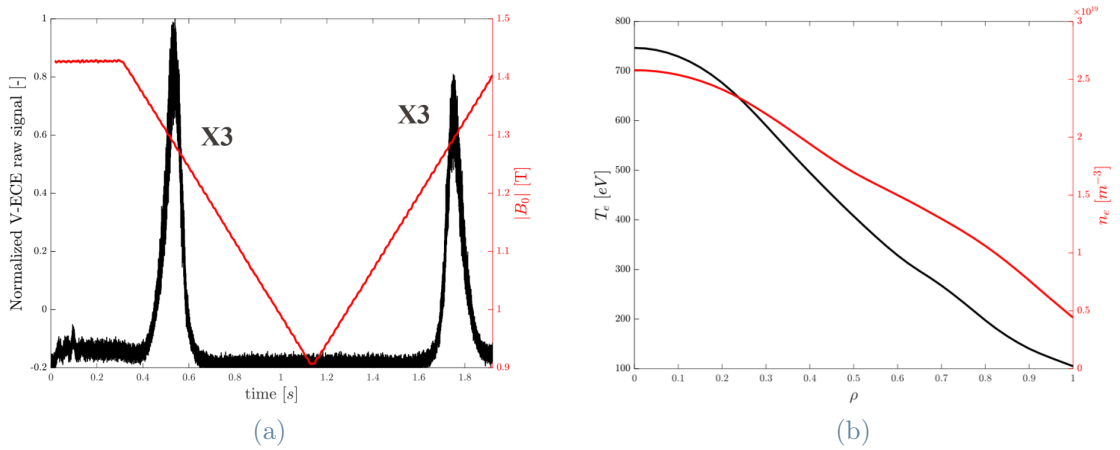
Figure 4.12: Shot #73003: (a) Normalized VECE signal for $f_{ECE} = 108.84$ GHz and tokamak magnetic field B_0 variation - (b) Electron temperature and density from the Thomson scattering.

To assess the validity of the YODA calculations, it is useful to benchmark it against an existing *ECE* synthetic diagnostic, such as SPECE. This comparison is performed for the specific time step of $t = 1.9$ s, the same used for the beam convergence. In this case, a frequency range of $f \sim 113 - 118$ GHz is selected for an X-mode beam composed by only one ray.

This choice can be justified by the fact that, since the convergence of the beam is demonstrated to be guaranteed at 24 rays, using only one ray to mimick the antenna pattern when one wants to benchmark the codes this approach remains general while being easy and convenient. As shown in figures 4.13 and 4.14, the YODA calculations match with very good accuracy the SPECE calculations. Since SPECE is already validated for thermal plasmas on several tokamaks (including TCV), it can be deduced from the correspondence
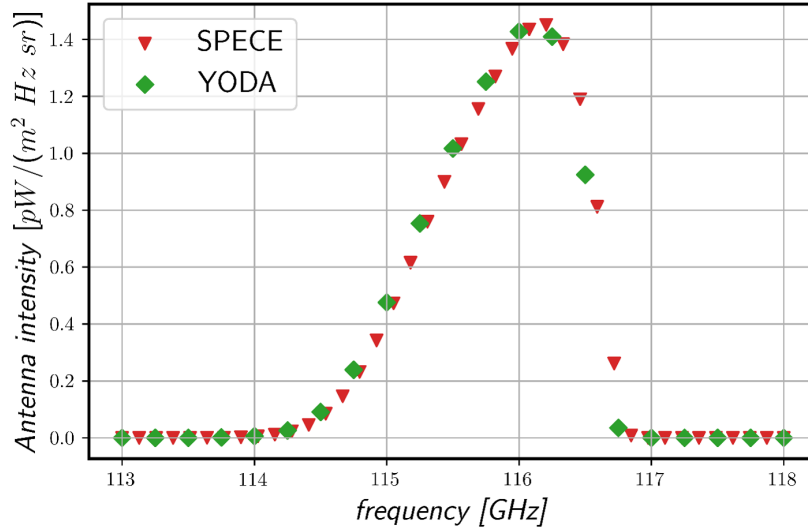
Figure 4.13: Comparison between YODA and SPECE spectral X-mode intensity calculations for $f \sim 113 - 118$ GHz (#73003 $t = 1.9$ s)

between the two results that the calculations produced by the YODA code are valid for thermal plasma scenarios.

In figure 4.14, it is also possible to observe a poor agreement between the calculation of YODA and SPECE before $s = 0.25$ m. This is mainly due to a slightly different calculated ray trajectory before that point, and because of different numerical approaches used in the two codes. In any case, these little differences do not affect strongly the ECE intensity calculations.

In conclusion, it is worth mentioning here that all the synthetic ECE results in this thesis are expressed as spectral intensities. In fact, the possibility of calculating the power bandwidth, although trivial, is not yet implemented in the YODA code, which is only able (for the moment) to calculate the spectral intensity $I(f)$. This is mainly due to the fact that it is time demanding from the computational point of view, therefore an extensive parallelization of the code is needed. It is worth to mention that the transformation (3.2) is, in principle, required for a quantitative comparison between the code results and the experimental measurements. However, as will be explained in chapter 5, it is possible to extract meaningful information from the synthetic intensities trends even without the direct calculation of P_{BW}.
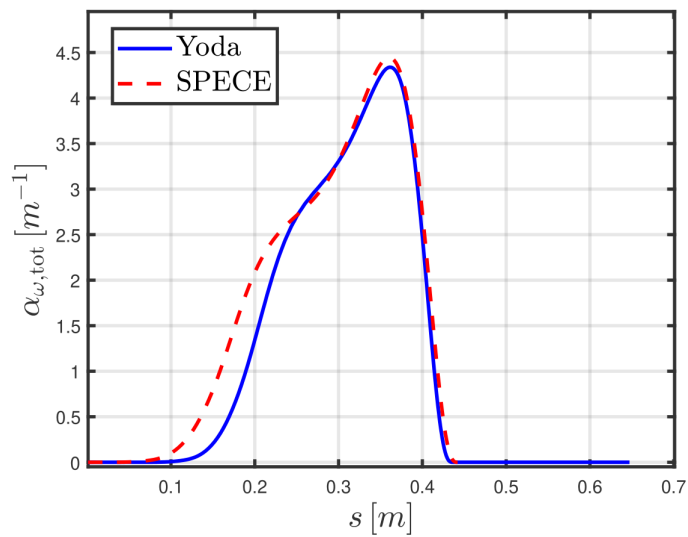
(a)
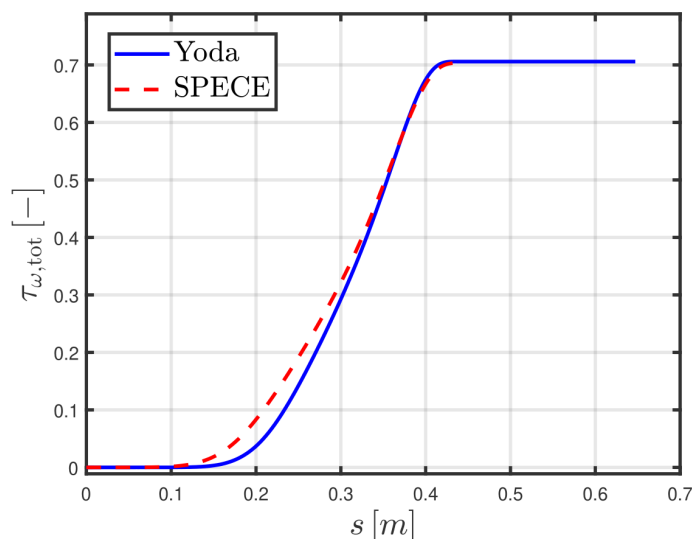
(b)

Figure 4.14: Shot #73003, $f_{ECE} = 116\,\text{GHz}$, $t = 1.9\,\text{s}$: (a) Comparison between YODA and SPECE absorption coefficient vs. ray trajectory - (b) Comparison between YODA and SPECE optical thickness vs. ray trajectory.

5 | Suprathermal Electrons at the Tokamak à Configuration Variable

In this final chapter, VECE synthetic simulations from non-thermal electron scenarios are detailed and compared with experimental measurements.

5.1. Electron Cyclotron Current Drive

5.1.1. Scenario I

The TCV plasma discharge #73217 is an ECCD shot which has been specifically designed to achieve VECE measurements in which thermal and non-thermal EC emission can be observed separately during the shot [8]. Figure 5.1 displays time traces of the discharge parameters and the normalized raw VECE signals for the ECE X-mode radiation, at the frequency of $f_{ECE} = 108.84\,\text{GHz}$. The electron cyclotron heating phase occurs for about 1 second between $\sim 0.3\,\text{s}$ and $\sim 1.3\,\text{s}$ at a constant magnetic field of approximately $1.54\,\text{T}$. The magnetic field strength is kept constant for approximately 100 ms after the heating is turned off until about $\sim 1.4\text{s}$. The field is then ramped down from $1.54\,\text{T}$ to $0.9\,\text{T}$ for the remainder of the discharge. The heating phase takes place at a constant ECH power of around $500\,\text{kW}$ and a constant launcher angle of approximately $10°$. The launcher angle controls the direction of the ECH wave vector with respect to the toroidal magnetic field in the plasma. Perpendicular launching means that the ECH wave purely heats the plasma by increasing the perpendicular energy of the bulk electrons. Increasing the launcher angle allows the ECH wave to resonate with higher energy electrons and selected velocity parallel to the magnetic field, thereby driving a net toroidal current. In this discharge, the plasma current is ramped down along with the magnetic field to maintain a quasi-frozen equilibrium [8]. This preserves the same X-mode polarization from the current drive to the calibration phase.
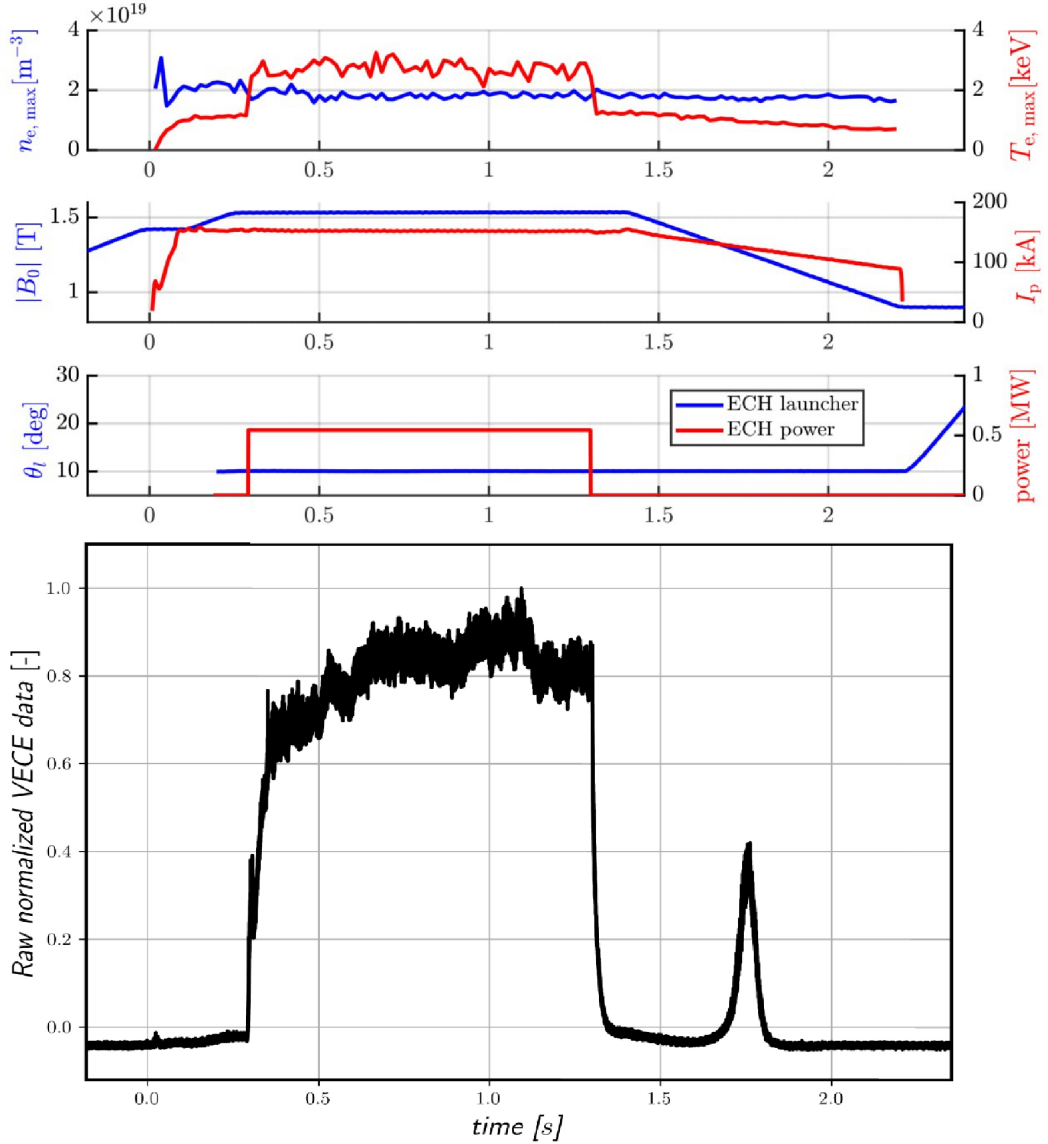
Figure 5.1: Time trace of the main parameters and VECE normalized raw data (108.84 GHz) for the discharge #73217 .

A remarkable feature of this shot is the smooth ramp down of the magnetic field after $t \sim$ 1.4 s, which allows for the identification of thermal peaks for each frequency. This happens because, depending on the measured frequency, during the the ramp down the magnetic field will reach the value needed to match the X3 EC resonance condition (equation (2.63)). As an example, for the measured frequency of 108.84 GHz shown in figure 5.1, the thermal peak is observed around $t \sim 1.7$ s for a magnetic field value of $B \sim 1.2$ T. The thermal peak provides a self-calibration reference for the discharge #73217, using the value of the ECE synthetic power calculated at the thermal peak.

The radiation intensity decreases for all measured energies as soon as the heating is turned off at 1.3 s. This decrease in radiation intensity indicates that the radiation detected during the current drive phase is mainly produced by non-thermal electrons, with little or no contribution from thermal electrons for the observed frequency 108.84 GHz. The intensity level of the polluting background radiation is higher for lower frequencies due to the X2 cold resonances of lower frequencies being located at higher major radii in the plasma. In fact, for frequencies that have their thermal X2 cold resonance position in the plasma, the measured radiation during current drive is a combination of both thermal and non-thermal radiation. In the specific case of interest, the chosen frequency of 108.84 GHz is high enough to ensure that the background radiation is not polluting the measurements [8].

Simulations results

In order to simulate the synthetic VECE spectrum of the shot #73217, a specific strategy has been chosen. Firstly, it is crucial to understand how much the VECE line fluctuate from the perfectly vertical configuration due to mechanical vibrations. Hence, the time evolution of the V-ECE expected thermal peak has been simulated with YODA for different inclinations. In this case, the experimental trend is matched using an inclination of 1° towards the TCV HFS in the c3po simulations[1].

Once the appropriate line of sight has been chosen, one can proceed with the YODA simulation of the whole shot. To properly take into account the electric field response for a plasma current density variation in time, LUKE is set up to solve the drift kinetic equation using time dependent simulations and solving the induction equation. The main difference between *time independent* and *time dependent* LUKE simulations resides in the fact that in the former case one is looking for a time-asymptotic solution (i.e. $\partial f/\partial t = 0$). Time-independent calculations are much faster but only applicable during steady-state plasma phases. The time discretization of the drift-kinetic simulations in LUKE is chosen equal to the Thomson scattering time resolution[2] of ~ 60 Hz.

In the kinetic simulations, emphasis was placed on transitions between heating and non-heating phases. The time discretization used in the transition intervals is more refined with respect to the *steady state* ECH phase. In the kinetic simulations, fast electron radial transport is neglected (i.e. $\mathbb{D}_r = 0$) and the electron driven toroidal current calculated

---

[1]Actually, this corresponds to $\beta = 180° - 1°$ in c3po settings.

[2]This choice is driven by the fact that LUKE takes the Thomson scattering profiles for the electron temperature and density as input. In principle, it is possible to have a more refined time resolution interpolating the Thomson profiles in time.

by LUKE, accounting for ECRH and Ohmic heating, matches the plasma current with less than 10% difference. In this simulation, named NHU100PL,a loss term for runaway electrons that is proportional to the ECRH power is included to account for the enhanced runaway electron transport observed in many recent experiment in the presence of ECRH.

The synthetic VECE intensity calculated by YODA for the shot #73217 at the observed frequency of 108.84 GHz are shown in figures 5.2 and **??**. First of all, simulations predict with good accuracy the VECE experimental trend during the steady ECH phase. Also, the VECE signal behaviour right after the heating is turned off is well matched. It means that in the ~ 100 ms in which the ECH is turned off, while the magnetic field is left constant, the electron distribution function is predicted to come back to the Maxwellian distribution. It also confirms that all the measured EC emission in that case comes from suprathermal ~ 60 keV electrons generated during the ECCD phase.
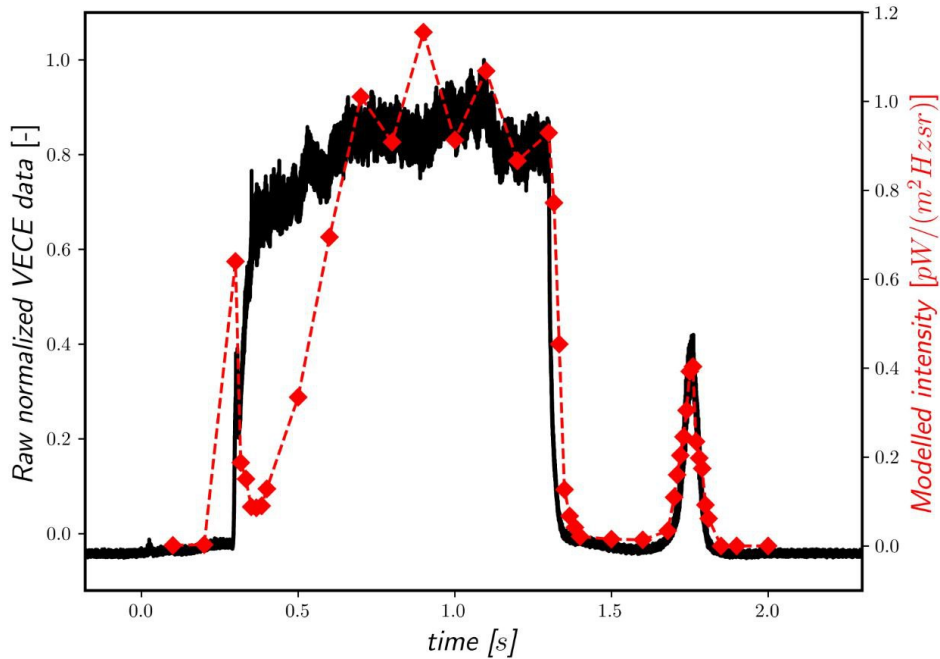
Figure 5.2: Comparison between synthetic VECE intensity trends for NU100PL case and VECE raw data measured at 108.84 GHz in the #73217 disharge.

On the other hand, it is clear that the synthetic VECE intensity is strongly underestimated during the heating onset. As shown in figure 5.3, the variation in time of the fraction of 60keV electrons coming from the kinetic simulations predicts a small number of non thermal electrons in the simulations, during the first phase of the heating. There is a clear correlation between this fact and the underestimation of the modelled intensity, also confirmed by the fact that the rise of the predicted number of fast electrons corresponds,

in time, to the rise of the synthetic VECE signal. Further investigations are needed to understand the reasons why the models do not match the experimental trends in the initial phase.
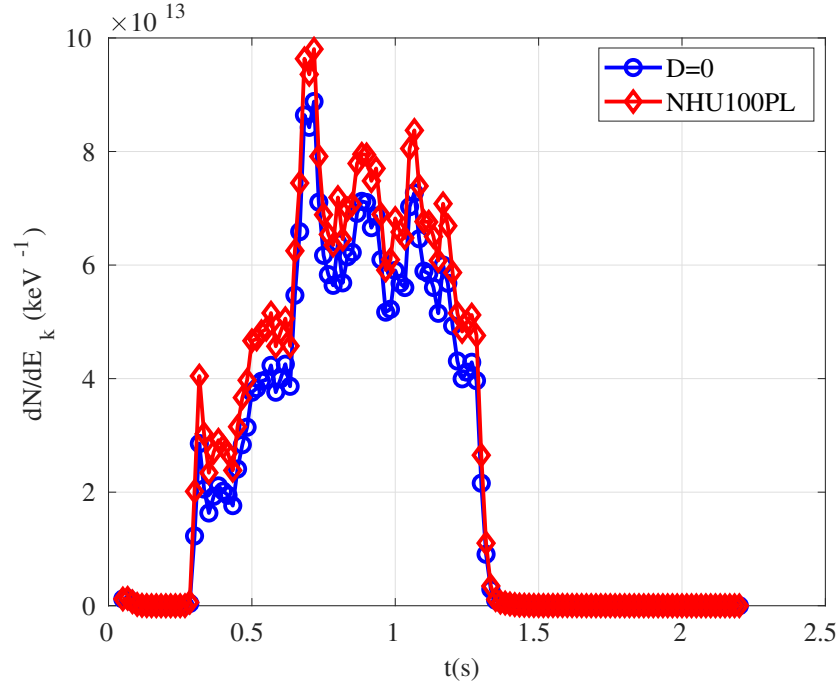
Figure 5.3: Time evolution of the $\sim 60\,\mathrm{keV}$ electrons corresponding to the measured frequency of $108.84\,\mathrm{GHz}$.

5.1.2.   Scenario II

In TCV shot #72644, the ECH power has a value similar to that of the hybrid discharge #73217, while the launcher angle is varied in 5 stationary steps between 0.7 s and 1.9 s. Here as well, the toroidal angle of the X2 launcher is kept constant at $\sim -90°$. The variation of the poloidal angle of the launcher from $\sim -10°$ to $\sim -26°$ in each stationary step leads to stair-shape X-mode intensities, as is shown in figure 5.4. Also, in this case, before the heating phase, the signal level is close to the noise level. When the heating is turned on at $\sim 0.7\,\mathrm{s}$, a sharp increase of the VECE signals is observed. This means that these measurements are not polluted by background radiation.

As shown in figure 5.4, at the ECH onset, only the higher frequency shows a sharp increase in measured intensity. The lower frequency signal - corresponding to a higher energy - increases only at the third step in poloidal angle. Note that the corresponding jump is
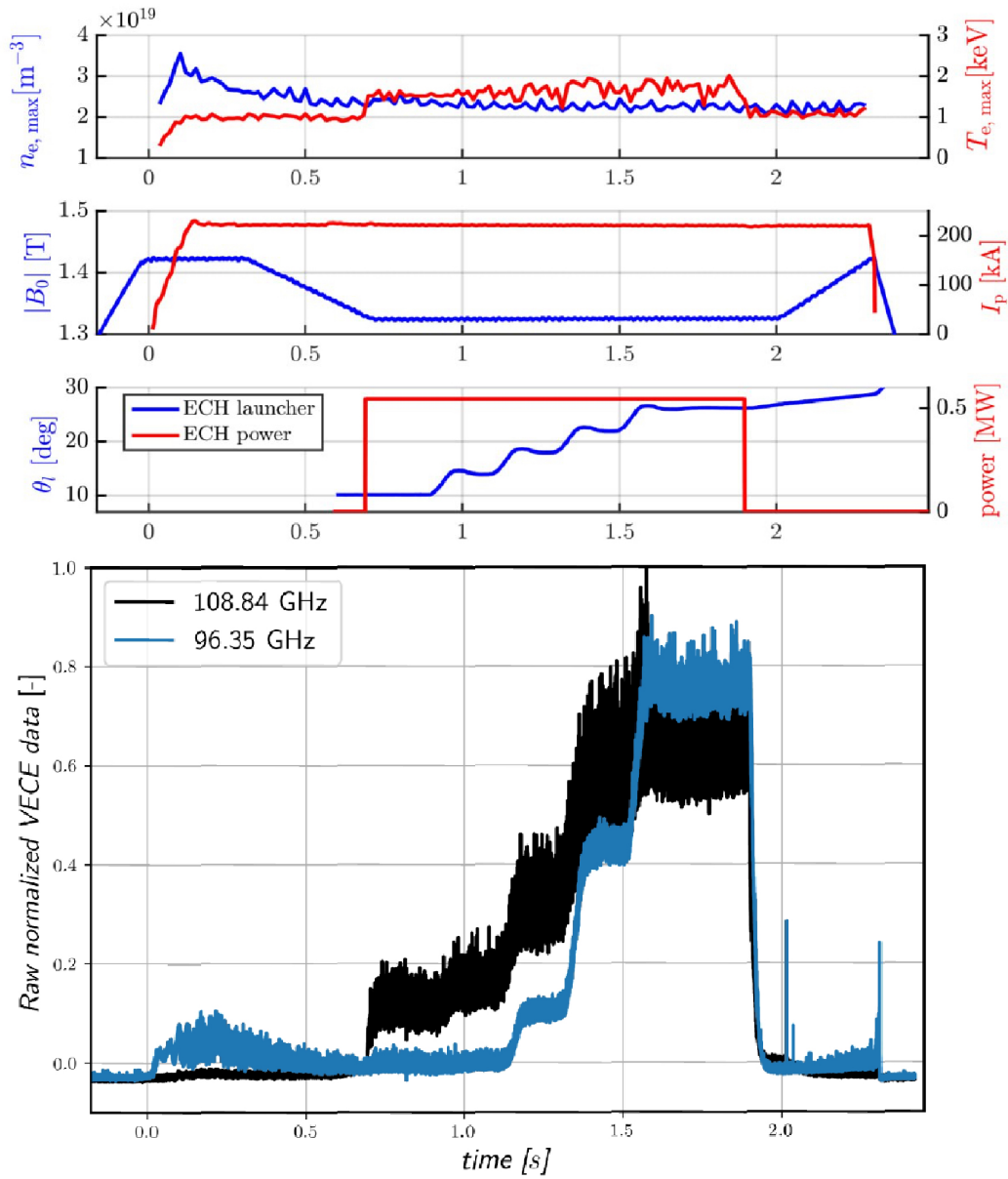
Figure 5.4:   Time trace of the main parameters and VECE normalized raw data (108.84 GHz and 96.35 GHz) for the discharge #72644 .

higher than that of the higher frequency.

Simulations of the ECH wave interaction with the plasma in discharge #72644 are conducted using the C3PO code [8]. The power deposition profiles of the ECH in the plasma vs the radial position ρ are displayed in figure 5.5.
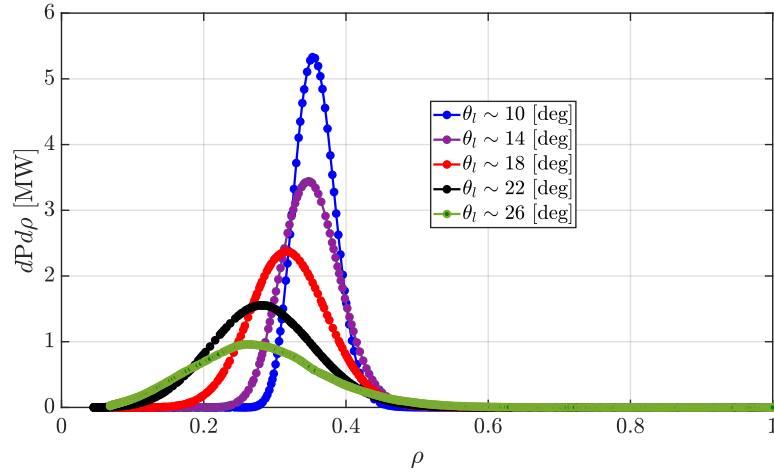
Figure 5.5: Profile of the power deposition in the plasma for the various launcher angles, swept during the discharge [8].

Simulations results

The emphasis in the simulations of the #72644 VECE spectrum was placed in predicting the intensity jumps between the different steady state ECH phase and relate measurements to the density of fast electrons at selected frequencies. It is not necessary to do *time dependent* calculations in the kinetic simulation since the successive phases of constant ECH poloidal angle are sufficiently long to assume a quasi-steady state. Radial transport of fast electrons must be included to match the experimental plasma current during LUKE iterations. To stress the differences between the case in which the radial transport is taken into account and the one in which it is not accounted for two sets of simulations are carried out for two different ECE frequencies: $108.84\,\mathrm{GHz}$ (figure 5.6) and $96.35\,\mathrm{GHz}$ (5.7).

The first kinetic simulation performed using a zero diffusion coefficient ($\mathbb{D}_r = 0$) overestimates the experimental plasma current. In this case, it is useful to inspect the left hand side of figures 5.8 and 5.9, where the logarithm of the LUKE distribution functions, integrated over the pitch angle ξ, are shown in contour plots with respect to the normalized electron momentum p and the radial location ρ, for each simulated time-step. Taking advantage of this figure, it is possible to observe the presence of a spike of highly energetic electrons at the radial position in which the ECH power is deposited.

Including radial transport is turned on with an ad-hoc diffusion coefficient of $\mathbb{D}_r = 5$, LUKE matches the experimental plasma current, and the computed electron distribution function is strongly different from the no-transport case. In fact, as can be seen in the right panels of the same figures 5.8 and 5.9, the predicted energy peak is still at the radial
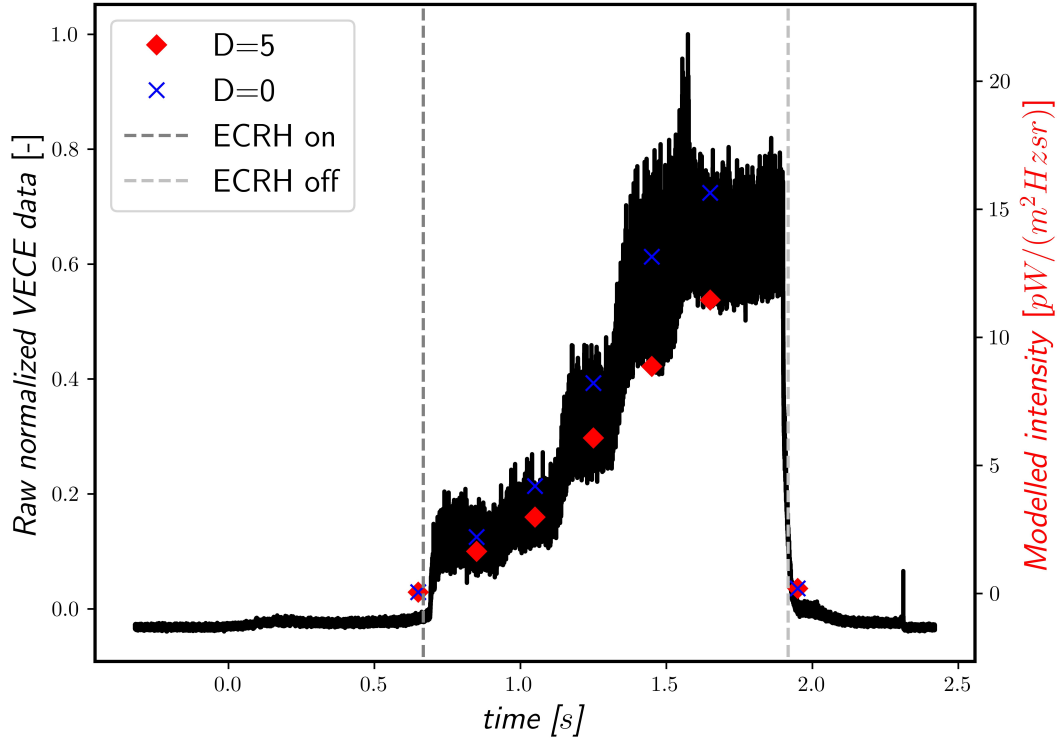
Figure 5.6: Comparison between synthetic VECE intensity trends for $\mathbb{D}_r = 0$ and $\mathbb{D}_r = 5$ and VECE normalized raw data measured at $108.84\,\mathrm{GHz}$ in the #72644 disharge.

position of the ECH power deposition, but it is are less pronounced with respect to the electron momentum values.

The differences in the two kinetic simulations have a strong impact on the YODA VECE synthetic profiles, for both the simulated frequencies.

Both sets of simulations predict the step-like evolution of the VECE signal, with the $\mathbb{D}_r = 0$ simulation slightly overestimating the signal and the $\mathbb{D}_r = 5$ simulation slightly underestimating it, both sets of frequencies.

For the lower frequency - corresponding to the higher energy - the difference between the $\mathbb{D}_r = 0$ and the $\mathbb{D}_r = 5$ cases is more pronounced, with the $\mathbb{D}_r = 5$ case being sensibly closer to experimental measurements. With the better match of the toroidal current, this seems to indicate that radial transport of fast electrons indeed plays an important role.

In conclusion, looking at both the synthetic VECE intensities and the related energy maps, it is possible to conclude that a more accurate anomalous transport model is needed to match the experimental results, but still these simulations constitute a good starting point for further investigations of fast electron physics.
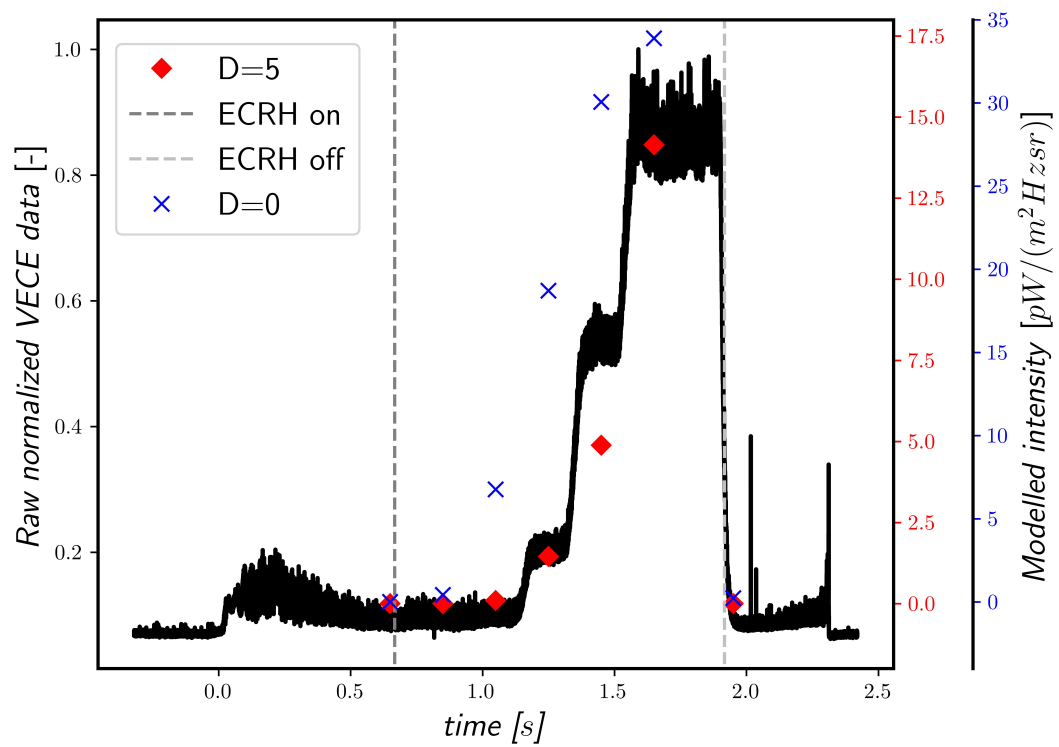
Figure 5.7: Comparison between synthetic VECE intensity trends for $\mathbb{D}_r = 0$ and $\mathbb{D}_r = 5$ and VECE normalized raw data measured at $96.35\,\mathrm{GHz}$ in the #72644 disharge.
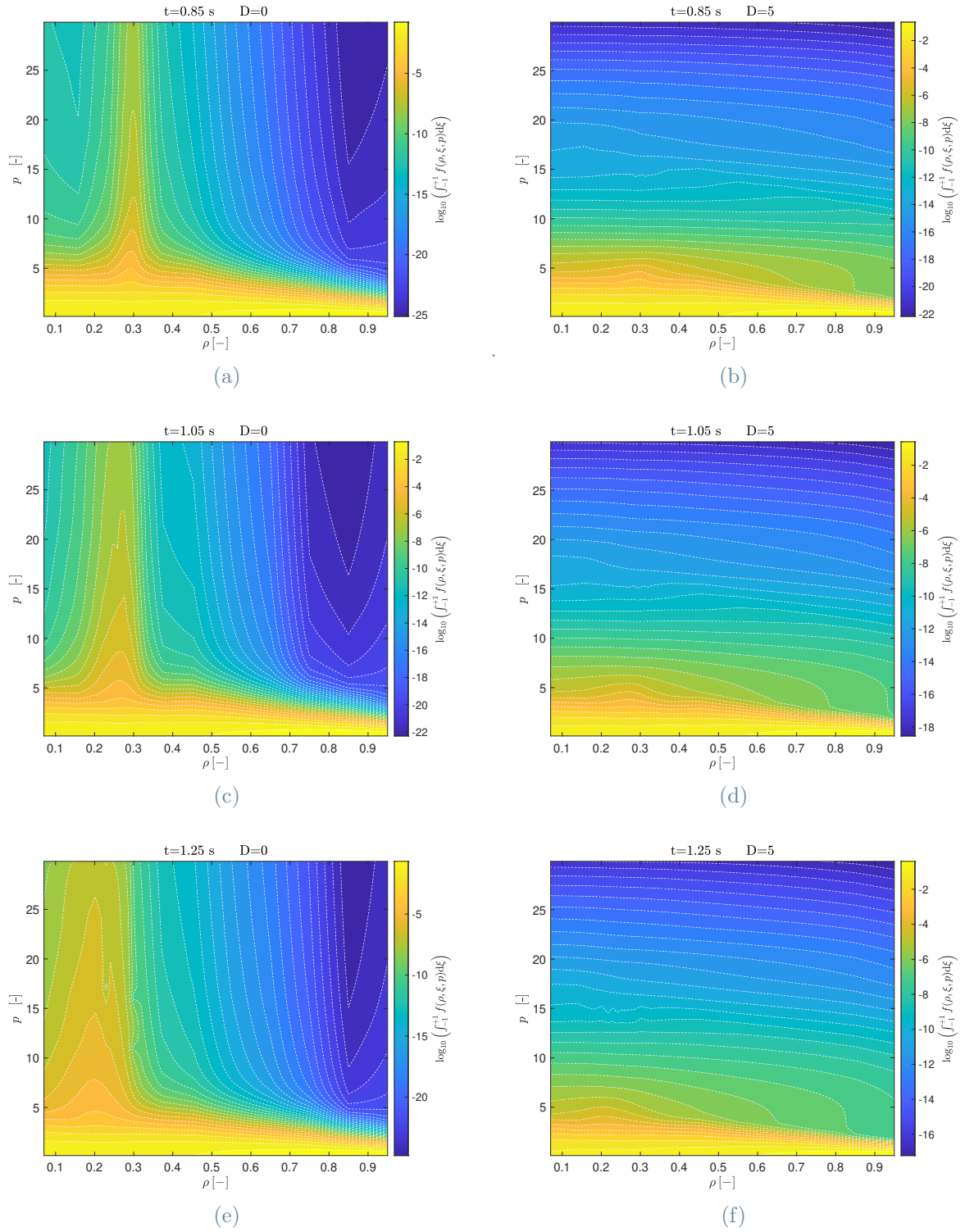
Figure 5.8: Energy map evolution of the simulated distribution function on logarithmic scale, for the #72644 discharge (part 1).
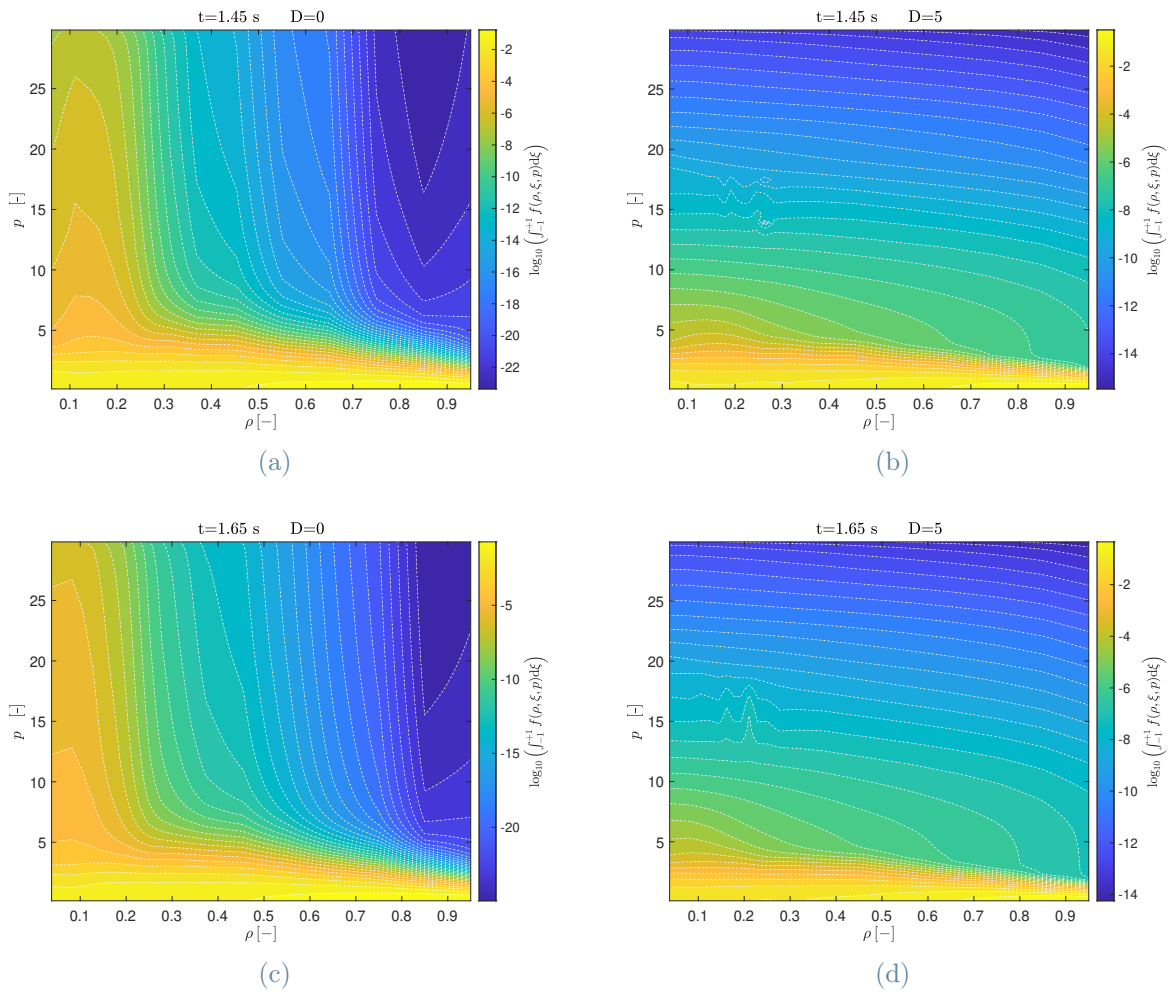
Figure 5.9: Energy map evolution of the simulated distribution function ($\mathbb{D}_r = 0$ and $\mathbb{D}_r = 5$) on logarithmic scale, for the #72644 discharge (part 2).

Conclusion and Perspectives

The research goals at the beginning of this master thesis were

- To model the VECE detection system (antenna);

- To model the EC emission and (re)absorption based on the electron any arbitrary distribution funciton;

- To model the transport of EC radiated power along the propagation path;

The VECE detection system was successfully modeled through the use of the raytracing code C3PO. In the vertical configuration, a good convergence is achieved for 24 rays in the pattern, disposed in a 4×6 configuration, as described in section 4.1. Also, it allows the simulation of any arbitrary line of sight, opening the possibility of using it not only for the vertical ECE, but also for low field side ECE and oblique ECE.

The YODA code was developed. It is a new general ECE synthetic diagnostic which allows the calculations of EC emission and (re)absorption taking into account the electron distribution function. It is also able to calculate the EC radiation transport through the plasma. YODA was first validated for thermal plasmas, using an analytical Maxwellian distribution, through the comparison with the ECE synthetic diagnostic SPECE. By comparing the simulations of the TCV plasma discharge #73003, a match can be observed between the absorption and spectral intensity profiles calculated by both codes.

Also, YODA was coupled with the 3D fully relativistic bounce-averaged Fokker-Planck code LUKE, allowing the reconstruction of ECE spectra taking into account arbitrary numerical distribution function. This is the main achievement of this work.

The VECE spectra of two TCV ECCD plasma scenarios (I : #73217 and II : #72644) were analyzed. For the first time, experimental VECE measurements were qualitatively compared with Fokker-Planck modeling (LUKE) coupled to the ECE synthetic diagnostic (YODA - C3PO).

For *scenario* I, a time dependent kinetic simulation was carried out with a zero ad-hoc diffusion coefficient ($\mathbb{D}_r = 0$), the induction equation and runaway electrons which

accelerate above the maximum resolved momentum value accounted for. This simulation leads to good agreement between the VECE raw data (for the radiometer frequency $f_{ECE} = 108.84\text{GHz}$) and the synthetic intensity trends for $t > 0.6\,\text{s}$. In fact, during the ECCD onset, an underestimation of both the synthetic VECE signal and of the fraction of suprathermal electrons is predicted. This is probably due to the fact that, for this shot, the experimental plasma current density profile is not matched by the one calculated during the kinetic simulations, not having accounted for anomalous transport.

In *scenario* II, emphasis was placed in predicting the intensity jumps between the different steady state ECH phases, in the VECE signal. To do that, it is suffient to do time-independent kinetic simulations. In this case two different ECE frequency were taken into account ($f_{ECE} = 108.84\text{GHz}$ and $f_{ECE} = 96.35\text{GHz}$). When a constant diffusion coefficient $\mathbb{D}_r = 5$ is taken into account, the current density profile calculated in the kinetic simulation shows a good agreement with the experimental measurements. Also, the VECE synthetic trend is in agreement with the experimental VECE raw data for the most majority of simulated time steps.

As a remark, the major limitation of this work is that the synthetic ECE simulations can not be compared directly with the experimental measurements by a quantitative point of view; therefore they must be considered only preliminary. This is mainly due to

- The lack of the the power bandwidth calculation for each simulated VECE channel;

- The lack of a valid error estimation method for the synthetic results.

The first future development of this thesis should be to overcome these limitations.

The calculation of the power bandwidth is numerically straightforward, therefore it does not constitute a big problem. On the other hand, the main challenge will be the integration of YODA in the STARWARS suite, allowing extensive parallel calculations, reducing the running time. An idea could be to better couple YODA and C3PO in order to launch in parallel, for each time step, simulation of different EC frequencies, while the kinetic simulations are running. It should not be a big issue, since the LUKE simulations are more time demanding than the YODA - C3PO ones, for each time step.

For what concerns the error estimation, the most important sources of error should be the uncertainties linked to the Thomson scattering electron temperature and density profiles and the ones related to the magnetic equilibrium reconstruction and the ones. Further investigations are needed to find a suitable way to propagate all the errors.

Future developments of this work do not stop to these two issues. In fact, as an example, now that the STARWARS code suite is equipped with both synthetic ECE and synthetic

hard x-ray spectroscopy (HXRS) diagnostics, it will be possible to make multiple constain kinetic simulations which should help to resolve some of the standing issues by simultaneously using the data of the two diagnostics that are complementary in their multi-dimensional resolution. This could open up new paths in understanding suprathermal electron dynamics and associated phenomena, ranging from ECRH to MHD to runaway generation.

Bibliography

[1] M. Afsar and K. Button. Precise millimeter-wave measurements of complex refractive index, complex dielectric permittivity and loss tangent of GaAs, si, SiO/sub 2/, a1/sub 2/o/sub 3/, BeO, macor, and glass. *IEEE Transactions on Microwave Theory and Techniques*, 31(2):217–223, Feb. 1983. doi: 10.1109/tmtt.1983.1131460. URL `https://doi.org/10.1109/tmtt.1983.1131460`.

[2] F. Albajar. Electron-cyclotron absorption in high-temperature plasmas: quasi-exact analytical evaluation and comparative numerical analysis. *Plasma Phys. Control. Fusion*, 49:15–29, 2007.

[3] V. V. Alikaev and V. V. Parail. Current drive by electron cyclotron waves. *Plasma Physics and Controlled Fusion*, 33(13):1639, nov 1991. doi: 10.1088/0741-3335/33/13/011. URL `https://dx.doi.org/10.1088/0741-3335/33/13/011`.

[4] M. E. Austin, J. Lohr, B. J. Tobias, M. W. Brookman, A. G. Kellman, C. K. Phillips, and D. M. Thomas. Electron cyclotron emission radiometer upgrade on the diii-d tokamak. *Review of Scientific Instruments*, 74(3):1457–1459, 2003. doi: 10.1063/1.1530387.

[5] G. Bekefi. *Radiation Processes in Plasmas*. John Wiley Sons, New York, 1966.

[6] S. T. Beliaev and G. I. Budker. Soviet physics doklady. 1:218, 1956.

[7] A. T. Biwole. Characterization of components for the hfs ece radiometer on tcv. Technical report, Swiss Plasma Center, Oct 2018.

[8] A. T. Biwole. *Measurement the electron energy distribution in tokamak plasmas from polarized electron cyclotron radiation*. PhD thesis, ÉCOLE POLYTECHNIQUE FÉDÉRALE DE LAUSANNE, 2023.

[9] A. T. Biwole, L. Figini, L. Porte, and A. Fasoli. The plasma as a calibration source for ece diagnostics. submitted to Nuclear Fusion, 2023.

[10] A. T. Biwole, L. Porte, S. Coda, and A. Fasoli. The vertical ece of tcv. submitted to review of scientif instruments, 2023.

[11] J. P. Bizarro, Y. Peysson, P. T. Bonoli, J. Carrasco, T. Dudok de Wit, V. Fuchs, G. T. Hoang, X. Litaudon, D. Moreau, C. Pocheau, and I. P. Shkarofsky. On self-consistent ray-tracing and fokker-planck modeling of the hard x-ray emission during lower hybrid current drive in tokamaks. *Physics of Fluids B: Plasma Physics*, 5(9): 3276–3283, 1993.

[12] P. Blanchard. *'Etudes du rayonnement suprathermnique emis lors du chauffage cyclotronique electronique du plasma du tokamak TCV*. PhD thesis, ECOLE POLYTECHNIQUE F'ED'ERALE DE LAUSANNE, 2002.

[13] J. M. Blatt and V. F. Weisskopf. *Theoretical nuclear physics*. Springer, New York, 1952. ISBN 978-0-471-08019-0. doi: 10.1007/978-1-4612-9959-2.

[14] P. T. Bonoli. Linear theory of lower hybrid heating. *IEEE Transactions on Plasma Science*, PS-12(2):95–107, 1984.

[15] P. T. Bonoli and R. C. Englade. Simulation model for lower hybrid current drive. *Phys. Fluids*, 29(9):2937–2950, 1986.

[16] M. Bornatici and F. Engelmann. Electron cyclotron emission and absorption in fusion plasmas. *Nucl. Fusion*, 23:1153–1257, 1983.

[17] M. Bornatici and F. Engelmann. Electron-cyclotron absorption and emission: "vexatae quaestiones". *Physics of Plasmas 1*, 1994.

[18] R. U. Bornatici, M. The fully relativistic dielectric tensor for electron cyclotron interaction in a maxwellian plasma. *Il Nuovo Cimento*, D 6:231–250, 1985.

[19] T. J. M. Boyd and J. J. Sanderson. *The Physics of Plasmas*. Cambridge University Press, Jan. 2003. doi: 10.1017/cbo9780511755750. URL `https://doi.org/10.1017/cbo9780511755750`.

[20] B. J. Braams and C. F. F. Karney. Differential form of the collision integral for a relativistic plasma. *Physical Review Letters*, 59(16):1817–1820, 1987. doi: 10.1103/PhysRevLett.59.1817.

[21] B. N. Breizman, P. Aleynikov, E. M. Hollmann, and M. Lehnen. Physics of runaway electrons in tokamaks. *Nuclear Fusion*, 59(8):083001, June 2019. doi: 10.1088/1741-4326/ab1822. URL `https://doi.org/10.1088/1741-4326/ab1822`.

[22] R. Causey. Hydrogen isotope retention and recycling in fusion reactor plasma-facing components. *Journal of Nuclear Materials*, 300(2-3):91–117, 2002.

[23] J. Cazabonne, P. Donnel, S. Coda, J. Decker, G. Di Giannatale, A. Iantchenko,

U. Kumar, Y. Peysson, L. Porte, S. Rienäcker, A. Tema-Biwole, L. Villard, and T. Team. Experimental and numerical investigations of electron transport enhancement by electron-cyclotron plasma-wave interaction in tokamaks. *Plasma Physics and Controlled Fusion.*

[24] J. Cazabonne, P. Donnel, S. Coda, J. Decker, G. Di Giannatale, A. Iantchenko, U. Kumar, Y. Peysson, L. Porte, S. Rienäcker, T.-B. A., and L. Villard. Experimental and numerical investigations of electron transport enhancement by electron-cyclotron plasma-wave interaction in tokamaks. *submitted to Plasma Physics and Controlled Fusion*, 2023.

[25] F. F. Chen. *Plasma Physics and Controlled Fusion.* Springer, 1984.

[26] D. Choi. Experimental analysis of suprathermal electrons generated by electron cyclotron waves in tokamak plasmas. *Journal of Plasma Physics*, 86(2):905860201, 2020.

[27] I. Classen, J. Boom, M. Brix, M. de Baar, Y. Liang, D. Moseev, H. van der Meiden, R. Jaspers, A. Donne, and B. Tobias. Dual array 3d electron cyclotron emission imaging at asdex upgrade. *Review of Scientific Instruments*, 85(11):11D833, 2014.

[28] S. Corning. Macor® machinable glass ceramic for industrial applications. Technical report, 2012.

[29] J. Decker and M. Hoppe. Validation of the ampere-faraday equations resolution in luke. Technical report, ecole polytechnique fédérale de lausanne, 2023.

[30] J. Decker and Y. Peysson. Dke: A fast numerical solver for the 3d drift kinetic equation. EUR-CEA-FC-1736 EUR-CEA-FC-1736, Euratom-CEA, 2004.

[31] J. Decker and A. Ram. Relativistic description of electron bernstein waves. *Physics of Plasmas*, 13(11):112503, 2006. doi: 10.1063/1.2366585. URL `https://doi.org/10.1063/1.2366585`.

[32] J. Decker et al. Full conversion from ohmic to runaway electron driven current via massive gas injection in the tcv tokamak. *Nuclear Fusion*, 62(7):076038, May 2022. doi: 10.1088/1741-4326/ac544e. Cited on pp. 6, 9.

[33] S. Denk. *Study of non-thermal energy distribution functions by modeling of electron cyclotron emission from the fusion plasma of the ASDEX Upgrade tokamak.* PhD thesis, TUM, Ph.D thesis in physics, 2019.

[34] H. Dreicer. Electron and ion runaway in a fully ionized gas. I. *Phys. Rev.*, 115(2): 238–249, July 1959.

[35] H. Dreicer. Electron and ion runaway in a fully ionized gas. II. *Phys. Rev.*, 117(2): 329–342, Jan. 1960.

[36] A. K. et al. Ray-tracing study of electron-cyclotron heating in toroidal geometry. *Tech. rep. Princeton Univ. Plasma Physics Lab.*, 1983.

[37] E. P. et al. Torbeam, a beam tracing code for electron-cyclotron waves in tokamak plasmas. *Computer Physics Communications*, 136:pp. 90–104, 2001.

[38] D. Farina. A quasi-optical beam-tracing code for electron cyclotron absorption and current drive: Gray. *Fusion Science and Technology*, 52, 2007.

[39] F. Felici. ECPOL: Equations and MATLAB Tools for EC Wave Reflection and Polarization Calculations. Technical report, Centre des Recherches en Physique des Plasmas, Ecole Polytechnique Fédérale de Lausanne, Feb. 2012.

[40] L. Figini. *Electron Cyclotron Emission in Tokamaks: development of a new modeling tool for data validation, analysis and predictions*. PhD thesis, Università degli studi di milano, Ph.D thesis in physics, astro-physics and applied physics, 2009.

[41] N. J. Fisch and A. H. Boozer. Creating an asymmetric plasma resistivity with waves. *Phys. Rev. Lett.*, 45:720–722, Sep 1980. doi: 10.1103/PhysRevLett.45.720.

[42] M. Fontana. *Turbulence studies in TCV using the correlation ECE diagnostic*. PhD thesis, EPFL, Ph.D thesis in tokamak physics, 2018.

[43] G. Giruzzi et al. Observation of the m=1 mode by microwave transmission measurements in tore supra. *Nuclear Fusion*, 31(11):2158–2162, Nov 1991. doi: 10.1088/0029-5515/31/11/013. Cited on page 16.

[44] G. Giruzzi et al. Measurement of the time constants of fast electron distributions in the tore supra tokamak. *Physical Review Letters*, 74(4):550–553, Jan 1995. doi: 10.1103/physrevlett.74.550. Cited on page 16.

[45] S. Gnesin. *Electron Cyclotron Heating and Suprathermal Electron Dynamics in the TCV Tokamak*. Doctoral dissertation, Ecole Polytechnique Fédérale de Lausanne, Lausanne, Switzerland, October 2011.

[46] M. R. H. Ritchie and P. Rosado. Energy. *Our World in Data*, 2020. https://ourworldindata.org/energy.

[47] H.-J. Hartfuß and T. Geist. *Fusion Plasma Diagnostics with mm-Waves*. Wiley-VCH Verlag GmbH & Co. KGaA, Sept. 2013. doi: 10.1002/9783527676279. URL https://doi.org/10.1002/9783527676279.

[48] H. P. Helander and D. J. Sigmar. *Collisional Transport in Magnetized Plasmas*. Cambridge University Press, 2002. ISBN 9780521020985.

[49] P. Helander and S. Dieter J. *Collisional Transport in Magnetized Plasmas*. Cambridege university press.

[50] T. C. Hender et al. Chapter 3: Mhd stability, operational limits and disruptions. *Nuclear Fusion*, 47(6):S128–S202, June 2007. doi: 10.1088/0029-5515/47/6/S03. Cited on page 2.

[51] Hofmann. Plasma phys. control. fusion. *Plasma Physics and Controlled Fusion*, 36: B277, 1994.

[52] F. Hofmann et al. Stability and energy confinement of highly elongated plasmas in tcv. *Plasma Physics and Controlled Fusion*, 43(12A):A161–A173, 2001. doi: 10.1088/0741-3335/43/12a/312.

[53] M. Hoppe. *Runaway-electron model development and validation in tokamaks*. PhD thesis, Chalmers University of Technology, 2021.

[54] I. H. Hutchinson. *Principles of Plasma Diagnostics*. Cambridge University press, 1966.

[55] F. Imbeaux and Y. Peysson. Ray-tracing and fokker–planck modelling of the effect of plasma current on the propagation and absorption of lower hybrid waves. *Plasma Physics and Controlled Fusion*, 47(11):2041, oct 2005. doi: 10.1088/0741-3335/47/11/012. URL https://dx.doi.org/10.1088/0741-3335/47/11/012.

[56] F. Imbeaux and Y. Peysson. Ray-tracing and fokker-planck modelling of the effect of plasma current on the propagation and absorption of lower hybrid waves. *Plasma Physics and Controlled Fusion*, 47(11):2041–2065, 2005.

[57] IPCC. *Climate Change 2022: Mitigation of Climate Change. Contribution of Working Group III to the Sixth Assessment Report of the Intergovernmental Panel on Climate Change*. Cambridge University Press, Cambridge, UK and New York, NY, USA, 2022. doi: 10.1017/9781009157926.

[58] P. J. J. P. Freidberg. *Plasma Physics and Fusion Energy*. Cambridge University Press, 2007. doi: 10.1017/CBO9780511755705.

[59] S. J. Janz. *Analysis of Nonthermal Electron Cyclotron Emission During Electron Cyclotron Current Drive Experiments on the DIII-D Tokamak*. PhD thesis, 1992.

[60] K. Kato. *Diagnosis of Mildly Relativistic Electron Velocity Distributions by Electron Cyclotron Emission in the Alcator C Tokamak*. PhD thesis, Massachusetts Institute of Technology, 1986.

[61] I. Klimanov. *Reconstruction of the electron distribution function during ecrh/eccd and magnetic reconnection events in a tokamak plasma*. PhD thesis, ÉCOLE POLYTECHNIQUE FÉDÉRALE DE LAUSANNE, 2005.

[62] Y. Kogi, K. Kawahata, Y. Nagayama, J. Kim, Y. Kim, H. Park, K. Lee, J. Lee, K. Lee, J. Hong, et al. Development of multichannel intermediate frequency system for electron cyclotron emission radiometer on kstar tokamak. *Review of scientific instruments*, 79(10):10F115, 2008. doi: 10.1063/1.2969633.

[63] T. C. Luce. *Superthermal electron distribution measurements with electron cyclotron emission*. PhD thesis, Princeton University, 1987.

[64] E. Luna, A. Bruschi, G. Granucci, C. Sozzi, and J. Collaboration. Electron cyclotron emission radiometer upgrade on the joint european torus (jet) tokamak. *Review of Scientific Instruments*, 75(10):3831–3833, 2004.

[65] A. Mase, H. Igami, R. Kumazawa, N. Ohyabu, T. Shimozuma, and Y. Yoshimura. Electron cyclotron emission imaging on a large helical device. *Review of scientific instruments*, 74(3):1445–1448, 2003. doi: 10.1063/1.1539267.

[66] K. Matsuda. Ray tracing study of the electron cyclotron current drive in diii-d using 60 ghz. *IEEE Transactions on Plasma Science*, 17(1):6–11, 1989. doi: 10.1109/27. 21664.

[67] E. mazzuccato. "relativistic effects on microwave reflectometry. *Physics of Fluids*, B 4, 10:p. 1015, 1992.

[68] G. Merlo et al. Turbulent transport in tcv plasmas with positive and negative triangularity. *Physics of Plasmas*, 26(10):102302, 2019. doi: 10.1063/1.5115390.

[69] G. Merlo et al. Nonlocal effects in negative triangularity tcv plasmas. *Plasma Physics and Controlled Fusion*, 63(4):044001, 2021. doi: 10.1088/1361-6587/abe39d.

[70] J.-M. Moret, B. Duval, H. Le, S. Coda, F. Felici, and H. Reimerdes. Tokamak equilibrium reconstruction code liuqe and its real time implementation. *Fusion Engineering and Design*, 91:1–15, 2015.

[71] Y. Nagayama, S. Kubo, S. Itoh, T. Shimozuma, and Y. Yoshimura. Electron cyclotron emission diagnostics for helical plasma in large helical device. In *The 30th International Conference on Plasma Science, 2003. ICOPS 2003. IEEE Conference Record-Abstracts.*, pages 271–. IEEE, 2003. doi: 10.1109/PLASMA.2003.1231681.

[72] T. Ohkawa. Steady state operation of tokamaks by rf heating. *General Atomics Report GA-A13847*, 1976.

[73] J. I. Paley et al. Real time control of plasmas and ECRH systems on TCV. *Nuclear Fusion*, 49(8):085017, July 2009. doi: 10.1088/0029-5515/49/8/085017.

[74] Y. Peysson and J. Decker. A versatile ray-tracing code for studying rf wave propagation in toroidal magnetized plasmas. *Plasma Phys. Control. Fusion*, 54(045003), 2012.

[75] Y. Peysson, R. Arslanbekov, V. Basiuk, J. Carrasco, X. Litaudon, and J. Bizarro. Magnetic ripple and the modeling of the lower-hybrid current drive in tokamaks. *Physics of Plasmas*, 3(10):3668–3688, 1996.

[76] R. Piessens, E. de Doncker-Kapenga, C. W. Oberhuber, and D. K. Kahaner. *QUAD-PACK: A Subroutine Package for Automatic Integration*. Springer-Verlag, Berlin Heidelberg New York Tokyo, 1983.

[77] W. H. Press, S. A. Teukolsky, W. T. Vetterling, and B. P. Flannery. *Numerical Recipes in C: The Art of Scientific Computing*. Cambridge University Press, Cambridge, New York, Port Chester, Melbourne, Sydney, 2 edition, 1992.

[78] S. Rathgeber, H. Müller, M. Cavedon, T. Happel, U. Stroth, W. Treutterer, and A. U. Team. Estimation of edge electron temperature profiles via forward modelling of the electron cyclotron radiation transport at asdex upgrade. *Plasma Physics and Controlled Fusion*, 55(2):025004, 2013.

[79] S. Schmuck, H. Laqua, S. Marsen, P. Rong, and Y. Turkin. Design of the ece diagnostic at wendelstein 7-x. *Fusion Engineering and Design*, 84(7-11):1739–1743, 2009. doi: 10.1016/j.fusengdes.2009.01.039.

[80] S. Schmuck, L.-G. Eriksson, T. Johnson, F. Meo, O. Sauter, E. Stefanikova, T. Tala, D. Van Eester, and J. Collaboration. Electron cyclotron emission measurements on jet: Michelson interferometer, new absolute calibration, and determination of electron temperature. *Review of Scientific Instruments*, 83(12):125101, 2012.

[81] A. P. Smirnov and R. W. Harvey. The genray ray tracing code. Technical Report CompX-2000-01, Ver. 2, 2003.

[82] C. Sozzi, A. Bruschi, G. Granucci, E. Luna, M. Scannavini, and J. Collaboration. Optical design of the oblique ece antenna system for jet. *Fusion Engineering and Design*, 74(1-4):691–696, 2005.

[83] T. H. Stix. *Waves in Plasmas*. American Institute of Physics, 1992.

[84] A. Tema Biwole, L. Porte, A. Fasoli, A. Simonetto, and O. D'Arcangelo. Performance of a high vacuum, high temperature compatible millimeter-range viewing dump for the vertical ece experiment on tcv. *Fusion Engineering and Design*, 162:112079, 2021. ISSN 0920-3796. doi: https://doi.org/10.1016/j.fusengdes.2020.112079. URL `https://www.sciencedirect.com/science/article/pii/S092037962030627X`.

[85] B. J. Tobias, M. E. Austin, M. W. Brookman, X. Chen, N. C. Luhmann Jr, W. A. Peebles, E. J. Valeo, M. A. Van Zeeland, and R. S. Wilcox. Commissioning of electron cyclotron emission imaging instrument on the diii-d tokamak and first data. *Review of Scientific Instruments*, 81(10):10D928, 2010. doi: 10.1063/1.3483275.

[86] C. Tsironis. On the simplification of the modeling of electron-cyclotron wave propagation in thermonuclear fusion plasmas. *Progress In Electromagnetics Research*, 47:37–61, 12 2012. doi: 10.2528/PIERB12102911.

[87] M. B. U. Belotti and F. Engelmann. Radiative energy transfer in anisotropic, spatially dispersive, weakly inhomogeneous and dissipative media with embedded sources. *Rivista del Nuovo Cimento*, 20, 1997.

[88] E. Westerhof. Wave propagation through an electron cyclotron resonance layer. *Plasma Physics and Controlled Fusion*, 39(6):1015, jun 1997. doi: 10.1088/0741-3335/39/6/007. URL `https://dx.doi.org/10.1088/0741-3335/39/6/007`.

[89] A. E. White, W. A. Peebles, T. L. Rhodes, T. A. Carter, W. W. Heidbrink, G. J. Kramer, M. A. Van Zeeland, L. Zeng, J. A. Baumgaertel, D. R. Mikkelsen, et al. A correlation electron cyclotron emission diagnostic and the importance of multifield fluctuation measurements for testing nonlinear gyrokinetic turbulence simulations. *Review of Scientific Instruments*, 79(10):103505, 2008. doi: 10.1063/1.2964189.

List of Figures

List of Tables

List of Symbols and Acronyms

Acronyms

Tokamaks

- **TCV**: Tokamak à Configuration Variable (CH)

- **JET**: Joint European Torus (UK)

- **PLT**: Princeton Large Torus (US)

- **ALCATOR**: Alto Campo Toro (US)

- **TORE SUPRA**: Ancestor of the WEST tokamak (FR)

- **DIII-D**: Doublet III tokamak upgrade (US)

- **KSTAR**: Korea Superconducting Tokamak Advanced Research (KR)

- **ASDEX Upgrade**: Axially Symmetric Divertor Experiment Upgrade (DE)

Tokamak Physics

- **ECE**: Electron Cyclotron Emission

- **VECE**: Vertical Electron Cyclotron Emission

- **X-/O-mode**: eXtraordinary/Ordinary polarization of ECE

- **EC**: Electron Cyclotron

- **X2/X3**: Second/third harmonic of the X-mode emission

- **RF**: Radio Frequency wave

- **EC(R)H**: Electron Cyclotron (Resonance) Heating

- **ECCD**: Electron Cyclotron Cyrrent Drive

- **LHCD**: Lower Hybrid Current Drive

- **REs**: Runaway Electrons

- **HXRS**:Hard X-ray Spectroscopy

- **HFS/LFS**: High Field Side/Low Field Side of the tokamak

- **LCFS**: Last Closed Flux Surface

- **MHD**: Magheto-Hydro-Dynamics

- NTM: Neoclassical Tearing Modes

- **LOS**: Line Of Sight

- **WKB**: Wentzel-Kramers-Brillouin approximation

Codes

- YODA: ECE synthetic diagnostic developed during this thesis

- LUKE: 3D bounce-average Fokker-Planck equation solver

- c3po: Ray-tracing code

- spece: ECE synthetic diagnostic

Symbols

- λ_D: Debye length

- ω_p: Plasma frequency

- ν_{en}: Collision frequency between electrons and neutrals

- Ω_c: Cyclotron frequency

- Λ: Plasma dispersion relation

- ρ_L: Larmor radius

- μ: Magnetic moment

- n_e: Electron density

- B: Magnetic field strength

- T_e: Electron temperature

- m_e: Electron mass or rest mass (always specified)

- E: Electric field strength

- c or c_0: Speed of light in vacuum

- e: elementary charge

- ε_0: vacuum electrical permittivity

- $\ln \Lambda$: Coulomb logarithm

- T_{rad}: Radiation temperature

- τ: Optical depth

- ψ: Poloidal magnetic flux

- γ: Relativistic factor

- ω_{ECE}: Angular frequency of the fundamental harmonic of electron cyclotron emission

- f_{ECE}: Electron cyclotron frequency (in Hz)

- P: Power

- Ω_S: Solid angle

- ω: Augular frequency in rad/s

- $p_\parallel$ and $p_\perp$: Parallel and perpendicular (to the magnetic field lines) components of the electron momentum normalized to the thermal momentum

- p_{th}: Electron thermal momentum

- j_ω: EC eissivity coefficient for a certain frequency

- α_ω: EC absorption coefficient for a certain frequency

- N: Refractive index

- I_ω: EC Spectral intensity for a certain frequency

- s: ray path arc-length

- N_r: Ray refractive index

- j: Current density

- E_k: Kinetic energy

- $\parallel$: Parallel component of a vector

- $\perp$: Perpendicular component of a vector

- R_{cold}: EC Cold resonance position

- n: Harmonic number

- ξ: Cosine of the pitch angle

- k: Wave vector strength

- S_ω: EC Source function

- S: Electromagnetic energy

- ε: Dielectric tensor

- $\tilde{e}$: Polarization vector

- $f_{e,MJ}$: Maxwell-Juttner electron distribution function

- I_{BB}: Blackbody radiation intensity

- φ_L: Toroidal lanching angle

- θ_L: Poloidal launching angle

- ΔR: Radiometer channel bandwidth

- P_{BW}: Power bandwidth

- φ: Gyroangle

- Z: Vertical direction in tokamak

- R: Radial direction in tokamak

Acknowledgements

First of all, I want to thank Joan Decker, my supervisor at EPFL. Joan not only gave me the more unique than rare opportunity to work for a year on an ambitious and challenging project, but she always took care of me and my research with meticulousness and passion.

I thank Mathias Hoppe from the bottom of my heart, the best teacher I could have hoped for. Mathias was first a friend than a supervisor (as well as a great guitarist), and I am truly honoured to have been able to work with him. Thank you for your infinite patience with me. You were the true gamechanger of my thesis and I hope we will continue to work side by side for a long time.

Special thanks go to Professor David Dellasega for his continuous support and valuable advice. It is certainly not easy to supervise a thesis done completely abroad, but he managed it very well, always allowing me to maintain relations with the Politecnico.

Finally, thank you to my family who have always supported me in both joyful and difficult moments. Without you I would never have made it.